The Dissertation Committee for Wei Gao certifies that this is the approved version of the following dissertation:

Upper Mantle Seismic Structure beneath the Central Rio Grande Rift and beneath Eastern Mexico and Their Implications

Committee:

Stephen P. Grand, Supervisor

Luc Lavier

James F. Ni

Robert Tatham

Clark Wilson

Upper Mantle Seismic Structure beneath the Central Rio Grande Rift and beneath Eastern Mexico and Their Implications

by

Wei Gao, B.S.; M.S.

Dissertation

Presented to the Faculty of the Graduate School of

the University of Texas at Austin

in Partial Fulfillment

of the Requirements

for the Degree of

Doctor of Philosophy

The University of Texas at Austin

May, 2006

To My Parents and My Family

Acknowledgments

I would like to thank my advisor Steve Grand for his guidance, encouragement, and inspiration during the process of my PhD study at The University of Texas at Austin. His intelligence and knowledge of the latest developments in the area have benefited these studies and influenced me considerably. I also would like to thank Dr. Clark Wilson, Dr. Robert Tatham, Dr. James Ni and Dr. Luc Lavier for serving as my dissertation committee members.

I would like to thank the following colleagues with whom I have benefited a great deal: Eric Matzel for his help with setting up waveform inversion in this study that is based on his previous work; Brian Schlottmann for his help with operation of Unix system and improving my English; Nathan Simmons for wide and valuable discussions on many geophysical issues and improving my English writings; Paresh Patel and Christopher Sine for improving my English writings.

I want to thank many colleagues and friends in the Department of Geological Sciences and the Institute for Geophysics for their great friendship: Bryan Wilbur, Jason Gumble, Kevin Bain, Chengshu Wang, Mingjuan Shi, Xinxia Wu, Guoyue Niu, Hongbo Lu, Hao Xun, Eric Leuro, Chandan Kumar, Reeshidev Bansal, Sanjay Sood, and Samarjit Chakraborty.

I want to thank Dr. James Ni, Dr. Richard Aster, Dr. Scott Baldridge, Dr. Mike West, and Dr. David Wilson for valuable discussion on the La Ristra project.

Specifically, I want to thank my long time friend, Dr. Xiaoyang Ding, for his recommendation that influenced me to enter The University of Texas at Austin.

Finally, I thank my wife, her family and my family for their love and support during my study at The University of Texas at Austin.

Upper Mantle Seismic Structure beneath the Central Rio Grande Rift and beneath Eastern Mexico and Their Implications

Publication No. _______________

Wei Gao, Ph.D.

The University of Texas at Austin, 2006

Supervisor: Stephen P. Grand

I present new images of the P- and S-wave seismic structure of the upper mantle beneath the central Rio Grande rift and surroundings and beneath eastern Mexico. The upper mantle structure is determined using traveltime delays and seismic waveforms.

The P- and S-wave tomography beneath the rift is derived through the LSQR algorithm. Tomography shows large seismic anomalies (up to 5% and 8% variation in P- and S-wave respectively) in the shallow mantle. Beneath the rift and Mount Taylor lies the seismically slow shallow mantle that primarily caused by higher temperature with possibly a small amount of partial melt. The mantle deeper than 150-km beneath the rift is not anomalously slow. A fast anomaly near 500-km depth beneath the central Colorado Plateau is probably the trailing edge of the Farallon slab. A slow seismic anomaly to the east of that anomaly at 400-km depth appears to connect to the slow shallow anomaly beneath the Mount Taylor. Beneath the Great Plains a narrow fast structure is imaged throughout the upper mantle from 200 to 600-km depth. They may form small-scale convection beneath the central rift and surrounding region.

The P and S velocity models beneath eastern Mexico are derived through waveform inversion of triplicated P and S waves using a conjugate gradient algorithm. The optimal models have discontinuities of 6.2% and 7.3% at 410-km depth and 3.3% and 6.3% at 660-km depth for P and S respectively. A common feature of the models is a low velocity zone above the 410-km discontinuity, which may be due to partial melt induced by water release from the transition zone. The overall jump in velocity at 410-km is also larger than in previously published models. Another feature is that P-wave data require a small discontinuity at 490-km depth and S-wave data require an additional discontinuity at 600-km depth. This may be a thermal anomaly due to a flat lying slab or might reflect a phase change in the transition zone.

Also, I present a new technique for regional-scale joint inversion of body and surface waves and show its strengths using synthetic and real datasets.

Table of Contents

List of Tables

List of Figures

Chapter 1

INTRODUCTION

Seismology is a powerful tool for investigating the chemistry, dynamics and evolution of the Earth's interior because seismic wave speeds are sensitive to the composition, physical state, flow and temperature of the rock through which they pass. In this dissertation, I investigate upper mantle seismic structure beneath two tectonically interesting regions using two different seismological approaches. In part I I use back projection travel time tomography to image two-dimensional upper mantle structure beneath the central Rio Grande rift and surrounding regions using data recorded by a passive broadband seismic array (The Colorado P**La**teau/**Ri**o Grande rift **S**eismic **Tra**nsect Experiment, La Ristra). The seismic results are interpreted in terms of the ongoing tectonic activity in the region. In part II I use a waveform inversion approach to investigate the transition zone (from 300 to 700 km depth) beneath Eastern Mexico. The goal in this project was to determine in detail P and S wave velocity as a function of depth as opposed to mapping lateral variations in seismic properties. I used data recorded by the La Ristra array for this project as well although the approach is quite different from the technique used in part I. In part III I use a joint inversion of seismic body and surface waves to image two-dimensional upper mantle structure beneath the La Ristra array. It is a new approach to image regional scale upper mantle seismic structure using two complementary types of data. I conducted synthetic resolution tests to compare the results inverted by the two datasets (body waves, surface waves) and the combination of the two datasets.

The principal goal of the La Ristra seismic experiment was to image and interpret the seismic structure of the crust and upper mantle beneath the Colorado Plateau, the Rio Grande rift, and the southwestern Great Plains. Each of these physiographic provinces has exhibited distinctly different tectonic behavior for the past 100 Ma although prior to then the region was uniform in topography. Geoscientists have long debated the cause and mechanisms for the different behaviors of these provinces. Although activity that occurs at the boundaries of plates is well understood and attributed to mechanisms of plate interaction, even at present it is still not well understood why tectonic activity occurs within the continental interior. The La Ristra experiment consisted of a deployment of continuously recording broad band seismometers in a 970 km line extending from the western Great Plains, through the Rio Grande rift and the Jemez lineament, and into the central Colorado Plateau. It consisted of 54 seismic stations and was deployed from August 1999 to May 2001. The La Ristra project was funded by the National Science Foundation and the Institute of Geophysics and Planetary Physics at Los Alamos, and was supported by the IRIS Consortium Program for Array Seismic Studies of the Continental Lithosphere, PASSCAL. In this project four seismic methods: tomography, receiver function, surface wave analysis, and seismic anisotropy study, are used to estimate the seismic structure of the upper mantle beneath the array. Integrating geological and tectonic information with the seismic images of the upper mantle helps us better understand the above issues. The La Ristra research team consisted of five academic institutes: New Mexico Institute of Mining and Technology, New Mexico State University, University of Texas at Austin, Los Alamos National Laboratory, and Dine College. UT Austin took the responsibility for the seismic tomography.

In chapter 2 I will review the geologic and tectonic history of the region covered by the La Ristra seismic array and previous geophysical work done in this region. I will then describe the La Ristra seismic observations, including P and S wave travel time measurements and the inversion method used to image the upper mantle structure beneath the array. Finally, I discuss an interpretation of the results that integrates the seismic models and other geologic observations into a model that explains present day tectonics in the southwestern United States.

The upper mantle beneath eastern Mexico is an interesting region, wherein an oceanic slab has recently subducted into the transition zone of the upper mantle. The chemical and mineralogic changes that subducting slab causes in the upper mantle are still not well understood, especially within the transition zone. Furthermore, past work on seismic structure and mineral physics has still not resulted in a generally agreed upon model for the mineralogy of the transition zone. High resolution images of the seismic structure of the upper mantle transition zone are needed to better constrain the composition and mineralogy of the transition zone. Furthermore, such images in regions where subduction is occurring will be needed to better understand the role of subducted plates within the transition zone.

The second part of my dissertation is to determine the P and S seismic velocity structure of the upper mantle transition zone beneath Eastern Mexico. I used a new approach to do this that involves inverting seismic waveforms for velocity as a function of depth. The seismic observations used in the waveform inversion were collected in the La Ristra experiment. In this project high resolution 1-D P and S velocity models are produced from 300 to 700 km depth. Integrating mineral physics and tectonic information with the seismic images of the upper mantle will help us to better understand the effect of the change in composition and thermal states resulting from the subducted oceanic slab into the transition zone on seismic structures of the transition zone.

In chapter 3 I will review previous seismic studies of the upper mantle, analyze seismic data used in this project, describe the waveform inversion method, determine one-dimensional P and S seismic models beneath Eastern Mexico, and discuss their implications.

In chapter 4 I will briefly describe a new technique to jointly invert body and surface waves for regional scale upper mantle structure. And I show the complementary strengths of tomography of the combined dataset (body and surface waves) using synthetic and real datasets recorded by the La Ristra array respectively.

Chapter 2

UPPER MANTLE SEISMIC STRUCTUE BENEATH THE CENTRAL RIO GRANDE RIFT AND SURROUNDING REGION

2.1 Abstract

In this chapter I present models for the upper mantle P and S velocity structure beneath a southwestern United States transect extending from near the center of the Colorado Plateau across the Rio Grande rift to the Great Plains. The models were derived from travel times of compressional and shear seismic phases recorded by the La Ristra passive seismic array deployed from July 1999 to May 2001. Large variations in seismic velocity (up to 8% in S and 5% in P) are seen across the transect in the upper 200 km of the mantle. Seismically slow mantle underlies the Rio Grande rift and Jemez lineament and relatively slow mantle is seen beneath the Navajo volcanic field within the Colorado Plateau. The relative variations of P and S velocity imply that high temperatures are the primary cause of the slow mantle although a small amount of partial melting or hydration cannot be ruled out. Sharp boundaries in mantle seismic velocity are coincident with boundaries of Proterozoic structural trends implying that ancient lithospheric structure exerts a control on the tectonic and magmatic activity in the region. Weaker seismic variations are imaged below 200 km depth with three

southeastward dipping structures identified in our images. Two of the structures have fast seismic anomalies, beneath the central Colorado Plateau and the Great Plains respectively, and the third has anomalously slow seismic wave velocity. I interpret the western deep seismic anomaly to be foundering Farallon slab and the slow anomaly just to the east as upwelling mantle possibly associated with volatile release from the sinking Farallon slab. Beneath the Great Plains, there is also downwelling in the upper mantle. The combination of upwelling in the west and downwelling in the east are likely part of an upper mantle convection cell that may include entrained lithosphere from beneath the Rio Grande rift.

2.2 Introduction

Since the late Cretaceous, the southwestern United States has passed through several profound tectonic events resulting in widespread magmatic activity, large scale uplift and crustal shortening, and more recent rifting and extension. The forces that caused this activity produced different surface manifestations in different regions. The result is that the present day southwestern United States can be divided into a number of distinct tectonic regions (Figure 2.1). The Great Plains have low relief and have not undergone significant deformation since Precambrian times. They form the western edge of the North American craton. The Colorado Plateau to the west has also been tectonically stable since Precambrian times (Morgan and Swanberg, 1985) but today lies at an

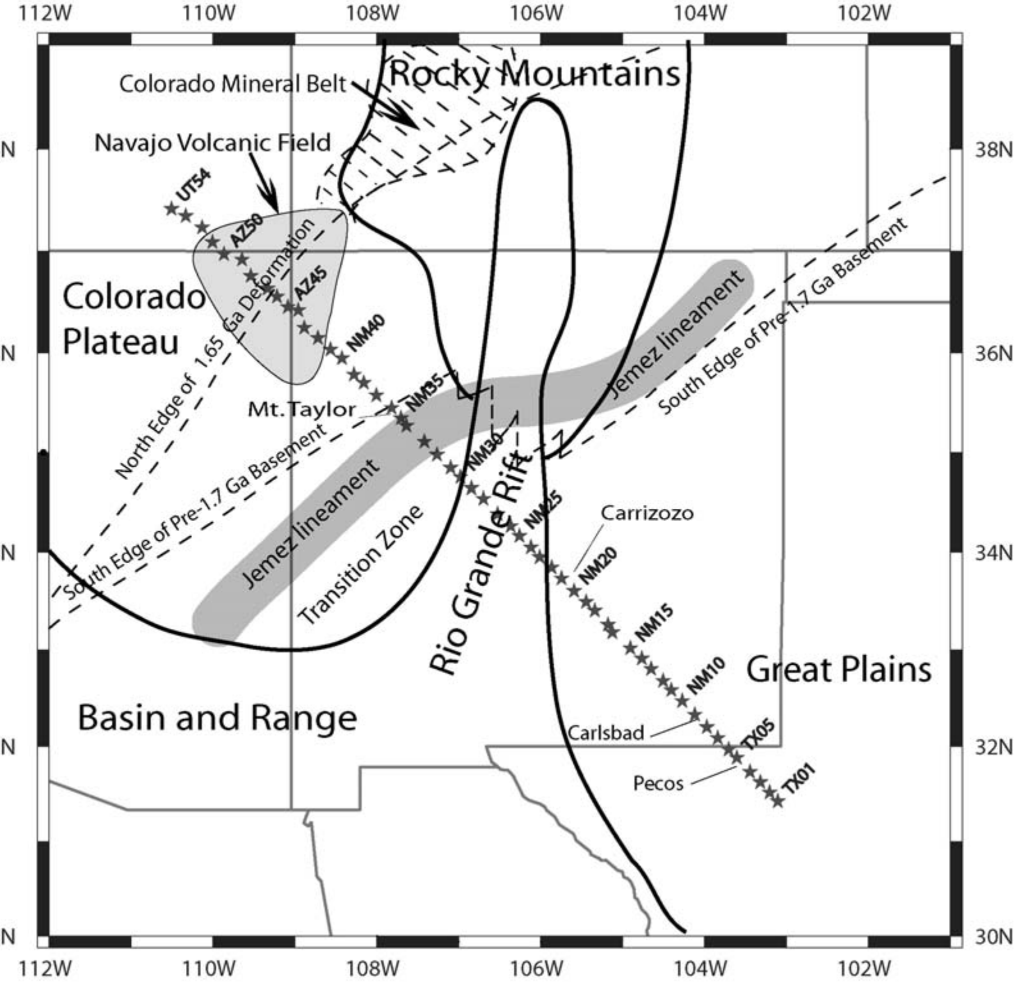

Figure 2.1 Map of the southwestern United States showing the locations of the La Ristra array seismic stations. The location of the main physiographic and tectonic provinces discussed in the text, are also shown. Dashed lines show boundaries of two Proterozoic provinces from Karlstrom and Humphreys (1998). The Colorado mineral belt lies along the northwestern Proterozoic boundary shown in the figure in the northern part of the map.

average elevation of about 1.8 km. Between the Plateau and the Great Plains lies the Rio Grande rift, a north-south trending series of faulted basins extending from Colorado to the Big Bend region of Texas. The rift has exhibited extensive deformation and volcanism during the Cenozoic. The most recent voluminous volcanism, however, has occurred to the west of the rift along a northeast trend called the Jemez lineament (Baldridge et al., 1991). In south-central New Mexico the Jemez lineament lies in what has been termed a transition zone between the Colorado Plateau and the Rio Grande rift. Surrounding the Colorado Plateau to the south and west lies the Basin and Range province that has undergone widespread extension since mid-Tertiary times and several episodes of deformation since the Mesozoic.

The Colorado P**La**teau/ **Ri**o Grande Rift **S**eismic **Tra**nsect Experiment (La Ristra) is a passive seismic experiment that was run along a transect from the Great Plains, across the Rio Grande rift and Jemez lineament, to the middle of the Colorado Plateau. The experiment consisted of 54 broad band seismic instruments deployed in a northwest oriented linear array shown in Figure1. The array was deployed from July 1999 to May 2001 with continuous recording at 20 samples per second using Reftek 24-bit acquisition systems supplied by PASSCAL. The goal of the project was to seismically image the crust and mantle beneath the three tectonic provinces in order to better understand the different tectonic behavior of the provinces as well as to understand the forces driving recent activity in the region. A more refined understanding of the present subsurface should also result in a better understanding of the diverse history of the region. In this chapter, I present two dimensional models of P and S velocity variations within the mantle beneath the La Ristra. The models extend from the Moho to 600 km depth with resolving power on the order of 50 km. The models were determined using back projection tomography of compressional and shear wave teleseismic delay times. In the remainder of the introduction I briefly review the geologic and tectonic history of the region covered by the La Ristra array and previous geophysical work done in this area.

2.2.1 Geological setting

The basement rock of the southwestern United States consists of several Proterozoic terranes that were successively added to the North American craton during collisional tectonic events. The 1.8 Ga Yavapai province is exposed in Arizona and is juxtaposed to the Matzatzal province (1.6 to 1.7 Ga) to the southeast (Karlstrom and Bowring, 1988). The Grenville orogeny (~1.1 Ga) completed the assembly of the southwestern part of the craton during the collision of Laurentia with an uncertain land mass to the southeast (Mosher, 1998). The sutures connecting the different Proterozoic terranes tend to have a northeast-southwest trend through a region extending from Arizona to west Texas. Through much of the Paleozoic, the southwestern United States was stable at or below sea level. An exception to this was a major orogenic event that occurred about 300 Ma resulting in the Ancestral Rocky Mountains that extended from west Texas through New Mexico to central Wyoming. By the beginning of the Cretaceous, however, the region extending from western Arizona to the central United States was below sea level. Ericksen and Slingerland (1990) show smoothly varying contours of paleobathymetry for the Cretaceous Interior Seaway indicating that lithospheric (crust and mantle) buoyancy was similar for a region extending from western Arizona to the present day Great Plains in the central United States at roughly 100 Ma. The subsidence causing the seaway is thought to be due to tilting of the North American continent caused by mantle flow resulting from subduction of the Farallon slab beneath the west coast of North America (Mitrovica et al., 1989).

From roughly 80 to 40 Ma, major uplift of the southwestern United States occurred during the Laramide orogeny. The uplifted region extended to central New Mexico and Colorado in a region not far from the Ancestral Rockies. Coincident with the Laramide uplifts far inland from the subduction zone to the west, was an eastward migration of volcanism from the Sierra Nevada volcanic arc (Coney and Reynolds, 1977) to New Mexico and Colorado. This has led to the hypothesis that a flattening of the subducting Farallon slab was the cause of the Laramide orogeny (Dickinson and Snyder, 1978) as well as the accompanying volcanism. Deformation during the Laramide was not uniform. The Colorado

Plateau was little deformed during the Laramide whereas central Colorado and New Mexico underwent extensive high angle reverse faulting and crustal shortening. From 40 to 20 Ma, a westward migration of calc-alkaline ignimbrite eruptions occurred that is thought to be related to the foundering of the flat Farallon slab (Humphreys, 1995). During the same period extension began in New Mexico within the Rio Grande rift that runs north-south through the center of the state. Extension also began south and west of the Colorado Plateau throughout the Basin and Range province.

At present, the southwestern United States consists of several distinct tectonic blocks (Figure 2.1). The 1.8 km high Colorado Plateau is an uplifted region that has experienced little deformation since Precambrian times (Morgan and Swanberg, 1985). The timing of the uplift is uncertain with estimates ranging from the Plateau attaining present elevations at the end of the Laramide (~40 Ma) to having 1 km of uplift within the last 5 Ma (Sahagian et al., 2002; Pederson et al., 2002; Chase et al. 2002). The Plateau is in isostatic equilibrium (Thompson and Zoback, 1979) so that the cause of the high topography is due to an increase in buoyancy of the crust or mantle beneath the Plateau since mid-Cretaceous time. Bird (1988) proposed that flat subduction of the Farallon plate during the Laramide orogeny displaced the lithosphere beneath the Plateau eastward. Subsequent foundering of the slab led to warm asthenosphere rising beneath the Plateau to cause the uplift. Isotopic evidence from xenoliths, however, shows that

Proterozoic mantle rock still remains beneath the Plateau (Livaccari and Perry, 1993). This has led Spencer (1996) to propose that just the deeper lithosphere (below 80 km or so) was removed during the Laramide to account for the increase in elevation of the Plateau. Riter and Smith (1996), however, conclude from analyses of xenoliths erupted in the Navajo field that the mantle beneath the central Colorado Plateau was cold to at least 140 km depth 25 Ma. McQuarrie and Chase (2000) and Chase et al. (2002) propose that uplift of the Plateau was due to thickening of the crust during the Laramide. Selverstone et al. (1999) argue for a boundary in the central Colorado Plateau dividing different Proterozoic lower crustal xenolith populations arguing against significant lower crustal flow prior to 25 Ma or so. Humphreys et al. (2003) propose that hydration and heating of the lithosphere has been the main source of uplift throughout the western United States. Although it is clear the Plateau has been uplifted at some time during the past 40 Ma, the cause is still uncertain.

To the east of the Colorado Plateau lies the Rio Grande rift that separates the Plateau from the Great Plains. The region of the Rio Grande rift was faulted and uplifted during the Laramide orogeny. The rift also marks the eastern limit of Eocene arc volcanism (Lawton and Mcmillan, 1999). Extension within the rift has not been a uniform process (Morgan et al., 1986). A first period of extension occurred from about 30 to 20 Ma and a second period occurred beginning 10 Ma until about 3 Ma. Magmatism accompanied both periods of rapid extension while the time between rapid extension events was accompanied by a lull in magmatic activity (Morgan et al., 1986; Baldridge et al., 1991). The source of volcanics during the 30 to 20 Ma extension event appears to be mantle lithosphere whereas the more recent volcanism in the central and southern part of the rift has an asthenospheric isotopic signature (Perry et al., 1987; McMillan et al., 2000) indicating that the lithosphere has been thinned to something on the order of 50 km thickness over time. Volcanism today is far more active to the west of the rift along a northeast trend known as the Jemez lineament (Baldridge et al., 1991). The region of the Rio Grande rift is also topographically high today. Eaton (1987) noticed that the topography of the southern Rocky Mountains resembles that observed for oceanic ridges and proposed that the Rio Grande rift is the central graben of a north-south trending continental ridge. As with the Colorado Plateau, there is still uncertainty surrounding the timing of the uplift of the Rio Grande rift region. Gregory and Chase (1992) argue from paleobotanical evidence that the southern Rockies attained their topographic highs by the end of the Laramide (about 40 Ma) whereas Axelrod and Bailey (1976) and Heller et al. (2003) argue for significant uplift (over 1 km) during the past 10 Ma. As with the Colorado Plateau, there is reasonable agreement over the tectonic events that have shaped the Rio Grande rift region but the timing of the events and the underlying cause is still uncertain.

The Great Plains, to the east of the Rio Grande rift, has been tectonically stable since Precambrian times but has experienced uplift during and since the Cretaceous. The uplift has resulted in a tilt of the plains from a height of 1.5 km above sea level in eastern New Mexico to elevations of about 200 m in eastern Texas and Oklahoma (Mitrovica et al., 1989). The cause of the tilt may be due to dynamical effects caused by the subducting Farallon plate (Mitrovica et al., 1989) or an increase in crustal thickness (Bird, 1984).

In summary, the southwestern United States has several well defined tectonic/physiographic provinces. The history of magmatism and tectonic activity is reasonably well documented although the timing of topographic changes is still uncertain. More uncertain are the underlying driving forces for the geologic activity in the region over time. Also not well understood is the reason for the different behavior of different tectonic provinces within the region.

2.2.2 Previous geophysical results

Many geophysical studies have been conducted in the region covered by the La Ristra array. Refraction and surface wave studies within the rift indicate a thinned crust and slow (presumably hot) shallow mantle (Keller et al., 1990; Sinno and Keller, 1986; Keller and Baldridge, 1999). Wilson et al. (2005) have analyzed receiver functions using data from the La Ristra array and confirm the thinning of the crust beneath the Rio Grande rift. They find crustal thicknesses of about 35 km beneath the rift as opposed to 42-45 km beneath the Colorado Plateau and 45-50 km beneath the Great Plains. Heat flow is high within the rift relative to the Great Plains to the east and the Colorado Plateau to the west (Lachenbruch and Sass, 1977). Pn velocities have been measured as low as 7.6 km/sec beneath the Rio Grande rift (Olsen et al., 1979) whereas Pn velocities beneath the Colorado Plateau are found to be about 8.1 km/sec (Beghoul et al., 1993). Lastowka et al. (2001) used surface wave dispersion measurements to find that the Colorado Plateau has a thin shear wave high lid with low velocities beneath. Less work on the deep crust and mantle has been conducted to the east of the rift in the Great Plains. Large scale studies of upper mantle seismic, however, show a strong contrast in upper mantle shear velocity to about 200 km depth between the Great Plains just to the east of the rift, and the Rio Grande rift - Colorado Plateau region (Van der Lee and Nolet, 1997; Grand, 1994).

Several passive seismic experiments span the Rio Grande rift and sample the margins of the Colorado Plateau and Great Plains (Spence and Gross, 1990; Parker et al., 1984; Davis et al., 1993). Slack et al. (1996) combined all the available data from previous experiments to determine a three-dimensional model of P velocity beneath the rift and surrounding regions. Their results show slow P wave velocities from 35 to 145 km depth along a NE-SW trend associated with the Jemez lineament. Relative to the Great Plains the velocities are 7-8% slower within this feature. They do not find very slow mantle velocities beneath the Rio

Grande rift and conclude that any thermal signature associated with Miocene rifting of the rift has greatly diminished. Examination of the Slack et al. data, however, shows a clear distinction between rift and the Jemez lineament only at the southern edge of their model where resolution of structure may not be very good. Also, below 145 km depth, P velocity appears slower beneath the rift than beneath the Jemez. In contrast to the Slack et al. results, West et al. (2004), from the phase velocities of Rayleigh waves recorded by the La Ristra array, find shallow mantle shear velocity slower beneath the rift than beneath the Jemez lineament. The study of West et al. also finds a fast seismic lid beneath the Colorado Plateau to 120-150 km depth underlain by much slower shear velocities. This is similar to the results of Lastowka et al. (2001) except that their seismic lid only extended to 65-70 km depth.

Geophysical studies of the Colorado Plateau, Rio Grande rift, and Great Plains show that both the crust and mantle have been modified beneath the rift and Jemez lineament transition zone, with thinner crust and slower mantle beneath these regions relative to the east and west. It also appears that the mantle at some depth beneath the Colorado Plateau is seismically slower than the mantle beneath the Great Plains. The detailed geophysical results, however, show many differences. Part of the differences may be due to the fact that each individual study only samples a portion of a particular tectonic province and there may be variability in mantle properties within each province. Resolution issues may also be important. Issues that are still unresolved include at what depth and how has Colorado Plateau lithosphere been modified to give the added buoyancy needed to uplift it 2 km? What has controlled the location of magmatism and extension in the southwest? What role does deep mantle flow play in the rifting and magmatism observed today?

2.3 Data and measurement

The La Ristra experiment consisted of a deployment of 54 three component broadband seismometers in a linear array extending from the Great Plains of west Texas across the Rio Grande rift and the Jemez Lineament, and ending in the center of the Colorado Plateau (Figure 2.2). The location of the La Ristra seismometers was showed in Table 2.1. The seismic line extended about 950 km with an average station spacing of 18 km. The orientation of the line was chosen such that the line lies close to the great circle path connecting the array to seismically active regions in Alaska, the Kuriles, Japan and Central and South America. The array operated from July 1999 to May 2001 with continuous recording. Figures 2.3 and 2.4 show an example of the La Ristra seismometers and stations respectively. The combination of the long length and the relatively tight station spacing, make the La Ristra array a unique data set for examining the seismic properties of the mantle beneath the southwestern United States.

Travel times of P waves with distances from 24° to 90°, PKP, PKIKP, and PcP were measured by visually aligning the wavelets from an individual earthquake, stacking them, and then using cross correlation of the first down (or up) swing in the data with the event wavelet determined by stacking. The P-wave data were band passed filtered from 1.0 Hz to 0.25 Hz. Only data with backazimuths between –20° and 20° of the azimuth of the seismic line were used to minimize the influence of seismic heterogeneity perpendicular to the array on the tomographic inversion. The events used for the inversion are shown in Figures 2.5 and 2.6. Using this process, 5007 compressional wave travel times were measured. Shear waves were measured using a similar approach but were filtered with only frequencies from 0.03 Hz to 0.1 Hz. For S waves and ScS waves, the data were rotated to radial and tangential components and the travel times were measured from the tangential component. The travel times of SKS waves were measured from the radial component. A total of 2164 S, ScS, and SKS travel time measurements were made. Travel time residuals were calculated for the data with respect to the IASP91 model of Kennett and Engdahl (1991) and means were then removed for each earthquake source for compressional and shear waves separately. An example of P and S waves produced by a single event is shown in Figure 2.7 with predicted travel times using the IASP91 model marked on each seismogram. The effect of topographic variations, crustal thickness variations, and sedimentary thickness variations were removed from the residuals using the

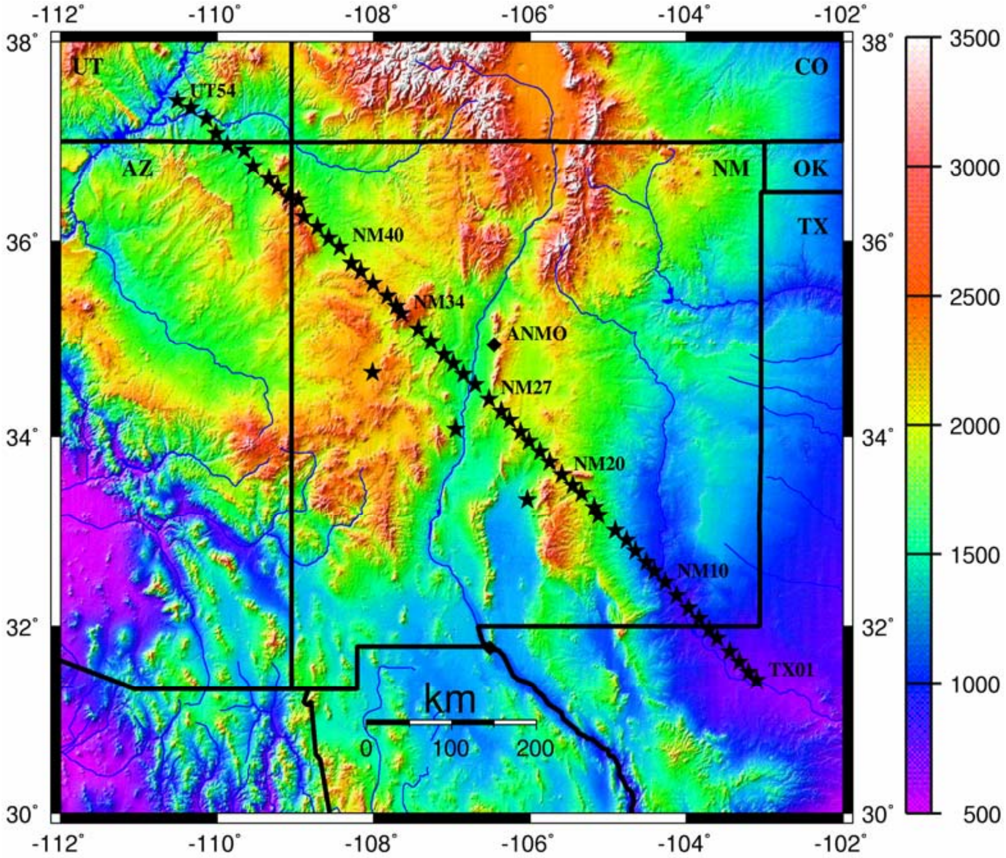

Figure 2.2 Topographic map showing the La Ristra station locations. The color scale indicates elevation in meters. The stars show main transect station locations. The diamond shows the location of the Global Seismic Network bolehole station ANMO.

Figure 2.3 Example of a La Ristra seismometer.

Figure 2.4 Example of a La Ristra station. A member (Dr. Steve Grand) of the La Ristra research team is seen servicing a station and aquiring seismic data.

Figure 2.5 Distribution of the events used that produced clear P waves. The star in the center of the figures marks the location of the La Ristra array. Not shown are a few earthquakes at distances beyond 100º that were used to measure PKIKP wave travel times.

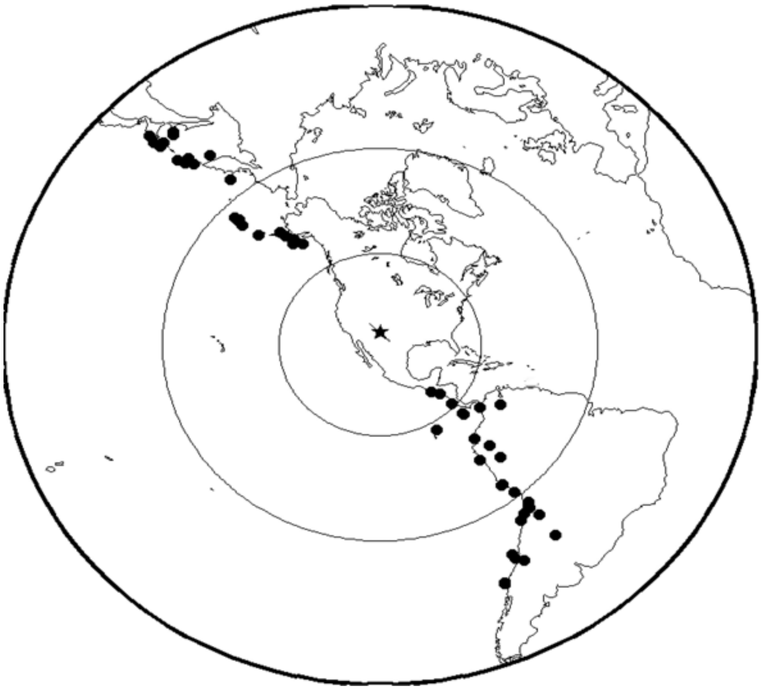

Figure 2.6 Distribution of the events used that produced clear S waves. The star in the center of the figures marks the location of the La Ristra array. Not shown are a few earthquakes at distances beyond 100° that were used to measure SKS wave travel times.

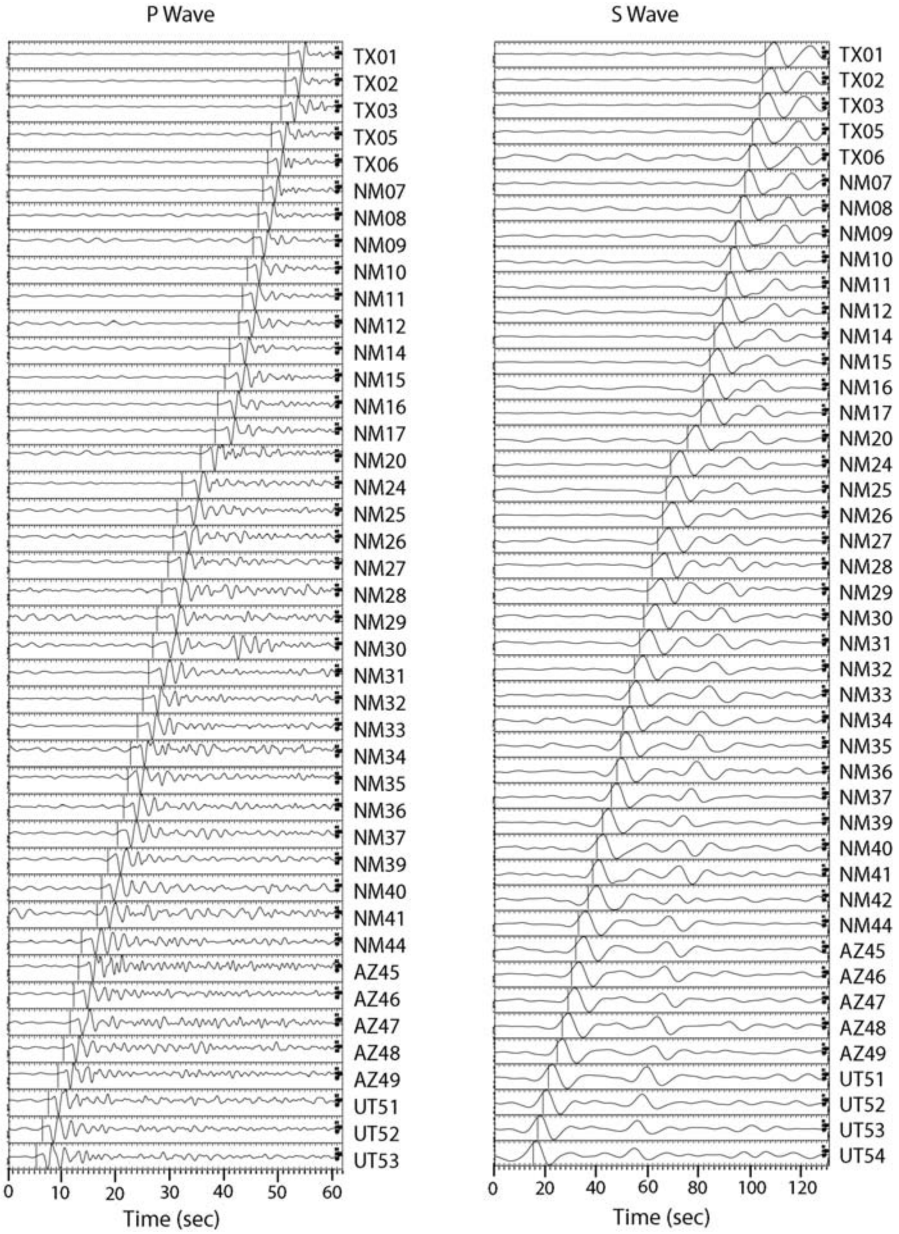

P Wave

S Wave

Figure 2.7 Some examples of P and S wave seismograms recorded by the La Ristra stations from a single earthquake. Predicted origin times are marked on the data. Note the similarity in waveform at the beginning of the P and S waves and the variations in arrival time with respect to the predicted times.

results of Wilson et al. (2005) who analyzed receiver functions for each of the La Ristra stations. I used their model for crustal structure to correct each residual to a 35 km thick crust with a simple structure measured at sea level. Figures 2.8 and 2.9 show the average residuals of the original data as well as the data corrected for near surface structure at each station for all compressional and shear phases respectively. The residuals are with respect to traveltimes calculated using the IASP91 model. The near surface corrections reach a maximum of 0.25 s for compressional phases and 0.75 s for shear phases respectively. The corrected residuals should reflect variations in mantle seismic structure beneath the array. In the inversion I heavily damped the solution in the crust.

The corrected travel time residuals of all the phases are shown in Figures 2.10 and 2.11 respectively. In these figures the data are divided into two groups depending on whether the earthquakes producing the seismic waves were to the northwest of the array or the southeast, respectively. Note the difference in residuals for both shear and compressional waves depending on the azimuth of the waves. The clear difference of the residuals with azimuth indicates that significant heterogeneity exists within the mantle at depth. Note also the similarity in pattern between the shear and compressional waves although the amplitude is different with shear waves varying a little more than 3 s in time across the array and P waves varying by about 1.5 s in time. Individual events show larger variations in residuals. Finally, note that the longwavelength pattern in residuals is primarily

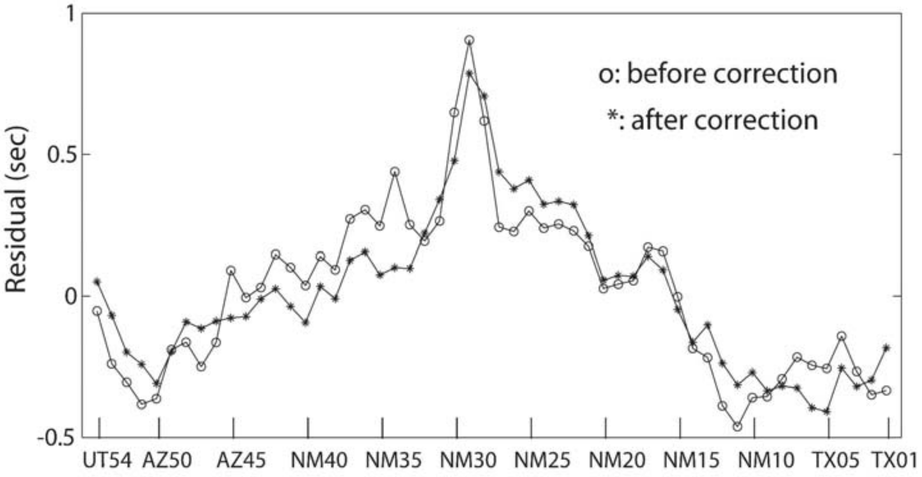

Figure 2.8 Average P wave residuals at each station in the La Ristra array. The closed symbols show the average residuals corrected for topography, crustal variations, and Moho depth. The open symbols show the uncorrected average residuals.

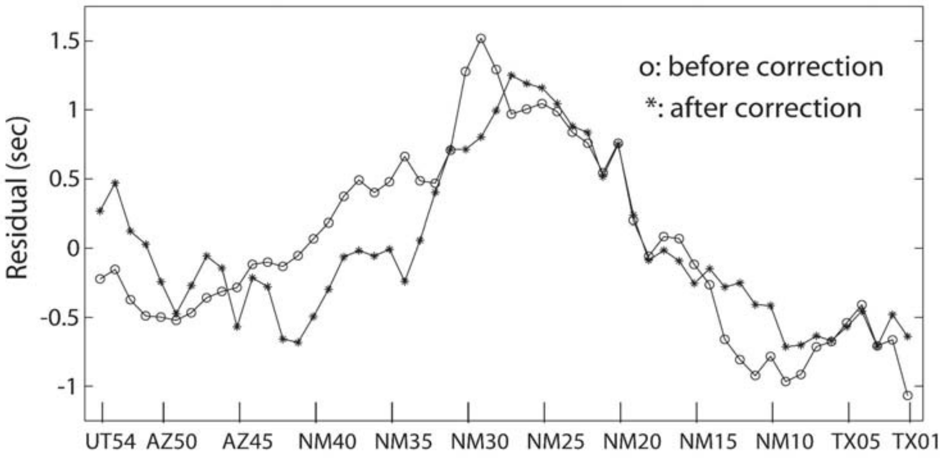

Figure 2.9 Average S wave residuals at each station in the La Ristra array. The closed symbols show the average residuals corrected for topography, crustal variations, and Moho depth. The open symbols show the uncorrected average residuals.

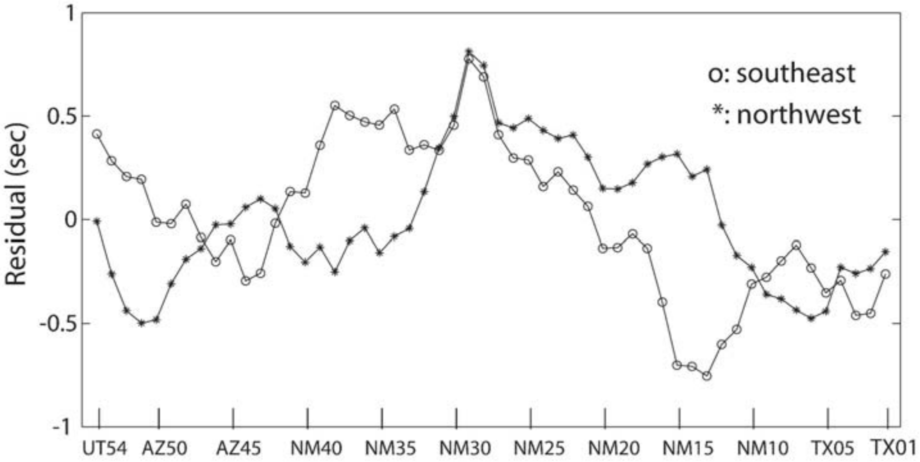

Figure 2.10 Average corrected P wave residuals as a function of backazimuth for the La Ristra stations. The open circles are average residuals from earthquakes to the southeast of the array, and the stars are residuals from earthquakes to the northwest of the line.

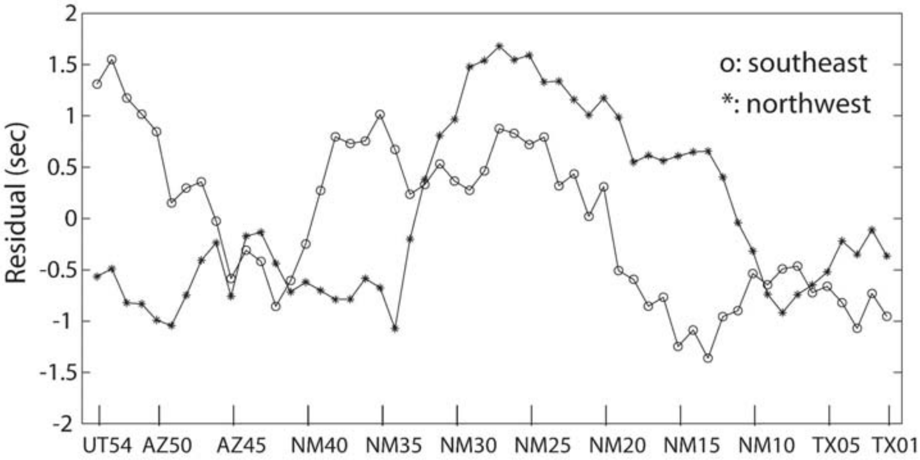

Figure 2.11 Average corrected S wave residuals as a function of backazimuth for the La Ristra stations. The open circles are average residuals from earthquakes to the southeast of the array, and the stars are residuals from earthquakes to the northwest of the line.

due to slow arrivals near the center of the array, likely due to slow mantle seismic velocities beneath the rift, but that there are also clear short wavelength anomalies in the data such as fast residuals from earthquakes to the southeast recorded by stations 13-17.

2.4 Tomographic method

Seismic waves traveling in the earth can be simplified as geometric rays at high frequencies. Therefore the travel time (t_t) of a seismic wave for a ray is a function of the $v_t(\boldsymbol{r})$ and the ray-path geometry

$$\boldsymbol{t_t} = \int_{s_t} \frac{\boldsymbol{dl}}{\boldsymbol{v_t(r)}} \qquad (2.4.1)$$

where ***dl*** is the distance the seismic wave travels in *dt* time, $v_t(\boldsymbol{r})$ is the velocity of the wave at $\boldsymbol{r}$, and s_t is the path the seismic ray traveled. However, in this case the velocities of the medium through which the seismic wave passed are unknown. The seismic structure will be determined from m traveltime observations at the surface. For this purpose a starting model describing the average seismic structure of the real earth is needed. Based on Fermat's Principle, time differences resulting from the difference between the real ray-path and the modeled ray-path are ignored (Aki et al., 1977). The predicted travel time (t_p) for the ray is

$$t_p = \int_{s_0} \frac{dl}{v_p(r)} \qquad (2.4.2)$$

where $v_p(r)$ is the velocity in the starting model, s_0 is the path the ray traveled. The difference between the real and predicted travel times resulting from the deviation of the velocity in the starting model from the true structure is

$$\Delta t = t_p - t_t = \int_{s_0} \frac{dl}{v_p(r)} - \int_{s_t} \frac{dl}{v_t(r)}$$

$$\approx \int_{s_0} [\frac{1}{v_p(r)} - \frac{1}{v_t(r)}]dl = \int_{s_0} [s_p(r) - s_t(r)]dl = \int_{s_0} \Delta s(r)dl \qquad (2.4.3)$$

where s_t is the true ray path, Δt is the residual time, $s(r) = 1/v(r)$ is the slowness, and $\Delta s(r) = s_p(r) - s_t(r)$. Suppose the slowness is a constant in each block, it holds

$$\Delta t = \int_{s_0} \Delta s(r)dl = \sum_{k=1}^{N} L_k \Delta s_k \ . \qquad (2.4.5)$$

where L_k is the ray segment length of the ray in the kth block, N is the number of blocks.

Generally, for an earthquake, if there are n stations available n different residuals can be obtained and for m quakes, there are $m \times n$ residuals and $m \times n$ equations

$$\Delta t_{pq} = \sum_{k=1}^{N} L_{pqk} \Delta s_k \ . \qquad (2.4.6)$$

where $p = 1, 2, ..., m$, $q = 1, 2, ..., n$. In seismic tomography one needs to find the solution of the equations (2.4.6) for Δs_k, the residual slowness. Hence, mathematically, the tomographic imaging is equivalent to solving a linear algebraic system

$$\boldsymbol{A}\boldsymbol{x} = \boldsymbol{b}. \qquad (2.4.7)$$

where $\boldsymbol{b} = (\Delta t_{ij})$ is a vector of length $m \times n$, Δt_{ij} is the travel time residual of the ith earthquake and jth ray, which is the difference between the predicted travel time and the observed travel time, $\boldsymbol{A} = (L_{ijk})$ is an $(m \times n) \times N$ matrix (N is the number of blocks), L_{ijk} is the ray segment length of the ith earthquake and jth ray in the kth block, and $\boldsymbol{x} = (\Delta s_k)$ is a vector of length N, where Δs_k is the slowness perturbation of the kth block. Although the matrix $\boldsymbol{A}$ is very large, it is sparse in typical tomography problems. In this case, matrix $\boldsymbol{A}$ is a *~5,000* by *2,000* matrix for the 2-D tomography inversion, but the number of non-zero elements in the matrix $\boldsymbol{A}$ is about *300,000*, and it is only about 3% of the total number of elements in matrix $\boldsymbol{A}$. With a sparse matrix approach for saving only non-zero elements in the sparse matrix $\boldsymbol{A}$, seismic tomography inversion with very large matrices is a feasible task on ordinary computers (see Appendix B).

In this tomography the LSQR algorithm (see Appendix A) will be used due to its good convergence and particularly good numerical properties for an ill-conditioned and noisy system (Paige and Saunders, 1982; Nolet, 1985). The LSQR algorithm is a least-squares conjugate gradient method. It is known that the conjugate gradient algorithm (CG) is an accurate algorithm, the residual vectors after each iteration are mutually orthogonal and monotonically decrease and theoretically an accurate solution can be obtained with n steps or less if there is no error in computation (van der Sluis and van der Vorst, 1987; and Spakman and Nolet, 1988). Nevertheless, there are some limits in the use of a standard conjugate gradient method, for example, matrix $\boldsymbol{A}$ is symmetric and positive. However, in a linear system of seismic tomographic inversion, $\boldsymbol{Ax} = \boldsymbol{b}$, matrix $\boldsymbol{A}$ is an m by n matrix. If one wants to use a standard conjugate gradient method, the linear system has to be changed into

$$\boldsymbol{A}^T\boldsymbol{A}\,\boldsymbol{x} = \boldsymbol{A}^T\boldsymbol{b} \qquad (2.4.8)$$

which are called the normal equations. One problem with using this transformation is that it decreases the accuracy of the solution in an ill-conditioned and noisy linear system. The LSQR algorithm, however, does not require that the matrix $\boldsymbol{A}$, in $\boldsymbol{Ax} = \boldsymbol{b}$, must be square, symmetric and positive definite matrix, but still has the same effect as the CG algorithm in solving a linear system. Also, it has the properties of the singular value decomposition (SVD) method which constructs the solution by neglecting those components belonging to the smallest eigenvalues of $\boldsymbol{A}^T\boldsymbol{A}$ (van der Sluis and van der Vorst, 1987; and Spakman and Nolet, 1988).

Practically the travel time residuals are then related to variations in the mantle by

$$\Delta t_{ij} = \sum_{j=1}^{n_i} L_{ijk}\Delta s_k + \overline{\Delta t}_i \qquad (i = 1, \ldots, m,\ k = 1, \ldots, N) \qquad (2.4.9)$$

where Δt_{ij} is the time residual of the i^{th} earthquake and its j^{th} ray, Δs_k is the difference in slowness of the k^{th} block with respect to the starting model, L_{ijk} is ray path length of j^{th} ray of the i^{th} earthquake through block k, n_i is the number of stations available for the i^{th} earthquake, and $\overline{\Delta t_i}$ is a static time shift for earthquake i. The linear equations given by equation (2.4.9) were solved iteratively using the LSQR algorithm of Paige and Saunders (1982). Nolet (1985) discusses this technique in more detail in relation to seismic travel time tomography. Aside from the travel time equations, we also added the following equations to the inversion.

$$S_j - 0.4S_{j-1} - 0.4S_{j+1} - 0.1\,S_{j-L} - 0.1\,S_{j+L} = 0 \qquad (2.4.10)$$

S_j is the slowness in block j, S_{j-1} and S_{j+1} are the slownesses in horizontal adjacent blocks to block j, and S_{j-L} and S_{j+L} are the slownesses in vertical adjacent blocks to block j and L is the number of blocks on each layer. These equations impose a smoothness constraint on the model. The degree of smoothing can be controlled by the weight given to equations (2.4.10). The stronger the smoothing constraint is the lower the variance reduction of the travel times in the inversion. Various smoothing weights were tested to produce a model that shows short wavelength structure with minimal incoherence in the model. Finally, we added the different damps for different layers to the inversion.

$$\lambda_j \Delta s_j = 0 \qquad (2.4.11)$$

where λ_j is an real scalar, and Δs_j is the slowness perturbation of the block j.

2.5 Resolution

The resolution of 2-D seismic tomography is determined by the length and geometry of a seismic array, the number of stations, the distribution and number of the events. It also depends on the reference model that describes the structure that will be imaged. Generally, we can not control the seismic sources, but we can strategically control where receivers are deployed, how long a seismic array needs to be deployed, how many stations are deployed, and what the orientation of the array is in terms of the global and regional seismicity and how deep structure needs to be imaged. The La Ristra seismic experiement was designed to investigate at what depth mantle processes control surface geologic and tectonic processes. Figure 2.12 shows an example of the La Ristra array observations. There are seven events, three from southeastern direction (epicentral distances are about 30º, 60º and 90º respectively), three from northwestern direction (epicentral distances are about 30º, 60º and 90º respectively), and one from vertical direction (epicentral distances are about 180º). It is seen that the area with cross ray paths is in the central region beneath the array, generally this region is well resolved, and the two side regions beneath the array are poorly resovled. The depth of the well resolved region is down to about 600 km.

Mathematically the resolution includes two parts: data resolution and model resolution (Menke, 1989). Suppose we found a generalized inverse in some sense for the inverse problem,

$$\boldsymbol{Gm} = \boldsymbol{d} \tag{2.5.1}$$

where $\boldsymbol{G}$ is determined by distribution of the stations and events and the reference model, which yields an estimate of the model parameters

$$\boldsymbol{m}^{est} = \boldsymbol{G}^{-g}\boldsymbol{d}^{obs} \tag{2.5.2}$$

where $\boldsymbol{G}^{-g}$ is the generalized inverse. Then we will ask how well this estimate of the model parameters fits the observations. Substituting $\boldsymbol{m}^{est}$ in equation (2.5.2) for $\boldsymbol{m}^{est}$ in equation $\boldsymbol{d}^{pre} = \boldsymbol{Gm}^{est}$, it holds

$$\boldsymbol{d}^{pre} = \boldsymbol{Gm}^{est} = \boldsymbol{G}[\boldsymbol{G}^{-g}\boldsymbol{d}^{obs}] = [\boldsymbol{GG}^{-g}]\boldsymbol{d}^{obs} = \boldsymbol{Nd}^{obs} \tag{2.5.3}$$

where $\mathbf{N} = \boldsymbol{GG}^{-g}$ is called the data resolution matrix. On the other hand, we can estimate model resolution. Suppose $\boldsymbol{Gm}^{true} = \boldsymbol{d}^{obs}$, the estimate $\boldsymbol{m}^{est} = \boldsymbol{G}^{-g}\boldsymbol{d}^{obs}$, and it holds that

$$\boldsymbol{m}^{est} = \boldsymbol{G}^{-g}\boldsymbol{d}^{obs} = \boldsymbol{G}^{-g}[\boldsymbol{Gm}^{true}] = [\mathrm{G}^{-g}\mathrm{G}]\boldsymbol{m}^{true} = \boldsymbol{Rm}^{true} \tag{2.5.4}$$

where $\boldsymbol{R} = \boldsymbol{G}^{-g}\boldsymbol{G}$ is called the model resolution matrix. From equations (2.5.3-2.5.4) it is seen that both data and model resolutions are determined by the ray tracing matrix $\boldsymbol{G}$. If $\boldsymbol{N}$ or $\boldsymbol{R}$ are identity or close to identity, we can say the resolution is good.

Because the inverse of matrix $\boldsymbol{G}$, $\boldsymbol{G}^{-g}$, is difficult to calculate for a large matrix, to estimate the resolution in the inversion synthetic tests will be conducted. In our synthetic test we create a fictitious earth model, compute the residuals for the actual rayset that this model would produce, and then invert the

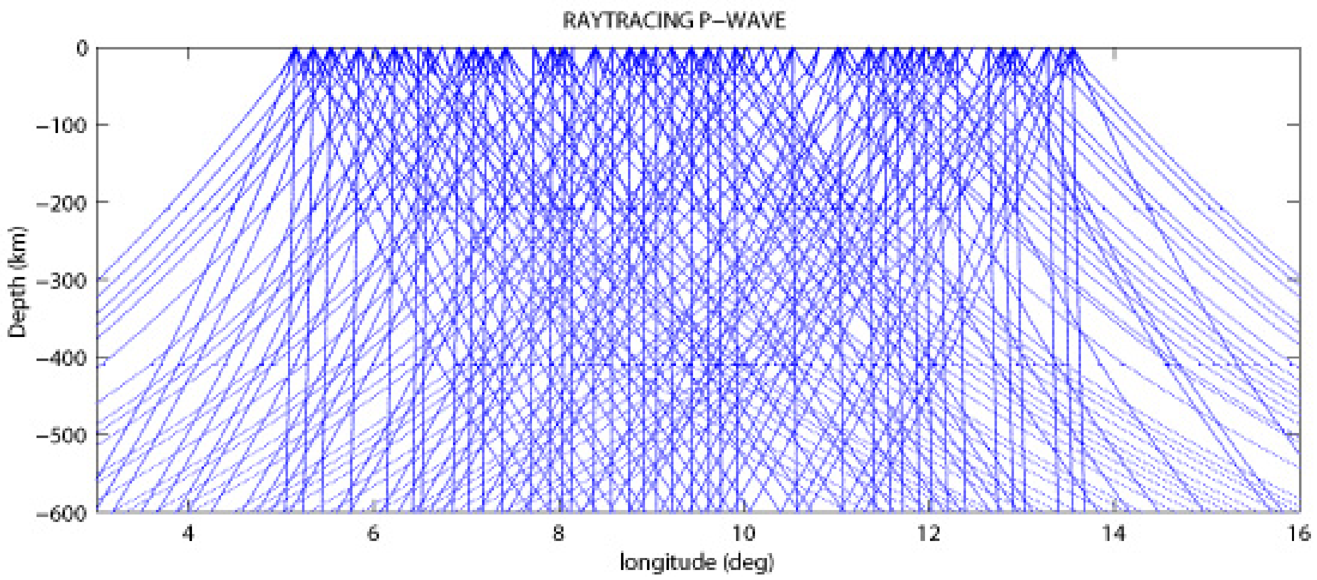

Figure 2.12 Some ray paths produced by real events. There are seven events, three from the southeastern direction (epicentral distances are about 30º, 60º and 90º respectively), three from the northwestern direction (epicentral distances are about 30º, 60º and 90º respectively), and one from the vertical direction (epicentral distances are about 180º)

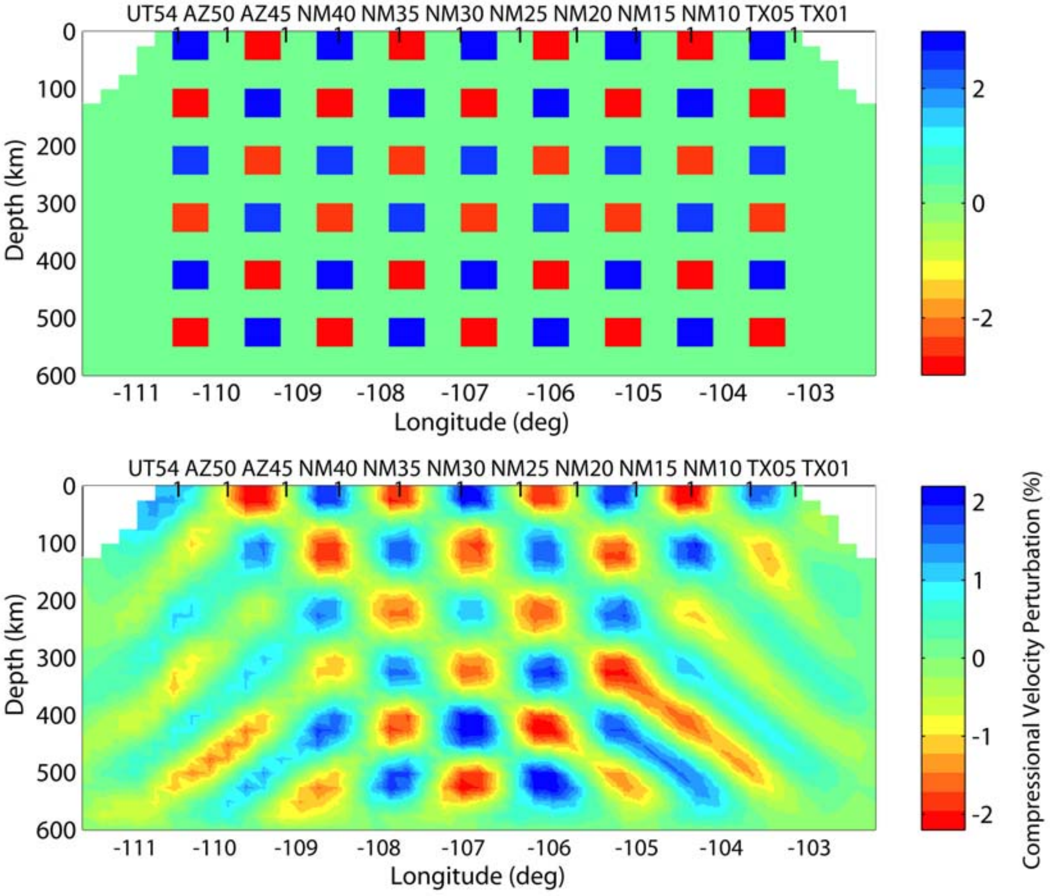

Figure 2.13 Synthetic resolution test for the compressional velocity model. The top panel shows the test input structure. The model consists of 50 km blocks which are used to compute a synthetic data set. The lower panel shows the result of inverting the synthetic P wave data using the same smoothing and inversion algorithm applied to the real data.

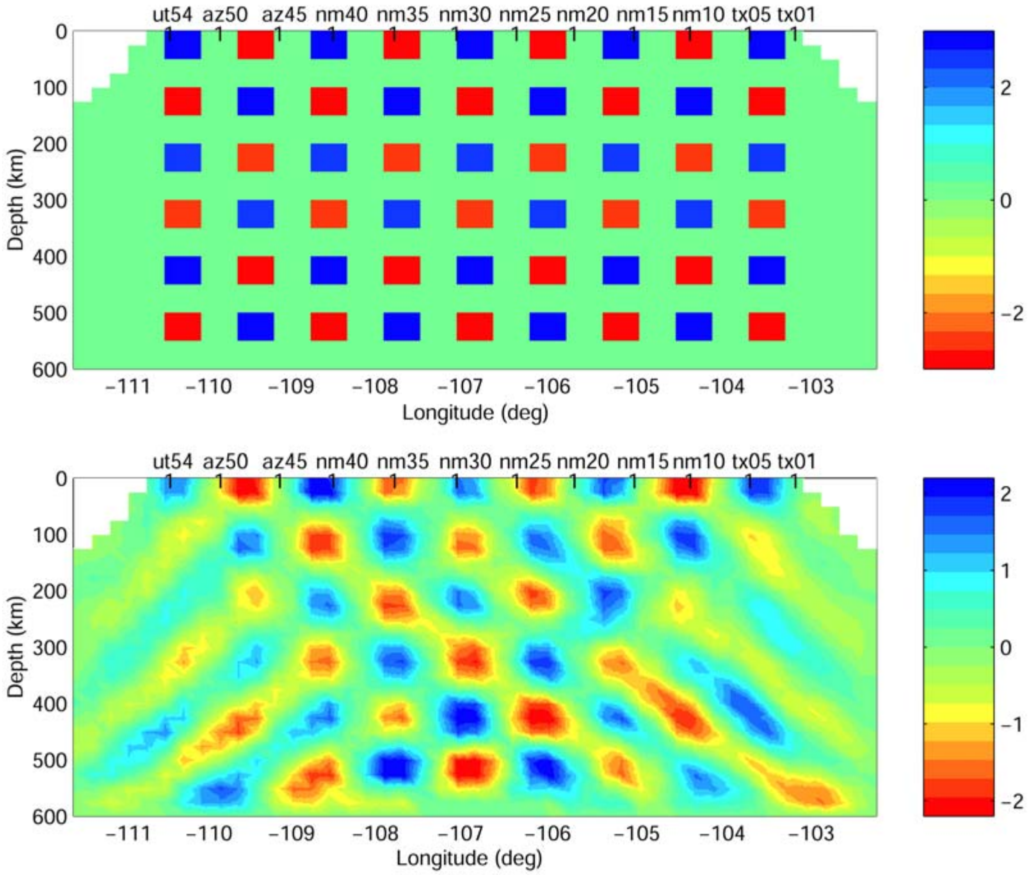

Figure 2.14 Synthetic resolution test for the shear velocity model. The top panel shows the test input structure. The model consists of 50 km blocks which are used to compute a synthetic S wave data set. The lower panel shows the result of inverting the synthetic S wave data using the same smoothing and inversion algorithm applied to the real data.

synthetic data in the same manner as was done in the actual inversion. Figures 2.13 and 2.14 show the results for one such test. The same starting model is shown in the top frame of Figures 2.13 and 2.14. This model was used for both P and S inversions. The alternating blocks in the test structure are 50 km in dimension. The lower panel shows the results of the P and S inversions respectively. The smoothing constraint degrades the inversion but the center of the array is still relatively well resolved to depths of around 600 km. Note that at the edges of the array, the input anomalies are not well resolved and show evidence of streaking due to the lack of crossing rays. It is consistent with the analysis results in Figure 2.12.

The largest sources of error in our models are likely due to our neglect of anisotropy and 3D variations in seismic velocity. Gok et al. (2003) examined shear wave splitting across the La Ristra array. They found the fast direction for SKS waves to be relatively uniform across the array with a northeast orientation. The magnitude of the splits has some shortwavelength variation but based on SKS splitting measurements alone, there is not enough constraint on anisotropy to include corrections in our inversion. Correcting our SKS travel time data for the measured splitting has negligible effect on our results. It is likely that including the effects of anisotropy on all the data would change the images in detail but given the relatively uniform fast direction of SKS splitting across the array, it is unlikely the major patterns of heterogeneity would change. Neglecting variations perpendicular to the seismic line is also a source of error that is difficult to quantify. Restricting the data to backazimuths within 20º of the azimuth of the seismic line should minimize these errors.

2.6 Tomographic results

In the inversion the travel time residuals were inverted for a two-dimensional model of P and S velocity beneath the array. The mantle beneath the array was divided into a two dimensional grid of equal size cells 25 km in dimension. For each residual, a ray was traced through the grid using the IASP91 model (Kennett and Engdahl, 1991).

2.6.1 Compressional and shear velocity models

The final compressional and shear models of the mantle beneath the La Ristra array are shown in Figurs 2.15 and 2.16 respectively. The upper 50 km of the model shows little lateral variation because the laterally variable crustal structure of Wilson et al. (2005) was used in the reference model and these depths were heavily damped in the tomographic inversion. The inverted model reduces the variance in the P wave data set by 83% and the variance in the S wave data by 79%. The largest amplitude variations in both P and S are within the upper 200 km. Within the upper 200 km, the lateral variations in P and S wave velocities are similar in pattern although in detail there are differences in relative amplitude.

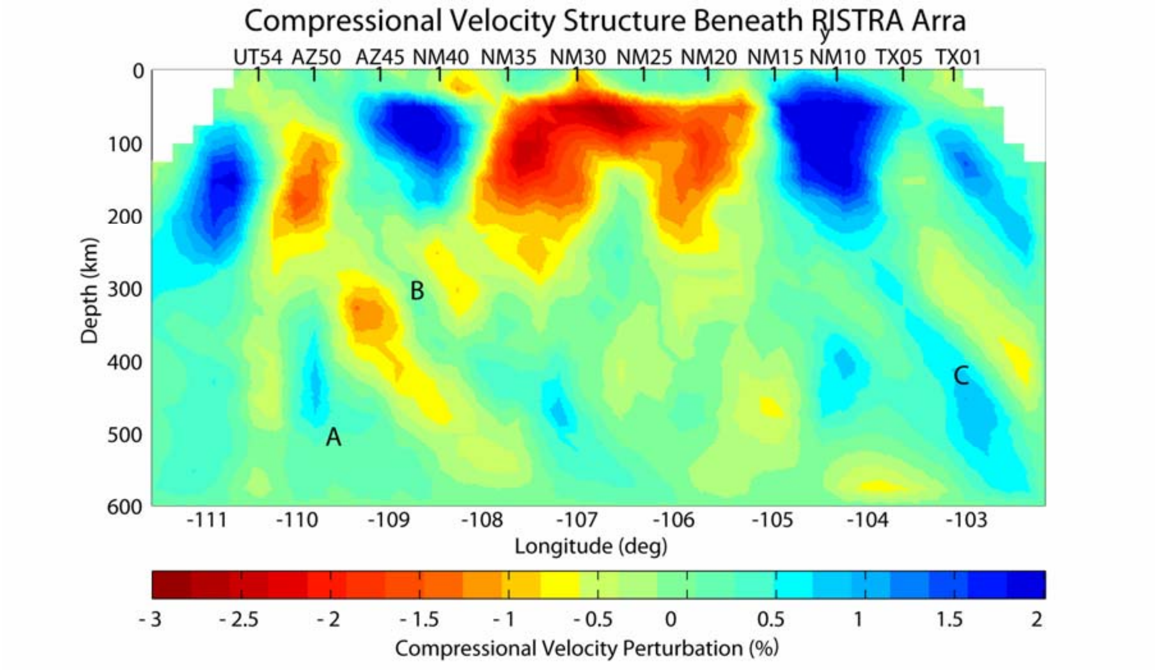

Figure 2.15 P velocity model obtained through the inversion of the P wave travel time residuals.

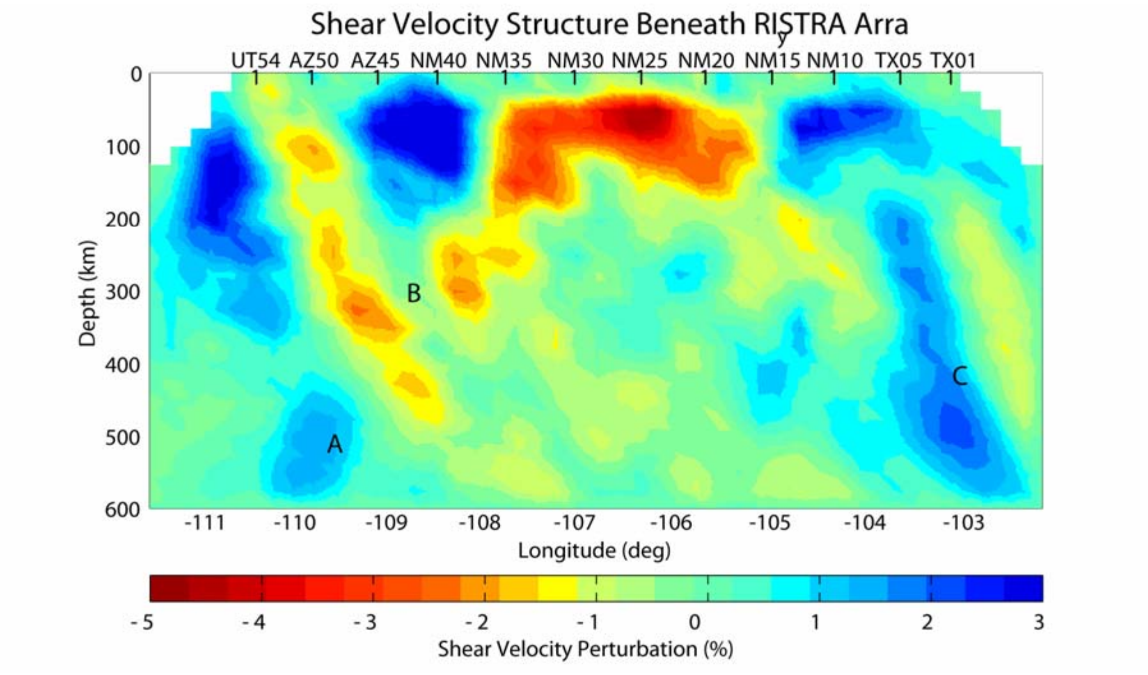

Figur 2.16 S velocity model obtained through the inversion of the S wave travel time residuals.

Both models show very slow wave velocities within the center of the array extending from station NM20 to station NM35. Station NM35 was situated on Mount Taylor, a volcano that is part of the Jemez lineament and can be considered the western most point in the transition zone along our line between the Rio Grande rift and the Colorado Plateau. Station NM20 was situated near the town of Carrizozo, NM. Carrizozo is situated at the eastern limit of the Rio Grande rift along the La Ristra line and has also been the site of recent volcanism (Laughlin et al., 1994). Our results differ from the model of Slack et al. (1996) in that we find very slow seismic velocity in the mantle beneath the Rio Grande rift as well as the Jemez lineament although the slow anomaly extends deeper beneath the Mount Taylor region than beneath the center of the rift. Our results do, however, agree qualitatively with the surface wave study of West et al. (2005). Although mantle velocities are higher beneath the Great Plains (stations TX01-NM19) and the Colorado Plateau (stations NM36-UT54) relative to the rift, there are significant variations of mantle velocity within those two provinces. In particular, the eastern edge of the Plateau has high P and S, but near the center of the Plateau (near station AZ50), seismic velocity is significantly lower. The fast eastern part of the Colorado Plateau is beneath the San Juan basin and the slower central part is beneath the Navajo volcanic field that saw a number of volcanic eruptions 20-30 Ma (Riter and Smith, 1996). The eastern part of the model also shows lateral variation in velocity. Although the mantle above 120 km depth is fast beneath stations TX01-NM16 that cover the western Great Plains, it is particularly fast at depths greater than 120 km beneath stations TX05-NM10. This narrow feature extends deeper in the shear wave image than the compressional wave image. The variability within the Colorado Plateau and the Great Plains makes it difficult to generalize differences in lithosphere thickness between the two provinces.

The mantle below 200 km depth shows less lateral variability in structure and more differences between the P and S models. The most prominent structure in the deep mantle is a slow anomaly beneath stations NM40 to AZ45 from 250 to 500 km depth labeled B in Figures 2.15 and 2.16. The anomaly is clearly seen in the shear model but appears weaker in the P model. Near the edges of our model, two deep fast anomalies are seen. The western anomaly, near 500 km depth beneath AZ50, is at the edge of the model in a region where there are no crossing rays and therefore is probably not well resolved. On the other hand, the anomaly is dipping to the southeast which is the opposite dip direction than one would expect for streaking of rays (Figure 2.14). The eastern anomaly is seen in the shear wave model beneath station TX05 extending from 200 to 600 km depth. The P model is also anomalous in the same region but is far stronger above 250 km depth. If the eastern fast anomaly is a downwelling, the difference in P and S may be due to anisotropy variations unaccounted for in the inversion. What is clear, however, is that there is anomalously fast mantle at depth over a relatively narrow horizontal distance beneath stations TX05-NM10.

2.6.2 Squeezing test

I tested whether the deep slow anomaly could be due to streaking of shallow structure to depth by performing “squeezing” experiments where by inversions are performed forcing all lateral variation in seismic wave velocities above a certain depth and then gradually releasing constraints on structure to greater depths. Evans and Achauer (1993) tested the resolution of situations in which traveltime residuals from anomalies outside the model space map into the image. In these cases the anomalies were mapped into the deepest layers of the model adjacent to the real feature, significantly distorting the result there. They stated that one should be careful to interpret the anomalies in the deepest layers and edges of a model. Saltzer and Humphreys (1997) conducted “squeezing” tests in which they limited the velocity perturbations to a smaller range of depths and then gradually release the constraints to a larger range of depths to find a “best” model. This processing permits any traveltime residuals that cannot be modeled with the smaller depth range to reconstruct structure elsewhere. In our “squeezing” test, the velocity perturbations are initially restricted to above a depth of 200 km, and then released to above depths of 300 km, 400 km and 500 km progressively. The results are shown in Figures 2.17 – 2.20. When the constraints are on a depth of 200 km, 300 km, and 400 km respectively, the slow anomaly expands downward to the bottom of the structure once the depth constraint was released (see Figures 2.17 – 2.19). When the depth constraint was released to 500 km, the slow anomaly stops expanding downward and stops at about 420 km (see Figure 2.20). But the two fast anomalies still expanded downward to the bottom (depth of 600km). Thus it is likely that some of the fast anomalies come from deeper structure or unmodeled structure within the array due to anisotropy. The variance reductions in these resolution tests are similar (77% for 200 km, 300 km and 400 km constraints, and 78% for 500 km constraint) but there are significant different in the peak-to-peak magnitude of the velocity anomaly (see the color bar in Figures 2.17-2.20). The peak-to-peak magnitudes are 13% for the 200 km constraint model, 10% for the 300 km constraint model, and 8% for the constraints deeper than 300 km. Surface wave observations beneath the array (West et al., 2004) indicate that velocities in the shallow mantle beneath the rift axis are 10% slower than beneath the Great Plains respectively. The surface waves should not be biased by deeper structure. Thus I feel the deep slow anomaly near 400 km depth is likely a real feature but that the fast velocities near 600 km depth are likely not well resolved. This is supported by the checkerboard tests shown in Figure 2.14 as well.

2.7 Ratio of Vp to Vs

Determining the cause of seismic heterogeneity is always problematic.

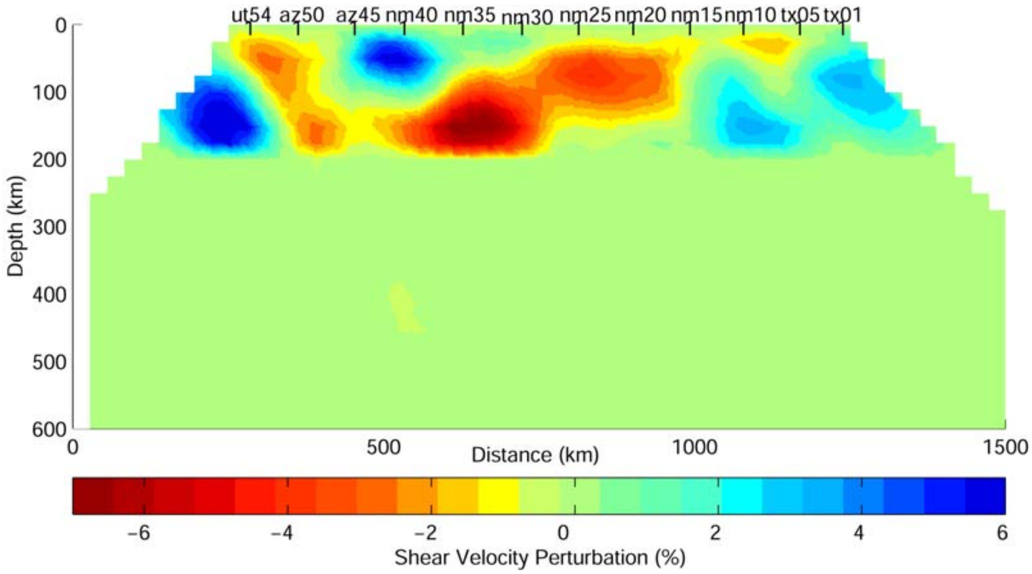

Figure 2.17 Tomography of a "squeezing" test (1). The velocity perturbations are limited to the region between 50 km and 200 km depth. Both fast and slow anomalies expanded downward to the bottom of 200 km depth.

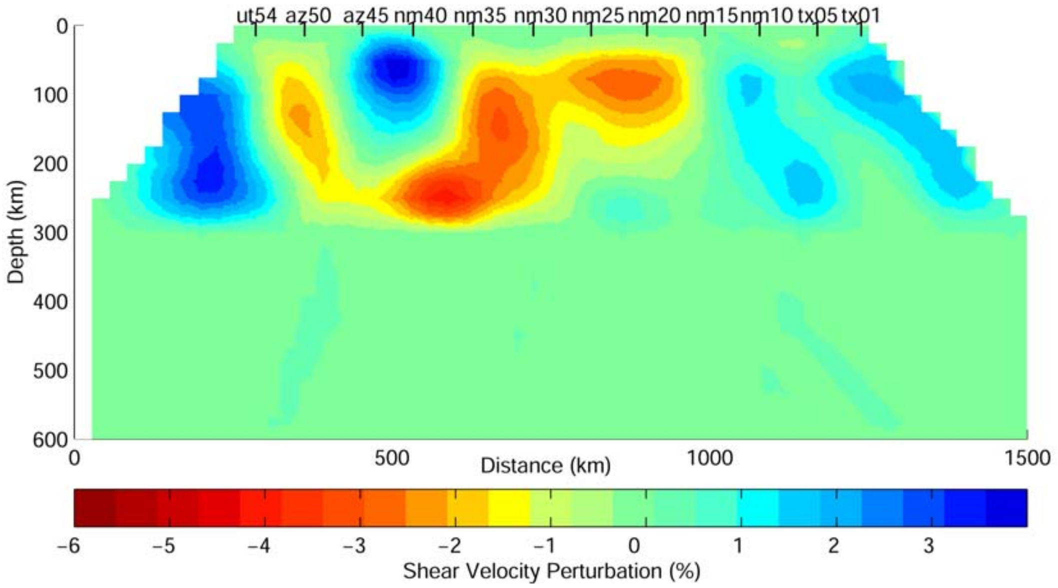

Figure 2.18 Tomography of a "squeezing" test (2). The velocity perturbations are limited to the region between 50 km and 300 km depth. Both fast and slow anomalies expanded downward to the bottom of 300 km depth.

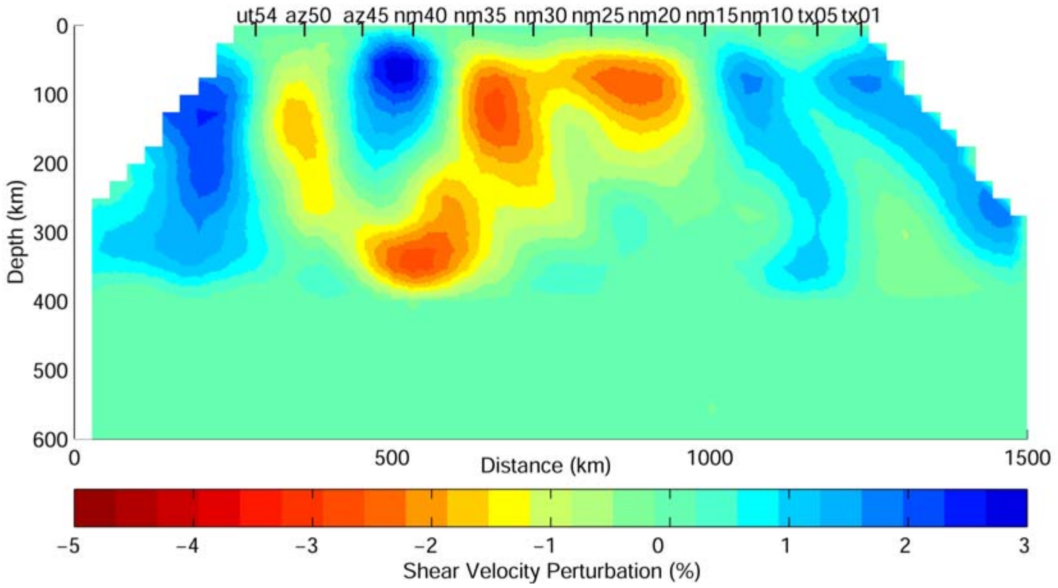

Figure 2.19 Tomography of a “squeezing” test (3). The velocity perturbations are limited to the region between 50 km and 400 km depth. Both fast and slow anomalies expanded downward to the bottom of 400 km depth.

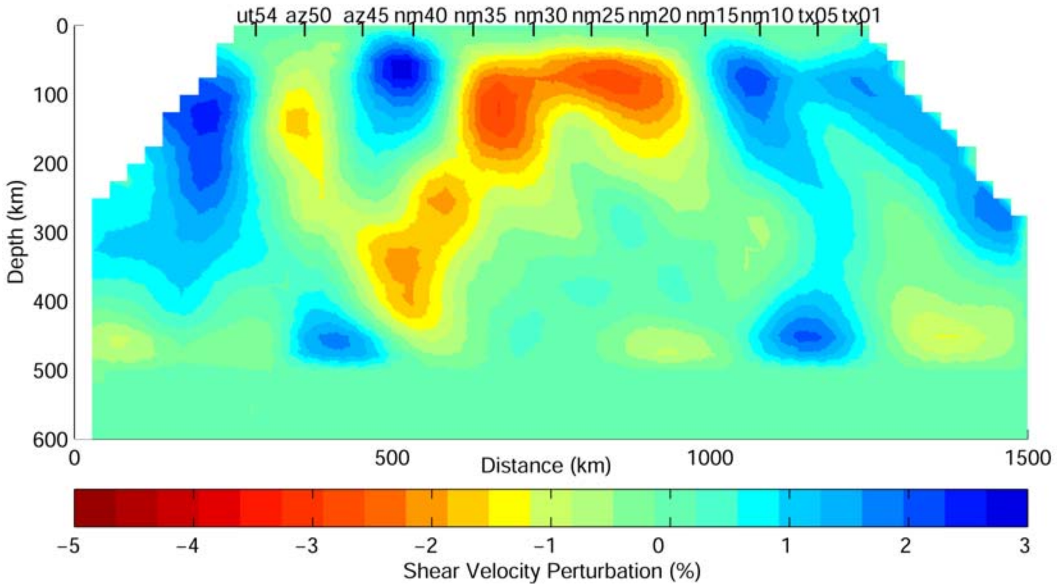

Figure 2.20 Tomography of a “squeezing” test (4). The velocity perturbations are limited to the region between 50 km and 500 km depth. Only fast anomalies expanded downward to the bottom of 500 km depth.

Anisotropy can play a role in P and S wave velocity variations in tomographic models as well as temperature variations, melting, and compositional variations. Shear wave splitting measurements have been made using the La Ristra seismic stations (Gok et al., 2003). The splitting is generally uniform across the array with a northeast oriented fast direction and thus it is unlikely that our neglect of anisotropy will produce large scale artificial laterally varying structures beneath the array. Relative variations of P and S wave velocities can also be diagnostic of the physical conditions that result in seismic heterogeneity.

The P and S data sets have different sampling of the mantle and we feel direct comparison of P and S from the models is likely to be uncertain. On the other hand, a direct comparison of P travel time residuals versus S travel time residuals involves less assumption in analyzing P versus S variations in models. Figure 2.21 shows a plot of S versus P travel time residuals for data where both P and S waves were measured from common earthquakes at common stations. There is a clear correlation between the two residual data sets. The best fitting least squares line through the data has a slope of 2.9. From the results of Karato (1993), one would expect the slope to be 2.9 for purely thermal effects assuming a Q_s of 89 and a Q_p of 200. The variance in travel time residuals is mostly due to the large heterogeneity within the upper 200 km of the models. Thus, we conclude that P and S heterogeneity above 200 km depth is primarily due to lateral changes in shallow mantle temperature. This is also consistent with the lateral changes in heat flow in the region (Morgan et al., 1986). Again using the results of Karato (1993), the maximum 8% variation in shear wave velocity in our model at 100 km depth implies a temperature variation of 470 K in temperature across the array. This is a large temperature variation but not unreasonable. Nataf and Ricard (1996) estimate a temperature difference at 100 km depth of a little over 500 K between asthenosphere and typical platform lithosphere. The Karato model assumes relatively strong anelastic effects on the temperature derivatives of seismic velocity and our calculations assume relatively low, but reasonable, Q values so that our estimate of the expected slope of the S versus P residual curve due to solid state thermal effects is likely on the high end. It is possible then, that a small amount of partial melt in the shallow mantle beneath the center of our line would be consistent with our seismic observations as this would increase the Poisson ratio further than a solid state temperature increase (Williams and Garnero, 1996).

Chemical and mineralogic variation can also affect seismic. The intrinsic variation in seismic velocity between fertile and infertile peridotite is relatively small (Humphreys and Dueker, 1994) so that it is unlikely that such variations are directly the cause of the seismic heterogeneity we observe. Water content can also affect seismic with hydrated minerals having slower velocity than a typical dry peridotitic mantle (Tyburczy et al., 1991; Christensen, 1996). It is seen that a narrow zone of low P and S is beneath station AZ50 near the Four Corners region.

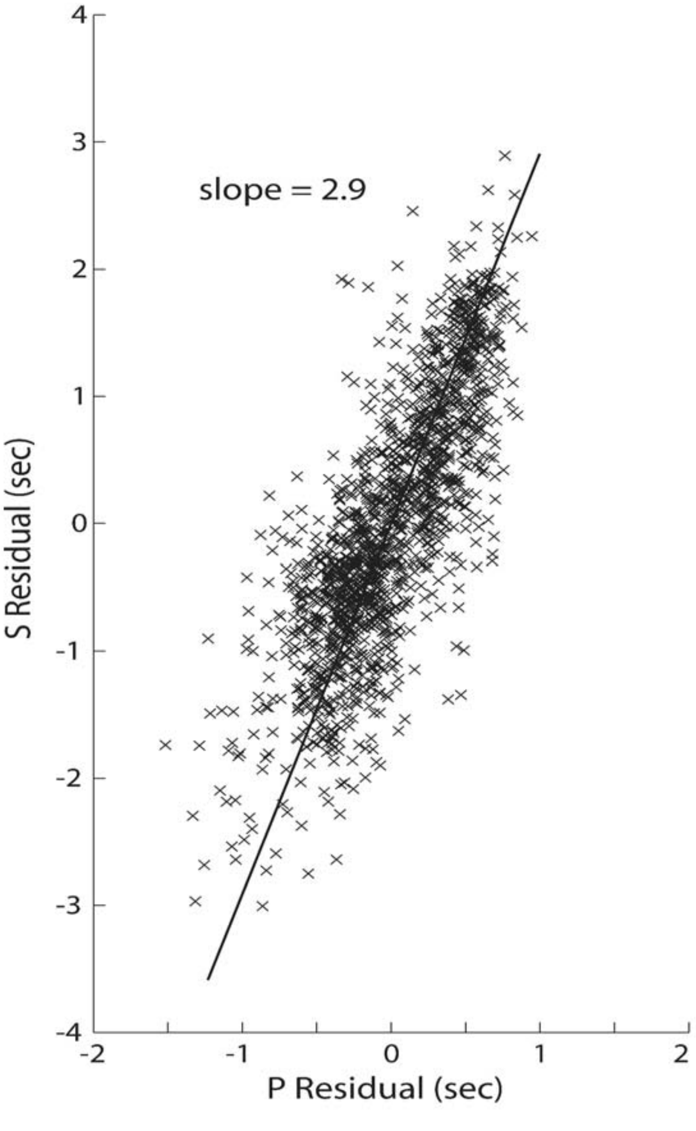

Figure 2.21 Plot of travel time residuals for P waves versus those S waves for common earthquakes and stations. The least squares fit line through the data has a slope of 2.9.

This area is associated with the Navajo volcanic field. Smith et al. (2002) have proposed, based on examination of mantle xenoliths, that a wedge of mantle beneath the Navajo volcanic field was hydrated from 70 to 35 Ma. They also propose that the hydration occurred preferentially within an old zone of weakness separating two Proterozoic terrains (Figure 2.1). The Four Corners region is near the southwestern end of the Colorado mineral belt. To the northeast a similar shortwavelength slow seismic anomaly has been observed in the mantle beneath Aspen, Colorado in the Colorado mineral belt (Dueker et al., 2001). Given the thick lithosphere beneath the Navajo field (West et al., 2003; Riter and Smith, 1996) and the relatively narrow width of the slow anomaly seen beneath station AZ50, it is possible the Four Corners seismic anomaly we see is due to the effect of hydration or chemical variation within the lithosphere of the Colorado Plateau. Serpentine has been found to have a very high Poisson ratio (Abers, 2000). Since the Four Corners anomaly is seen in P as well as S, it is unlikely that hydration alone is responsible for the anomaly and perhaps heat has been advected along with water and small amounts of melt.

2.8 Discussion

2.8.1 General issues

It is generally agreed that a flattening of the subducting Farallon plate and its subsequent removal from beneath the western United States has had a fundamental influence on the tectonic behavior of the region (see Humphreys et al., 2003 for a review). During flat slab subduction, the western U.S. lithosphere was under compression resulting in the Laramide orogeny and eastward migration of arc volcanism. Beginning about 40 Ma, it has been postulated that the flat slab beneath the western United States began to founder and roll back in some way (Figure 2.22) towards the west (Coney and Reynolds, 1977; Humphreys, 1995). The foundering of the slab implies a replacement of relatively cold slab with hot asthenospheric mantle in the shallow upper mantle, resulting in widespread ignimbrite volcanism and ultimately in large scale extension through a large part of the western United States. Within this general framework, however, the details of how the flat slab interacted with the western North America lithosphere and how the roll back of the slab affected the lithosphere are still controversial. One general issue of importance is the role of pre-existing lithosphere structure in controlling the tectonics of the region and how that lithosphere was modified during the flat slab subduction and subsequent removal. A second issue is the role of active mantle processes, especially in recent times, in the tectonic behavior of the southwestern United States. Is the extension and volcanism of the past 20 Ma or so due to passive collapse of thickened crust or are externally applied forces responsible or are there forces acting on the lithosphere due to dynamic processes in the deeper mantle beneath the lithosphere?

2.8.2 Lithosphere beneath the array

The images of the upper mantle beneath the La Ristra line (Figures 2.15 and 2.16) show lateral variations in P and S wave velocity at all depths. Above 200 km depth there is a clear relation between geologic province and mantle velocity. It is clear that regions that have exhibited magmatic and/or extensional activity during the past 40 Ma, the Rio Grande rift, the transition zone and the Navajo volcanic field, have slow mantle velocities beneath them bounded by mantle with relatively fast seismic velocity. The gradient in mantle seismic velocity also appears to be sharp between the regions. The slow anomalies beneath stations AZ50 (the Navajo field) and stations NM30-NM35 (the Jemez lineament) are both close to Proterozoic boundaries (Figure 2.1) (Karlstrom and Humphreys, 1998). This may imply a Proterozoic structural control on regions with mantle heating, melting, and deformation as proposed by Karlstrom and Humphreys (1998). The structural control may be related to variations in how fertile the mantle was and thus, how easily melt was generated, or to variations in fracture density that may have allowed easier melt and fluid migration through the lithosphere or perhaps to variations in the original thickness of the lithosphere (Humphreys et al., 2003; Smith et al., 2002). Removal of the flat Farallon slab and its replacement with hot asthenosphere about 30 Ma would then have modified the different lithospheres in different ways i.e. more fertile, fractured and thinner lithosphere would have generated more melt and been more

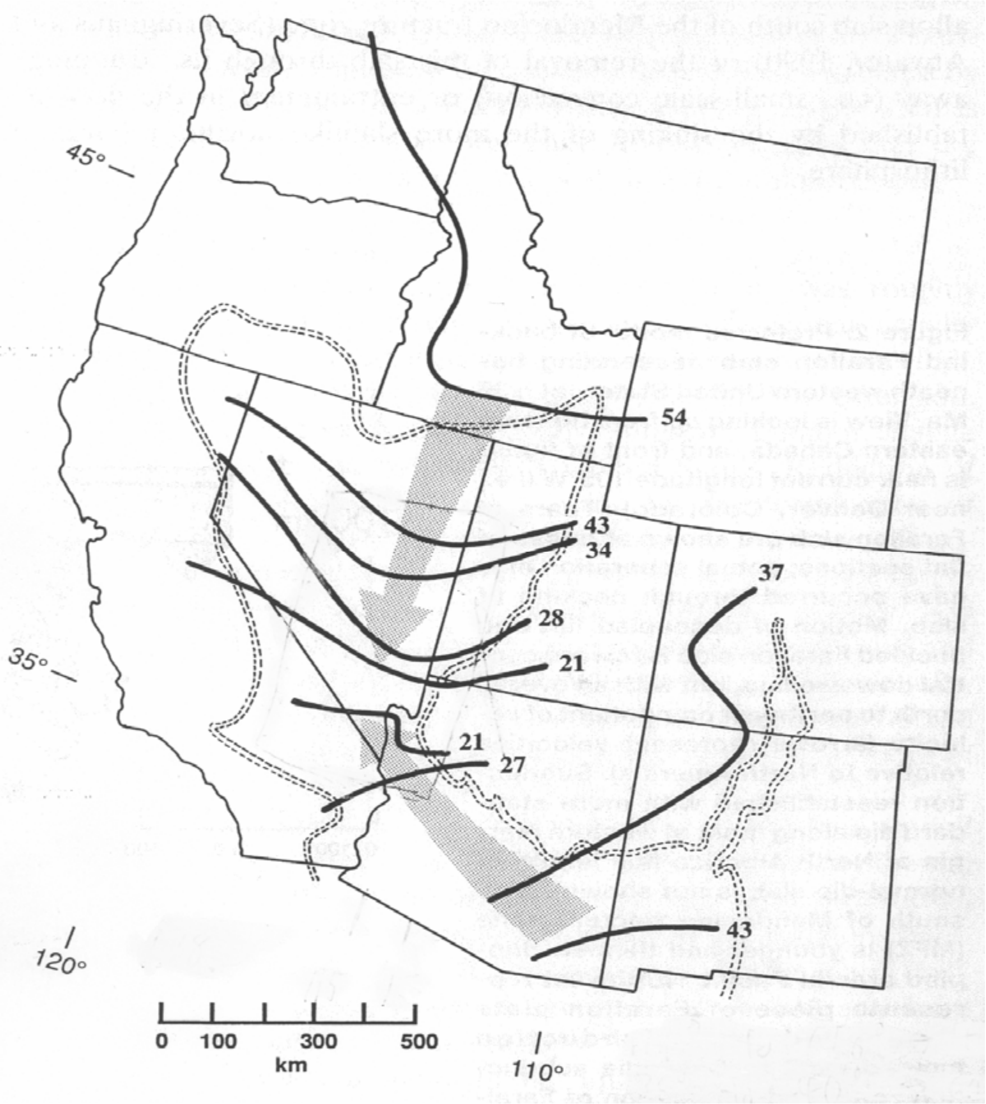

Figure 2.22 Map of propagating post-Laramide magmatic fronts. The heavy lines show the limits of magmatic advance toward southern Nevada at the times indicated (Ma, taken primarily from Christiansen and Yeats, 1992). The double line represents the current boundary of Basin and Range (from Humphreys, 1995).

mechanically weakened than surrounding lithosphere. At present, however, the seismic evidence discussed above indicates that most of the difference in mantle seismic velocity is due to temperature variations within the solid state. Also, there has been an increase in tectonic and magmatic activity during the past 10 Ma that is unlikely directly related to foundering of the Farallon plate 30 Ma. As discussed below, it may be that convection in the deeper mantle is responsible for recent magmatic and tectonic activity and that perhaps some of the older lithosphere beneath the Rio Grande rift and transition zone has been removed.

2.8.3 Seismic structure below 200 km depth

Below 200 km depth, the seismic variations are almost certainly related in some way to flow in the mantle, as this is below most estimates of lithosphere thickness. Buck (1986) and King and Ritsema (2000) showed that thinning of lithosphere due to extension should result in small scale convection due to the large lateral temperature differences created. Our seismically inferred lateral temperature variations are as large as Buck used in his calculations. Gao et al. (2003) claim to see evidence for such convection beneath the Baikal rift and the Rio Grande rift. In these studies upwelling occurs directly beneath the rift and downwellings occur symmetrically on either side of the rift. Our images show no indication of low seismic anomalies in the mantle beneath the rift below 150 km depth associated with upwelling mantle. Gao et al. (2003) claim that upwelling beneath the Baikal rift may align the a-axis of olivine in the vertical direction resulting in relatively fast P waves at near vertical incidence angle even if temperatures are hotter than average. This mechanism could explain the absence of deep slow P wave anomalies in our images but does not explain the absence of slow S wave anomalies. Thus we find no evidence for deep upwelling directly beneath the rift. However, we do see three large scale structures in the mantle below 200 km depth, labeled A, B, and C in Figures 2.15 and 2.16. Beneath the western edge of the model an eastward dipping high anomaly (A) is seen in the transition zone. Resolution is very poor here as the anomaly is off the edge of the line, thus the detailed shape of the anomaly is unknown although it is certain there is anomalously fast mantle in the region. Van der Lee and Nolet (1997) also imaged high velocity in the same location in their study of shear structure beneath North America. They interpret the transition zone anomaly near the Four Corners region to be the trailing edge of the Farallon plate. From the spatial progression of volcanism during the past 40 Ma (see Figure 2.22), it appears that the region near the western end of the La Ristra line is one of the last regions to have had the Farallon plate founder (Humphreys, 1995). Thus, we interpret the fast anomaly beneath the western part of the Ristra line to be remnant Farallon slab that may be stagnant in the transition zone or actively sinking. To the east of the slab anomaly is a region of slow seismic velocity (B) extending from near 500 km depth to the shallowest mantle (beneath seismic station 50). Resolution analysis and squeezing experiments indicate this feature is real. There appears to be some connection of the deeper slow anomaly with the strongest slow anomaly in the upper 200 km beneath Mount Taylor (station NM35) as well as with the Colorado mineral belt anomaly under station AZ50, both regions that have experienced recent volcanic activity. Thus it is likely that the deep slow anomaly represents some form of upwelling. The receiver function analysis of Wilson et al. (2003), however, shows no major deflection of the 410 km discontinuity in this region indicating it is unlikely that a large upwelling of hot mantle exists there. We suggest that the slow anomaly from 300 to 500 km depth beneath stations AZ45-AZ50 may be mantle that has been altered due to the release of water and other volatiles from the foundering Farallon slab just to the west. Recently, Bercovici and Karato (2003) have suggested that mantle that crosses the 410 km discontinuity from below would dehydrate due to the difference in water solubility between olivine and wadsleyite. They further suggest that partial melting could result just above 410 km depth due to this de-watering. The strongest part of anomaly B is indeed just above 410 km depth in our models and is stronger in S than P, perhaps indicating a small degree of partial melting. Previous studies have found indications of similar phenomena. Revenaugh and Sipkin (1994) interpreted a reversal near 330 km depth beneath eastern China as a melt layer associated with subduction to the east. Zhao et al. (1997) found a slow anomaly to 400 km depth associated with the subducting Pacific plate in the Tonga subduction zone and associate the anomaly with dehydration of the slab and arc as well as back arc volcanism seen at the surface. Nolet and Zielhuis (1994) interpret a slow shear wave anomaly at 300 to 500 km depth beneath the Tornquist zone as due to injection of water into the transition zone during ancient subduction. More recently, Abers (2000) has shown that hydrated oceanic crust exists to at least 250 km depth in subduction zones beneath Japan and Alaska, implying hydrous phases are carried beyond the volcanic front. The Farallon slab beneath the Four Corners region is likely very young and it is not clear if hydrous phases in young slab can be carried to great depth but the dehydration behavior of slabs is still uncertain. If the slow deep anomaly beneath the Four Corners region is thermal in origin it may be that the Farallon slab upon reaching depths near 600 km has disturbed a thermal boundary layer creating an instability that results in rising hot mantle. Tan et al. (2002) show this phenomenon in their simulations although the thermal boundary layer in their work is the core-mantle boundary.

At the eastern edge of the La Ristra line a fast seismic anomaly (C) is seen below 200 km depth beneath stations TX01-TX05. We interpret this narrow fast anomaly as a downwelling associated with convection. There is also some indirect evidence that such convection must be occurring or has occurred in the recent past. Based on Nd and Sr isotope ratios Perry et al. (1988) and McMillan et al. (2000) have determined that the source region of Rio Grande rift volcanic rocks has changed from lithosphere to asthenosphere during the last 10 Ma and perhaps as recently as 4 Ma. The Perry et al. (1988) study included analyses of basalts from the Lucero volcanic field just south of the La Ristra seismic line. Many of the younger volcanic rocks are alkali olivine basalts with isotopically depleted signatures. Alkali olivine basalt melt most likely forms at depths from 50 to 70 km (Perry et al., 1987) implying that the chemical lithosphere has thinned to less than those depths. Total extension across the rift at the location of the La Ristra line is on the order of 25% (Cather et al., 1994; Chapin and Cather, 1994) with most of the extension occurring prior to 20 Ma and a recent episode of increased extension during the last 10 Ma. Thus if the present lithosphere thickness is 60 km and it has thinned solely by extension then its original thickness would be just 75 km. The lithosphere thickness beneath the northern Rocky Mountains has been estimated to be 200 km and 100 km beneath the northern Rio Grande rift (Dueker et al., 2001) and Riter and Smith (1996) find evidence for at least a 140 km thick lithosphere beneath the Colorado Plateau 25 Ma. It is thus likely that the lithosphere under the Rio Grande rift was well over 75 km thick prior to the extensional events of the past 40 Ma even if it was originally thinner than beneath the surrounding regions. If this is so it implies that some of the chemical lithosphere, mantle rock that has been in place since perhaps the Proterozoic, has been physically displaced from beneath the Rio Grande rift region. The downwelling imaged in Figures 2.15 and 2.16 beneath the Great Plains may consist partially of deeper lithosphere originally beneath the Rio Grande rift that has been entrained by the convective flow beneath the rift. Active convection with concurrent removal of some of the lithosphere beneath the rift and surrounding regions may also explain the recent rejuvenation of tectonic activity in the region. A period of extension and volcanism occurred in the Rio Grande rift region from 40 to about 20 Ma. This tectonic activity can be explained in terms of the foundering of the Farallon slab thought to have begun about 40 Ma in the rift region. Following 20 Ma there was a slowing of extension within the rift and a lull in magmatic activity. Beginning 10 Ma extension across the rift accelerated, magmatic activity picked up, and, though controversial, possible significant uplift of the region occurred (Morgan et al. 1986; Baldridge et al., 1991). Also during this time interval the magma source in the southern rift changed from lithospheric to asthenospheric (Perry et al., 1988). This recent activity may be associated with removal of lithosphere by the convection that we infer from our seismic image.

Another interesting aspect of our seismic model is that the strongest slow anomaly is beneath stations NM30-NM35. These stations are located to the west of the Rio Grande rift, within the transition zone. Station NM35 is located on Mount Taylor, part of the Jemez lineament. The very shallow mantle is slow directly beneath the rift but below 100 km depth, the mantle seems to have normal wave velocities, at least relative to the very slow mantle to the west at those depths. West et al. (2004) have imaged the same structure in their analysis of surface wave dispersion along the Ristra line. If our interpretation of the seismic images in Figures 2.15 and 2.16 is correct, it appears as if deep upwelling (~400 km depth) is occurring beneath the San Juan basin (stations AZ45-AZ50) and is perhaps associated with volatiles from the Farallon slab to the west. This deep upwelling may be feeding the anomaly to 200 km depth beneath Mount Taylor. The mantle beneath the center of the rift may be fed through largely lateral flow from the Mount Taylor region above 100 km depth. In this scenario there would be an overall eastward flow of mantle from the Jemez region, across the rift, with sinking beneath the Great Plains. This is consistent with the generally eastward dip of the deep structures in our image.

The shear wave splitting observations of Gok et al. (2003) show the fast polarization direction to be approximately perpendicular to the Ristra line and therefore appear to be in contradiction to our model. The Gok et al. study used a very limited number of back azimuths in their study and the amplitude of the shear wave splitting varied by a factor of two across the line so that a detailed flow model can not be determined from their data alone. Gao et al. (1997) note that shear wave splitting in continental rifts has generally been found to have fast polarization directions parallel to the rift. They interpret this to indicate the anisotropy is due to alignment of fluid filled cracks perpendicular to the maximum tension axis and not to preferred alignment of olivine in the flow direction. This is consistent with the Gok et al. (2003) results and does not preclude a generally eastward flow generated by downwelling beneath the thick

Great Plains lithosphere. A further point to keep in mind is that our image is two dimensional and thus shows a projection of flow in just one direction, it clearly can not give the absolute flow direction in the region.

2.8.4 Small convection beneath the array

Figure 2.23 shows a cartoon model of our interpretation of the tomography images presented here. Upwelling from the deeper upper mantle, perhaps with higher than normal volatile content, is rising near the location of remnants of the sinking Farallon slab. The upwelling is causing melting in the shallow mantle under Mount Taylor and perhaps near the Navajo field. Both Mount Taylor and the Navajo field lie along Proterozoic suture zones that may have made the lithosphere more fertile there, thus more prone to melting, or more porous (Karlstrom and Humphreys, 1998; Smith et al., 2002). Downwelling of mantle is occurring beneath the thicker lithosphere of the Great Plains. Lithosphere under the Rio Grande rift and perhaps the transition zone, having already been weakened and thinned by previous extension, melting, and possibly hydration, has been mechanically removed to the east by the convective flow indicated by the Great Plains downwelling. This interpretation is based on a single cross section so that the actual direction of flow is undetermined. Fully three dimensional images should further clarify the dynamics beneath the region.

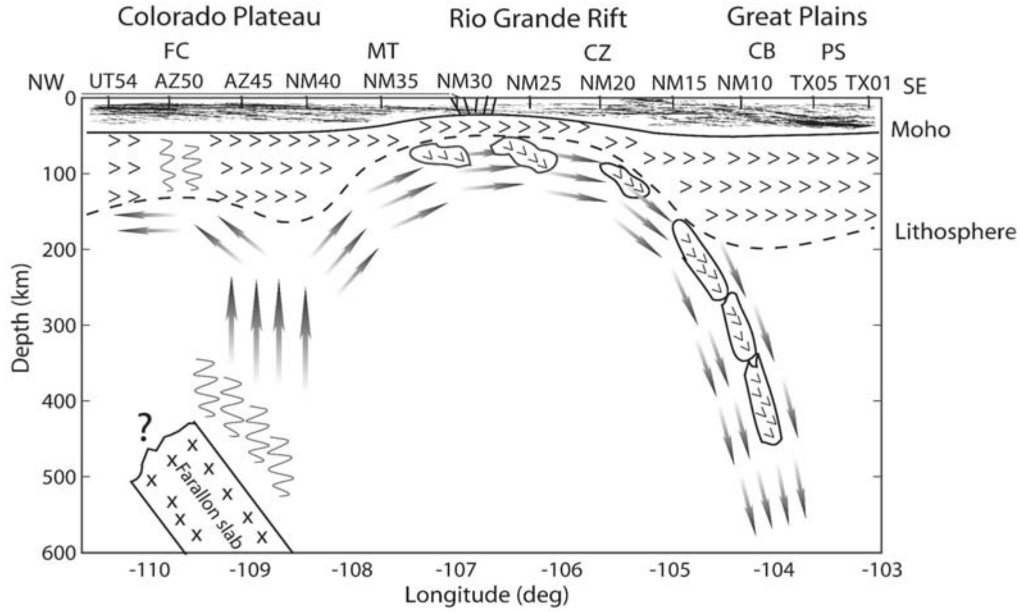

Figure 2.23 Schematic illustration of our interpretation of the present day mantle structure beneath the Rio Grande rift and surrounding regions. The full three dimensional flow of mantle in the region is unknown, but on the two-dimensional plane beneath the La Ristra line, we project certain features that are indicated by the tomography results. The stippled pattern in the shallow mantle indicates lithosphere. The arrows indicate mantle flow direction, and the wavy lines indicate mantle enriched in volatiles. Volatiles released from the Farallon plate are entrained in mantle upwelling, eventually rising under Mount Taylor. Downwelling is occurring under the Great Plains. In our model a significant portion of the lithosphere from Mount Taylor to Carrizozo has been removed and is entrained in the eastern downwelling. FC is the Four Corners region, MT is Mount Taylor, CZ is Carrizozo, CB is Carlsbad, NM, and PS is Pecos, TX.

2.9 Conclusion

Tomographic inversion of travel time delays recorded by the long and densely spaced La Ristra seismic line show variations in seismic wave velocity at all scales and depths in the upper mantle. The strongest variations are within the upper 200 km of the mantle, unsurprisingly, and correlate well with surface tectonic behavior. In particular, it is clear that the upper 100-200 km of mantle beneath the magmatically and tectonically active Rio Grande rift and transition zone to the Colorado Plateau is seismically distinct from the mantle beneath the stable Colorado Plateau and Great Plains. Furthermore, the boundaries between the active and stable mantle are very sharp and are located near ancient suture and shear zone boundaries indicating that old lithospheric structure plays a key role in tectonic behavior as suggested by Karlstrom and Humphreys (1998) and Dueker et al. (2002). The evolution of the mantle from a state of relative uniformity, in density at least, to the extremely heterogeneous state observed today is not clear. It is possible that some heterogeneity in fracture density, fertility, and lithosphere thickness existed since Precambrian times and that this affected the behavior of the lithosphere during flat slab subduction and subsequent rollback. In this scenario melting and lowering of viscosity would have preferentially occurred in lithosphere that was more fertile, fractured, and thinner. At present, it appears that most of the variation we see is due to temperature variations however. Convective removal of at least some of the lithosphere beneath the tectonically activated regions is likely to have occurred. Our seismic images of the deeper mantle, from 200 to 600 km depth, appear to show evidence for such convection with upwelling associated with the trailing edges of the Farallon plate and downwelling occurring under the thicker lithosphere of the Great Plains.

REFERENCES

Abers, G. A., 2000. Hydrated subducted crust at 100-250 km depth, Earth and Planet. Sci. Lett., 176, 323-330.

Aki, K., A. Christofferson, and E. S. Husebye, 1977. Determination of the three-dimensional seismic structure of the lithosphere, J. Geophys. Res., 82, 277-296.

Axelrod, D. I. And H. P. Bailey, 1976. Tertiary vegetation, climate and altitude of the Rio Grande depression, New Mexico-Colorado, Paleobiology, 2, 235-254.

Baldridge, W. S., F. V. Perry, D. T. Vaniman, L. D. Nealey, B. D. Leavy, A. W. Laughlin, P. R. Kyle, Y. Bartov, G. Steintz, and E. S. Gladney, 1991. Middle to late Cenozoic magmatism of the southeastern Colorado Plateau and central Rio Grande Rift (New Mexico and Arizona, U. S. A.); a model for continental rifting, Tectonophysics, 197, 327-354.

Beghoul, N., M. Barazangi and B. L. Isacks, 1993. Lithospheric structure of Tibet and western North America: Mechanisms of uplift and a comparative study, J. Geophys. Res., 98, 1,997-2,016.

Bercovici, D. and S. Karato, 2003. Whole mantle convection and the transition zone water filter, Nature, 425, 39-44.

Bird, P., 1984. Laramide crustal thickening event in the rocky mountain foreland and great plains, Tectonics, 3, 741-758.

Bird, P., 1988. Formation of the Rocky Mountains, western United States: A continuum computer model, Science, 239, 1,501-1,507.

Buck, W. R., 1986. Small-scale convection induced by passive rifting: the cause for uplift of rift shoulders, Earth and Planet. Sci. Lett., 77, 362-372.

Cather, S. M., R. M. Chamberlin, C. E. Chapin, and W. C. McIntosh, 1994. Straigraphic consequences of episodic extension in the Lemitar Mountains, central Rio Grande rift, in Keller, G. R. and Cather, S. M. eds., Basins of the Rio Grande rift: structure, stratigraphy, and tectonics setting, Geol. Soc. Am. Special Paper, 291, 157-170.

Chapin, C. E. and S. M. Cather, 1994. Tectonic setting of the axial basins of the northern and central Rio Grande rift, in Keller, G. R. and S. M. Cather eds., Basins of the Rio Grande rift: Structure, straigraphy, and tectonic setting, Boulder, Colorado, Geol. Soc. Am. Special Paper, G-3, 5-25.

Chase, C. G., J. A. Libarkin, and A. J. Sussman, 2002. Colorado Plateau: Geoid and means of isostatic support, International Geology Review, 44, 757-588.

Christensen, N. I., 1996. Poisson's ratio and crustal seismology, J. Geophys. Res., 101, 3,139-3,156.

Christiansen, R. L., and R. L. Yeats, 1992. Post-Laramide geology of the U. S. Cordilleran region, in Burchfiel, B. C., et al., eds., The Cordilleran orogen: Conterminous U.S.: Boulder, Corolado, Geological Society of America, Geology of North America, v. G-3, p. 261-406.

Coney, P. J. and S. J. Reynolds, 1977. Cordilleran Benioff zones, Nature, 270, 403-406.

Davis, P. M., P. Slack, H. A. Dahlheim, W. V. Green, R. P. Meyer, U. Achauer, A. Glahn, and M. Granet, 1993. Teleseismic tomography of continental rift zones,in Seismic Tomography: Theory and Practice, edited by H. M. Iyer and K. Hirahara, 397-439, Blackwell, London.

Dickinson, W. R. and W. S. Snyder, 1978. Plate tectonics of the Laramide orogeny, Mem. Geol. Soc. Am., 151, 355-366.

Dueker, K., H. Yuan, and B. Zurek, 2001. Thick-Structured Proterozoic lithosphere of the Rocky Mountain region, GSA Today, 11(12), 4-9.

Eaton, G. P., 1987. Topography and origin of the southern Rocky Mountains and Alvarado Ridge, in Continental Extensional Tectonics, Geological Soc Special Pub, 28, 355-369.

Ericksen, M. C. and R. Slingerland, 1990. Numerical simulations of tidal and wind-driven circulation in the Crteaceous Interior Seaway of North America, Geol. Soc. Am. Bull., 102, 1,499-1,516.

Evans, J. R. and U. Achauer, 1993. Teleseismic velocity tomography using the ACH method: theory and application to continental-scale studies, in

Seismic Tomography, Theory and Practice, edited by H. M. Iyer and K. Hirahara, pp. 319-360, Chapman and Hall, New York.

Gao, S. S., K. H. Liu, P. M. Davis, P. D. Slack, Y. A. Zorin, V. V. Mordvinova, and V. M. Kozhevnikov, 2003. Evidence for small-scale mantle convection in the upper mantle beneath the Baikal rift, J. Geophys. Res., 108, doi:10.1029/2002JB002039.

Gok, R., J. Ni, E. Snadvol, D. Wilson, W. S. Baldridge, R. Aster, M. West, S. Grand, W. Gao, F. Tilmann, and S. Semken, 2003. Shear wave splitting and mantle flow beneath the LA RISTRA array, Geophys. Res. Lett, 30(12), 1614, doi:10.1029/2002GL016616.

Grand, S. P., 1994. Mantle shear structure beneath the Americas and surrounding oceans, J. Geophys. Res., 99, 11,591-11,621.

Gregory, K. M. and C. G. Chase, 1992. Tectonic significance of paleobotanically estimated climate and altitude of the late Eocene erosion surface, Colorado, Geology, 20, 581-585.

Heller, P. L., K. Dueker, and M. McMillan, 2003. Post-Paleozoic alluvial gravel transport as evidence of continental tilting in the U. S. Cordilleran, Geol. Soc. Am. Bull., 115, 1,122-1,132.

Humphreys, E. D., 1995. Post-Laramide removal of the Farallon slab, western United States, Geology, 23, 987-990.

Humphreys, E. D. and K. G. Duecker, 1994. Physical state of the western U.S. upper mantle, J. Geophys. Res., 99, 9,635-9,650.

Humphreys, E. D., E. Hessler, K. Dueker, G. L. Farmer, E. Erslov, and T. Atwater, 2003. How Laramide-age hydration of North American lithosphere by the Farallon slab controlled subsequent activity in the western U. S., Int. Geol. Rev., 45, 575-595.

Karato, S., 1993. Importance of anelasticity in the interpretation of seismic tomography, Geophys. Res. Lett., 20, 1,623-1,626.

Karlstrom, K. E. and S. A. Bowring, 1988. Early Proterozoic assembly of tectonostratigraphic terranes in southwestern North America, J. Geology, 96, 561-576.

Karlstrom, K. E. and E. D. Humphreys, 1998. Persistent influence of Proterozoic accretionary boundaries in the tectonic evolution of southwestern North America: Interaction of cratonic grain and mantle modification events, Rocky Mountain Geology, 33, 161-179.

Keller, G. R., P. Morgan, and W. R. Seager, 1990. Crustal structure, gravity anomalies and heat flow in the southern Rio Grande rift and their relationship to extensional tectonics, Tectonophysics, 174, 21-37.

Kennett, B. L. N. and E. R. Engdahl, 1991. Traveltimes for global earthquake location and phase identification, Geophys. J. Int., 105, 429-465.

Lachenbruch, A. H. and J. H. Sass, 1977. Heat flow in the United States and the thermal regime of the crust in The Earth's Crust, Geophys. Monogr. Ser., vol 20, edited by J. G. Heacock, 626-675, AGU, Washington DC.

Lastowka, L. A., A. F. Sheehan, and J. M. Schneider, 2001. Seismic evidence for partial lithospheric delamination model of Colorado plateau uplift, Geophys. Res. Lett., 28, 1,319-1,322.

Lawton, T. F. and N. J. McMillan, 1999. Arc abandonment as a cause for passive continental rifting; Comparison of the Jurassic Mexican Borderland rift and the Cenozoic Rio Grande rift, Geology, 27, 779-782.

Livaccari, R. F. and F. V. Perry, 1993. Isotopic evidence for preservation of Cordilleran lithospheric mantle during the Sevier-Laramide orogeny, western United States, Geology, 21, 719-722.

McMillan, N. J., A. P. Dickin, and D. Haag, 2000. Evolution of magma source regions in the Rio Grande rift, southern New Mexico, Geol. Soc. Am. Bull., 112, 1,582-1,593.

McQuarrie, N., and C. Chase, 2000. Raising the Colorado Plateau, Geology, 28, 91-94.

Menk, W., 1989. Geophysical data analysis: discrete inverse theory, Academic Press, Inc..

Mitrovica, J. X., C. Beaumont, and G. T. Jarvis, 1989. Tilting of continental interiors by the dynamical effects of subduction, Tectonics, 8, 1,079-1,094.

Morgan, P., W. R. Seager and M. P. Golombek, 1986. Cenozoic thermal, mechanical and tectonic evolution of the Rio Grande rift, J. Geophys. Res., 91, 6,263-6,276.

Morgan, P. and C. A. Swanberg, 1985. On the Cenozoic uplift and tectonic stability of the Colorado Plateau, J. Geodyn., 3, 39-63.

Mosher, S., 1998. Tectonic evolution of the southern Laurentian Grenville orogenic belt, Geol. Soc. Am. Bull., 110, 1,357-1,375.

Nataf, H. C. and Y. Ricard, 1996. 3SMAC: An a priori tomographic model of the upper mantle based on geophysical modeling, Phys. Earth Planet. Inter., 95, 101-122.

Nolet, G., 1985. Solving or resolving inadequate and noisy tomographic systems, J. of Comp. Physics, 61, 463-482.

Nolet, G., 1987. Seismic wave propagation and seismic tomography, in Mathematical Geophysics, edited by Vlaar, Nolet Wortel, and Cloetingh, pp.155-187, D. Reidel Publishing Company.

Nolet, G., 1993. Solving large linearized tomographic problems, in Seismic Tomography, Theory and Practice, edited by H. M. Iyer and K. Hirahara, pp. 227-247, Chapman and Hall, New York.

Nolet, G. and A. Zielhuis, 1994. Low S velocities under the Tornquist-Teisseyre zone: Evidence for water injection into the transition zone by subduction, J. Geophys. Res., 99, 15,813-15,820.

Olsen, K. H., G. R. Keller, and J. N. Stewart, 1979. Crustal structure along the Rio Grande rift from seismic refraction profiles, in Rio Grande Rift: Tectonics and Magmatism, edited by R. E. Riecker, Am. Geophys. Union, Washington DC.

Paige, C. C., and M. A. Saunders, 1982. LSQR: An algorithm for sparse linear equations and sparse least squares, ACM Transactions on Mathematical Software, 8, 43-71.

Parker, E. C., P. M. Davis, J. R. Evans, H. M. Iyer, and K. H. Olsen, 1984. Upwarp of anomalous asthenosphere beneath the Rio Grande rift, Nature, 312, 354-356.

Pederson, J. L., R. D. Mackley, and J. L. Eddleman, 2002. Colorado Plateau uplift and erosion evaluated using GIS, GSA Today, 12(8), 4-10.

Perry, F. V., W. S. Baldridge, and D. J. DePaolo, 1988. Chemical and isotopic evidence for lithospheric thinning beneath the Rio Grande Rift, Nature, 332, 432-434.

Revenaugh, J. and S. A. Sipkin, 1994. Mantle discontinuity structure beneath China, J. Geophys. Res., 99, 21,911-21,927.

Riter, J. C. A. and D. Smith, 1996. Xenolith constraints on the thermal history of the mantle below the Colorado Plateau, Geology, 24, 267-270.

Sahagian, D., A. Proussevitch, and W. Carlson, 2002. Timing of Colorado Plateau uplift: Initial constraints from vesicular basalt-derived paleoelevations, Geology, 30, 807-810.

Saltzer, R. L. and E. D. Humphreys, 1997. Upper mantle P wave structure of the eastern Snake River Plain and its relationship to geodynamic models of the region, J. Geophys. Res., 102, 11,829-11,842.

Selverstone, J., A. Pun, and K. C. Condie, 1999. Xenolithic evidence for Proterozoic crustal evolution beneath the Colorado Plateau, GSA Bulletin, 111, 590-606.

Sinno, Y. A. and G. R. Keller, 1986. A Rayleigh wave dispersion study between El Paso, Texas and Albuquerque, New Mexico, J. Geophys. Res., 91, 6,168-6,174.

Slack, P. D., P. M. Davis, W. S. Baldridge, K. H. Olsen, A. Glahn, U. Achauer, and W. Spence, 1996. The upper mantle structure of the central Rio Grande rift region from teleseismic P and S wave travel time delays and attenuation, J. Geophys. Res., 101, 16,003-16,024.

Smith, D., 2000. Insights into the evolution of the uppermost continental mantle from xenolith localities on and near the Colorado Plateau and regional comparisons, J. Geophys. Res., 105, 16,769-16,781.

Smith, D., D. Moser, J. Connelly, K. Manser, and D. Schulze, 2002. U-Pb zircon ages of eclogites, garnetites, and Cenozoic rock-water reactions in Proterozoic mantle below the Colorado Plateau, Geol. Soc. Am. Abstracts, v. 34, 253.

Spakman, W., and G. Nolet, 1987. Imaging algorithms, accuracy and resolution in delay time tomography, in Mathematical Geophysics, edited by Vlaar, Nolet, Wortel, and Cloetingh, pp.155-187, D. Reidel Publishing Company.

Spence, W., and R. S. Gross, 1990. A tomographic glimpse of the upper mantle source of magmas of the Jemez lineament, New Mexico, J. Geophys. Res., 95, 10,829-10,849.

Spencer, J. E., 1996. Uplift of the Colorado Plateau due to lithosphere attenuation during Laramide low-angle subduction, J. Geophys. Res., 101, 13,595-13,609.

Thompson, G. A., and M. L. Zoback, 1979. Regional geophysics of the Colorado Plateau, Tectonophysics, 61, 149-181.

Tyburczy, J. A., T. S. Duffy, T. J. Ahrens, and M. A. Lange, 1991. Shock wave equation of state of serpentine to 150 GPA: Implications for the occurrence of water in the Earth's lower mantle, J. Geophys. Res., 96, 18,011-18,028.

Van der Sluis, A., and H. A. van der Vorst, 1988. Numerical solution of large, sparse linear algebraic systems arising from tomographic problems, in Seismic Tomography, edited by G. Nolet, pp49-83, D. Reidel Publishing Company.

Van der Lee, S. and G. Nolet, 1997. Seismic image of the subducted trailing fragments of the Farallon plate, Nature, 386, 266-269.

West, M., J. Ni, S. Baldridge, D. Wilson, R. Aster, W. Gao, and S. Grand, 2004. Crust and upper mantle shear wave structure of the southwest United States J. Geophys. Res., 109, B03310, doi:1029/2003JB002575.

Williams, Q. and E. J. Garnero, 1996. Seismic evidence for partial melt at the base of Earth's mantle, Science, 273, 1,528-1,530.

Zhao, D., Y. Xu, D. A. Wiens, L. Dorman, J. Hildebrand, and S. Webb, 1997. Depth extent of the Lau back-arc spreading center and its relation to subduction processes, Science, 278, 254-257.

Table 2.1 Location of the La Ristra stations

Station name	Latitude	Longitude	Elevation(m)	Deployment Period
TX01	31.4247	-103.1040	750	1999-09-11 2001-05-16
TX02	31.5140	-103.2050	765	1999-09-11 2000-12-31
TX03	31.6230	-103.3230	831	1999-09-01 2001-05-16
TX04	31.7330	-103.4460	833	1999-09-11 2001-03-11
TX05	31.8790	-103.6070	873	1999-09-11 2001-05-16
TX06	31.9670	-103.7070	899	1999-10-30 2001-03-11
NM07	32.0854	-103.8400	966	1999-09-11 2001-03-25
NM08	32.1967	-103.9710	886	1999-09-11 2001-03-11
NM09	32.3290	-104.1210	893	1999-09-11 2001-05-15
NM10	32.4710	-104.2710	929	1999-09-12 2001-03-11
NM11	32.5838	-104.4090	974	1999-09-11 2001-05-15
NM12	32.6800	-104.5100	1066	1999-09-11 2001-03-12
NM13	32.8003	-104.6520	1177	1999-09-13 2001-05-16
NM14	32.9100	-104.7640	1219	1999-09-10 2001-03-12
NM15	33.0150	-104.9090	1342	1999-09-13 2001-05-16
NM16	33.1757	-105.1250	1625	1999-09-12 2001-03-12
NM17	33.2570	-105.1790	1705	1999-09-18 2001-05-15
NM18	33.4046	-105.3400	1624	1999-09-13 2001-05-15
NM19	33.4900	-105.4500	2028	1999-10-01 2000-07-06
NM20	33.6047	-105.5940	2034	1999-09-16 2001-03-10
NM21	33.7328	-105.7450	2000	2000-05-25 2001-05-01
NM22	33.8403	-105.8690	1691	1999-10-01 2001-03-04
NM23	33.9499	-106.0130	1813	1999-10-02 2001-05-01
NM24	34.0469	-106.1200	1874	1999-01-02 2001-01-31
NM25	34.1669	-106.2600	1933	1999-07-05 2001-05-02
NM26	34.2622	-106.3640	1854	1999-07-06 2001-03-05
NM27	34.3857	-106.5240	1870	1999-07-06 2001-05-02
NM28	34.5399	-106.7010	1484	1999-07-06 2001-03-03
NM29	34.6470	-106.8490	1561	1999-07-08 2001-03-04
NM30	34.7541	-106.9800	1515	1999-09-15 2001-03-03
NM31	34.8478	-107.0990	1676	1999-11-10 2001-05-02
NM32	34.9805	-107.2640	1685	1999-09-15 2000-12-28
NM33	35.1109	-107.4230	2094	1999-05-22 2001-05-03
NM34	35.2690	-107.6410	2735	1999-08-28 2000-09-05
NM35	35.3448	-107.7070	2133	1999-08-05 2001-05-04
NM36	35.4506	-107.8200	2176	1999-08-05 2001-03-07
NM37	35.5779	-108.0050	2254	1999-08-04 2001-05-09
NM38	35.6998	-108.1630	2077	1999-07-28 2000-11-16
NM39	35.7853	-108.2780	1949	1999-07-28 2001-05-09

Table 2.1 Location of the La Ristra stations cont.

Station name	Latitude	Longitude	Elevation (m)	Deployment Period
NM40	35.9450	-108.4290	1796	1999-07-07 2001-03-06
NM41	36.0353	-108.5700	1718	1999-07-29 2001-05-09
NM42	36.1485	-108.7170	1794	1999-07-28 2001-03-18
NM43	36.2495	-108.8870	1991	1999-11-15 2001-03-18
NM44	36.4215	-108.9580	1921	1999-07-28 2001-05-09
AZ45	36.4543	-109.0840	2683	1999-08-11 2000-10-21
AZ46	36.5569	-109.2190	2009	1999-07-29 2001-05-09
AZ47	36.6352	-109.3340	1752	1999-07-30 2001-03-17
AZ48	36.7598	-109.5390	1664	1999-08-10 2001-05-10
AZ49	36.9233	-109.6490	1512	1999-07-30 2001-03-16
AZ50	36.9762	-109.8640	1469	1999-07-29 2001-05-10
UT51	37.0900	-110.0090	1498	1999-07-29 2001-03-16
UT52	37.2363	-110.1360	1671	1999-07-29 2001-05-10
UT53	37.3460	-110.3310	1291	1999-11-13 2001-03-17
UT54	37.4187	-110.5060	1439	1999-11-14 2001-03-17
MB01	33.3363	-106.0339	1446	2000-03-25 2001-05-01
MB04	34.0738	-106.9201	1414	1999-07-01 1999-11-09
MB04B	34.0709	-106.9422	1489	2000-03-08 2001-05-25
MB05	34.6636	-108.0113	2143	2000-03-18 2000-06-25
ANMO	34.9462	-106.4567	1740	1988-01-01

Chapter 3

UPPER MANTLE SEISMIC STRUCTUE BENEATH EASTERN MEXICO

3.1 Abstract

We present compressional (P) and shear (S) wave seismic velocity models for the upper mantle beneath southeastern Mexico derived from waveform inversion of triplicated seismic phases. The seismic waveform data produced by an earthquake located near the Mexico-Guatemala border were recorded by the La Ristra passive seismic array. The La Ristra seismic array consisted of 54 broadband seismometers arranged linearly from west Texas to southeastern Utah. The orientation of the La Ristra array is nearly along the great circle from the event and the distance (18.5º-26.5º) of the seismic array from southern Mexico is such that the data are ideal for investigating localized seismic structure of the upper mantle. Previous tomography and receiver function studies provide a-priori knowledge of receiver-side crustal and upper mantle structure from which static adjustments were made to the seismic data. The waveforms were inverted for mantle velocity from 300 to 700 km depth using a conjugate gradient algorithm. In the inversion, we evaluated a suite of starting models with different depths of the 410 km and 660 km discontinuities and varying velocity gradients. The best

fitting models have velocity increases across the 410 km discontinuity of 6.2% and 7.3% for P- and S-wave velocities, respectively. The velocity jump across the 660 km discontinuity was found to be 3.3% for P-waves and 6.3% for S-waves. The size of the upper mantle discontinuities we find are more in agreement with a pyrolite composition than standard reference models imply. A common feature of the best-fitting models is a low-velocity zone above the 410 km discontinuity that is more prominent in the shear velocity model than the compressional velocity model. This feature may be due to partial melting induced by water release from the transition zone as proposed by Revenaugh and Sipkin (1994) and Song et al. (2004). The overall jump in velocity at 410 km is also larger than in previously published models with a lower gradient below. In addition, the P-wave data require a small discontinuity at 490 km depth that is not resolved in the S data. Finally, the S-wave data require an unusually high gradient beginning at about 600 km depth extending to the 660 km discontinuity. This feature may be due to a thermal and/or mineralogic anomaly associated with a flat lying slab beneath eastern Mexico.

3.2 Introduction

The seismic structure of the upper mantle is a fundamental constraint for understanding the mineral and chemical composition of the mantle as well as the dynamics of the Earth. Compressional and shear wave velocities are sensitive to temperature variations, melt content, mineralogy, and chemical composition and provide our most direct observations of these properties in the mantle below about 200 km depth. Seismic observations have shown that the upper mantle is highly variable laterally but that there are features common to most regions. In particular, there are two significant and ubiquitous seismic velocity discontinuities in the upper mantle, the 410 km and 660 km discontinuities, which form the boundaries of the transition zone in the upper mantle. It is believed that the 410 km discontinuity results from a phase transition of olivine to the wadsleyite structure and the 660 km discontinuity is caused by the dissociation of ringwoodite to perovskite and magnesiowüstite (ex. Bina and Helffrich, 1994). Recent seismic observations also indicate that there may be a small global discontinuity near 520 km depth (Shearer, 1990; Tajima and Grand, 1995 and 1998; Ryberg et al., 1997; Simmons and Gurrola, 2000; Deuss and Woodhouse, 2001; Helffrich et al., 2003) that may represent an intermediate phase transition from the wadsleyite to ringwoodite structure (Sinogeikin et al., 2003; Li, 2003). Other minerals also go through phase changes with depth in the upper mantle leading to high gradients and other possible jumps in seismic velocity. Adding to the complexity in interpreting seismic models is that the pressure at which phase changes occur changes with temperature, chemical heterogeneity and water content (Bina and Wood, 1984; Flanagan and Shearer, 1998).

A commonly used model for the composition of the upper mantle is pyrolite. The pyrolite model was developed by Ringwood (1975) and its primary mineralogic constituents are olivine (57% by weight) with less common clinopyroxene, orthopyroxene, and garnet. As mentioned above, the phase changes that the olivine portion of the upper mantle undergoes are thought to explain the jumps in velocity near 410 and 660 km depth, respectively. In theory, if mineral physics experiments can determine the seismic velocity jumps associated with the olivine to wadsleyite phase change and the ringwoodite to perovskite and magnesiowüstite dissociation then the observed seismic velocity jumps near 410 and 660 km depth can be used to infer the olivine content of the mantle. Bass and Anderson (1984) compared the best mineral physics prediction of seismic velocity associated with the pyrolite model to published seismic models and found the pyrolite model did not fit the seismic models. They found a better fit was obtained with an upper mantle composition containing only 16% olivine and far more clinopyroxene than in the pyrolite model. Their results were controversial at the time (Bina and Wood, 1987; Weidner, 1985) but a more recent comparison of mineral physics predictions of the pyrolite model versus published seismic models by Li et al. (1998) has found that, indeed, the pyrolite model does not produce an acceptable fit to standard seismic models of the upper mantle. Li et al. (1998) go further and state that no single chemical composition of the mantle satisfies the seismic profiles over the depth range 400 to 650 km.

Cammarano et al. (2005) have reexamined the consistency of a pyrolite upper mantle with seismic constraints. The seismic constraints used in their study are a global set of P and S travel times as well as the periods of the free oscillations of the Earth. They also use a range of different mineral physics parameters and find a small subset of mineral physics parameters that predict seismic velocities consistent with the seismic data for a pyrolite composition.

It is clear that better constrained mineral physics measurements of bulk and shear moduli of high pressure mineral phases will be necessary to uniquely determine upper mantle composition. However, given the strong lateral variations in temperature and possibly composition within the upper mantle, it will also be necessary to determine upper mantle P and S velocity structure within specific regions to compare directly to mineral physics predictions. Commonly, reference seismic models like PREM (Dziewonski and Anderson, 1981) or AK135 (Kennett et al, 1995) are used for comparison to mineral physics predictions. These models satisfy the travel times of a global set P and S data and thus have large error bars as well as little resolution of the details of discontinuity structure and gradients. Global tomography is a powerful tool to image three-dimensional seismic velocity variations but resolution is still quite limited (see Romanowicz, 1991 for a review) and detailed gradients and discontinuity structure are still not available from such techniques. The use of underside reflected precursors of SS and PP waves (Shearer and Flanagan 1999; Gu et al., 2003) or converted Ps or Sp waves have also been powerful techniques to investigate upper mantle seismic structure. These type studies provide strong constraints on topography of upper mantle discontinuities and the impedance contrast across the discontinuities. Although it is possible to determine the velocity jump across the discontinuity by using the amplitude versus angle of incidence of reflected or converted waves, there are usually high uncertainties in the results. Also, these techniques provide no information on velocity gradients between discontinuities. The data most sensitive to seismic velocity as a function of depth in the upper mantle are P and S waves that turn within the upper mantle. The discontinuities within the upper mantle produce triplications for these waves and thus complicated waveforms but these complications can be used to place tight constraints on velocity variations with depth (Walck, 1984; Grand and Helmberger, 1984; Nolet et al., 1994).

Upper mantle turning waves have yielded detailed models of the transition zone; however, they are often constructed by trial-and-error with a non-ideal source receiver distribution and few are generated with compressional and shear waves that are produced by the same earthquakes. Hence the resolution that these seismic models provide of the upper mantle is difficult to assess. Another problem is that a 1D model is extracted from data that actually sample fully three dimensional structures and it has been difficult to assess the effects of the 3D variations on the model. In this paper we use a waveform inversion technique applied to an optimal data set of P and S upper mantle turning waves generated from one earthquake to derive 1D P and S velocity models of the transition zone beneath eastern Mexico. The waveform inversion approach overcomes the deficiency of the trial-and-error modeling by producing an optimal data fit with some a-priori constraints. The data set we use is also ideal in that it consists of a densely spaced line of broadband seismic recordings aligned with the great circle path from the earthquake source. Finally, P and S tomography inversions have been conducted beneath the array so there is some constraint on the lateral variations in velocity sampled by the data.

3.3 Data and analysis

The Colorado Plateau, Rio Grande rift and Great Plains Seismic Transect (La Ristra) experiment consisted of 54 broadband seismometers deployed from August 1999 to May 2001. The stations were deployed in a line beginning in west Texas, crossing the Rio Grande rift and ending in the center of the Colorado Plateau spanning about 950 km (Gao et al., 2004). In this paper we used Ristra data produced by an earthquake occurring near the border between Guatemala and Mexico (see Table 3.1). The La Ristra array spanned 18.5 to 26.5 degrees in distance along the surface from the earthquake epicenter and the orientation of the array was approximately along a great circle with the event source (Figure 3.1). This makes these data ideal for investigating the detailed seismic structure in the transition zone of the upper mantle beneath eastern Mexico. We searched for

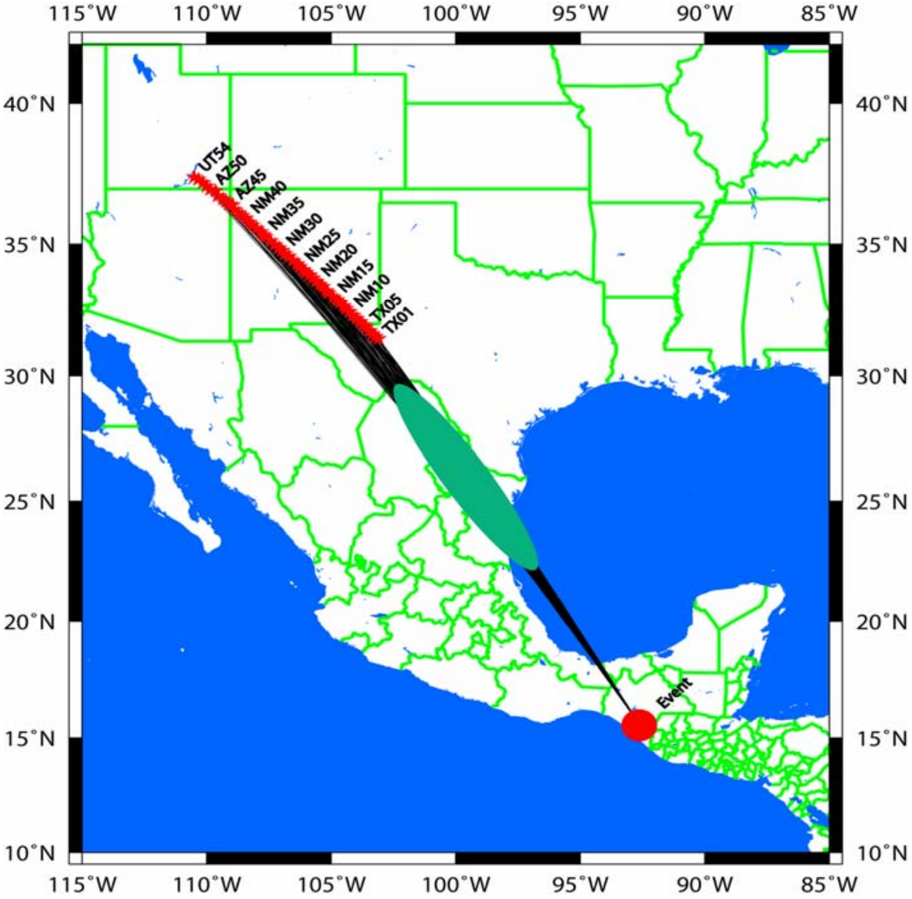

Figure 3.1 Map of the location of the La Ristra array seismic stations and the earthquake used as a source for the data used in this study. The great circle paths between the event and stations are also shown. The ellipse presents the area where the waves turn and thus sample the transition zone.

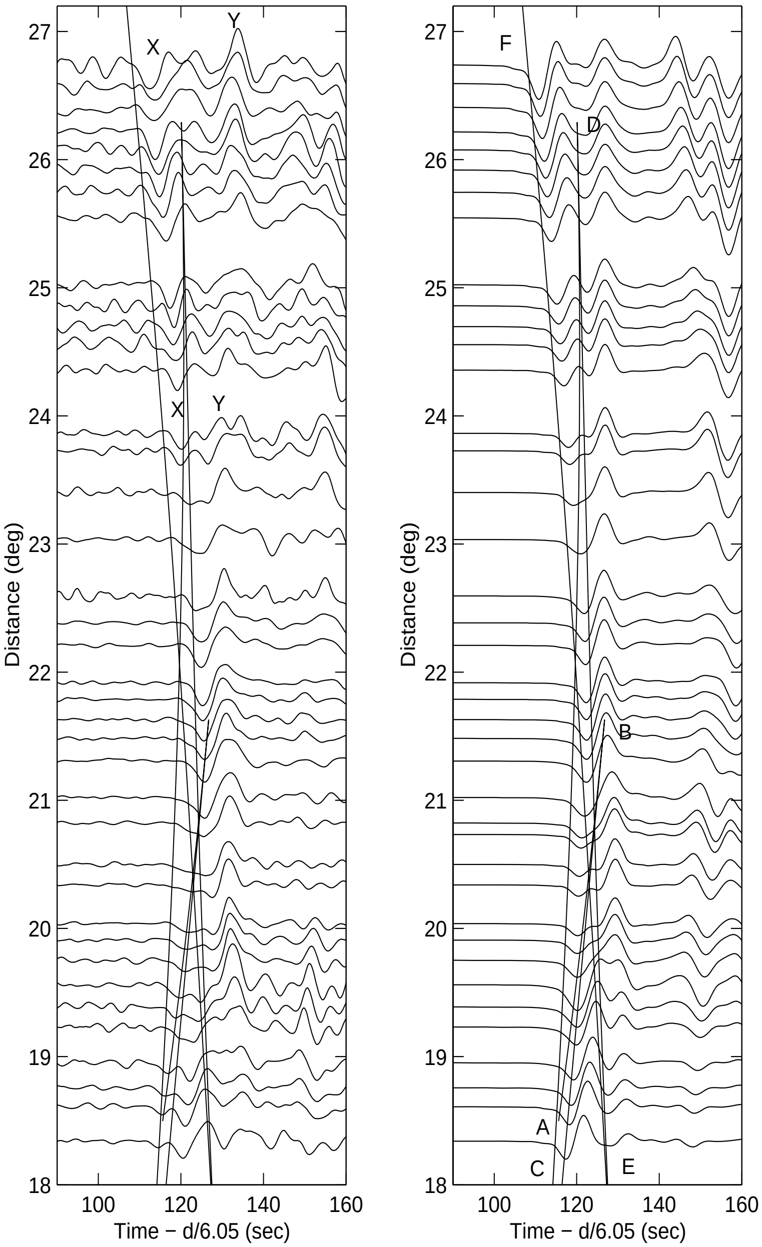

Figure 3.2 S wave seismograms and synthetics. On the left are tangential component seismograms, and on the right are synthetics calculated from the IASPEI model. The IASPEI predicted travel time curves are overlayed on both the data and synthetics.

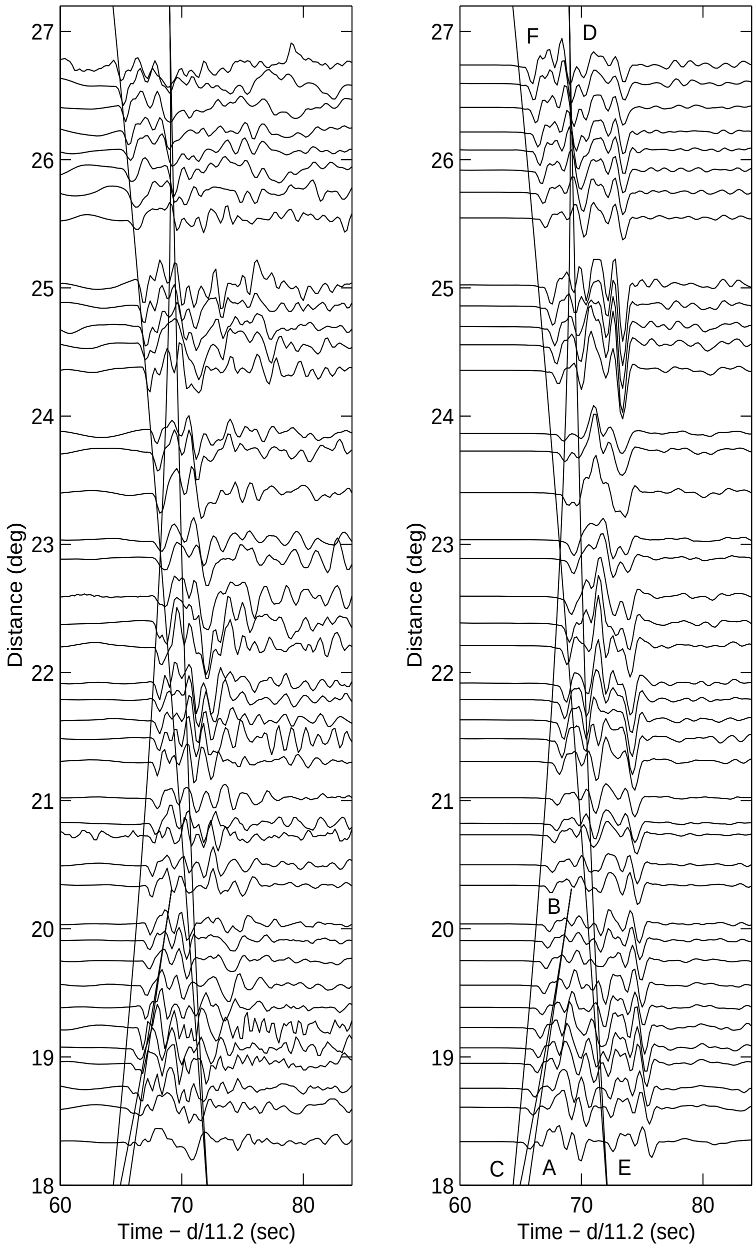

Figure 3.3 P wave seismograms and synthetics. On the left are vertical component seismograms, and on the right are synthetics calculated from the IASPEI model. The IASPEI predicted travel time curves are overlayed on both the data and synthetics.

other earthquakes in the same region but the January 19, 2001 event was the only one that produced both clear P and S waves. The earthquake depth is 82 km resulting in upgoing pP and sS waves arriving later than the triplicated arrivals from the transition zone. Figure 3.2 (on the left) shows the Ristra S-wave recordings (tangential component) and Figure 3.2 (on the right) shows synthetic seismograms computed using the IASP91 (Kennette and Engdahl, 1991) shear velocity model. The synthetics were computed using the reflectivity technique (Fuchs and Muller, 1971). The seismograms in Figure 3.2 (on the left) were bandpass filtered from 0.01 to 0.25 Hz. Figure 3.3 show the vertical component P wave data (on the left) and P wave synthetics (on the right) computed using the IASP91 model. The P wave data were bandpassed filtered from 0.01 to 1.5Hz. The observed seismograms were shifted in time to account for topography and crustal thickness variations along the line such that the arrival times of the data should correspond to those expected for a 35 km thick crust with zero topography. We also plot the predicted travel times by the IASP91 model on Figures 3.2 and 3.3 and mark different branches with letters. Branches AB, CD, and EF stand for arrivals that turn above 410 km, within the transition zone, and below the 660 km respectively (see Figures 3.4 and 3.5). We used the crustal model of Wilson et al. (2005) and rayparameters predicted by the IASP91 model to make the corrections. Gao et al. (2004) inverted P and S data recorded by Ristra stations and produced a 2D P and S velocity model of the upper mantle beneath the array. Their model has

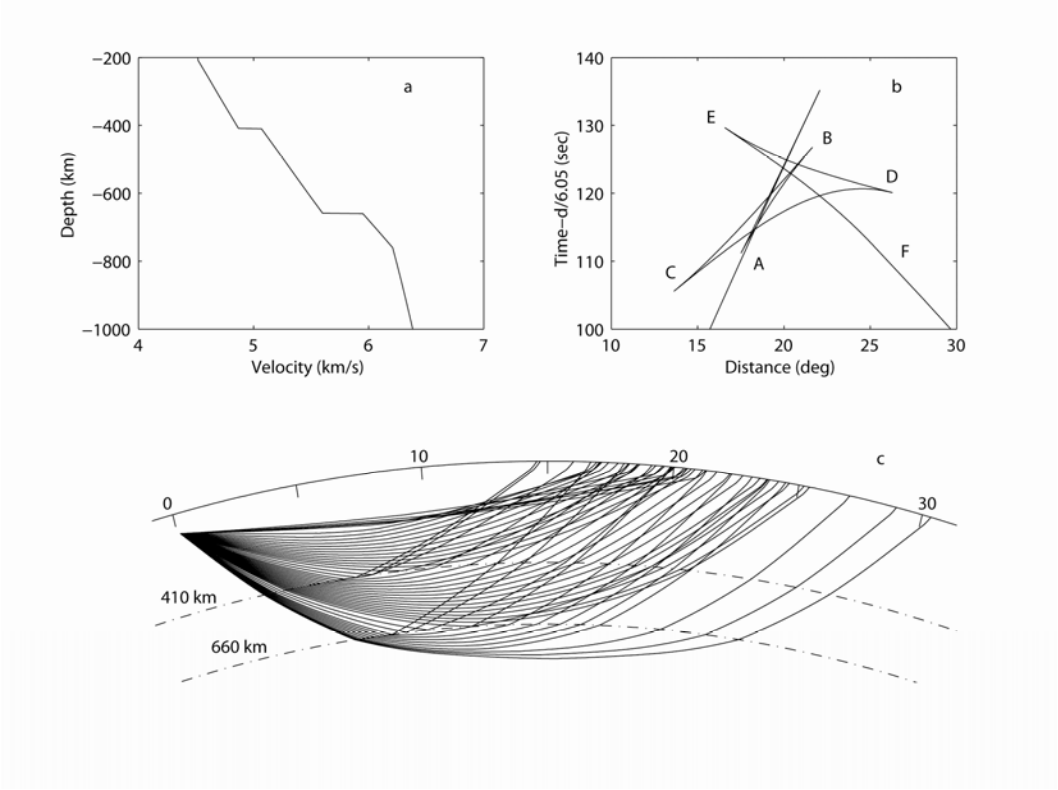

Figure 3.4 (a) The IASPEI shear velocity model. (b) Travel time curve for the IASPEI shear velocity model for a source at 80 km depth. (c) The raypaths for the IASPEI shear velocity model.

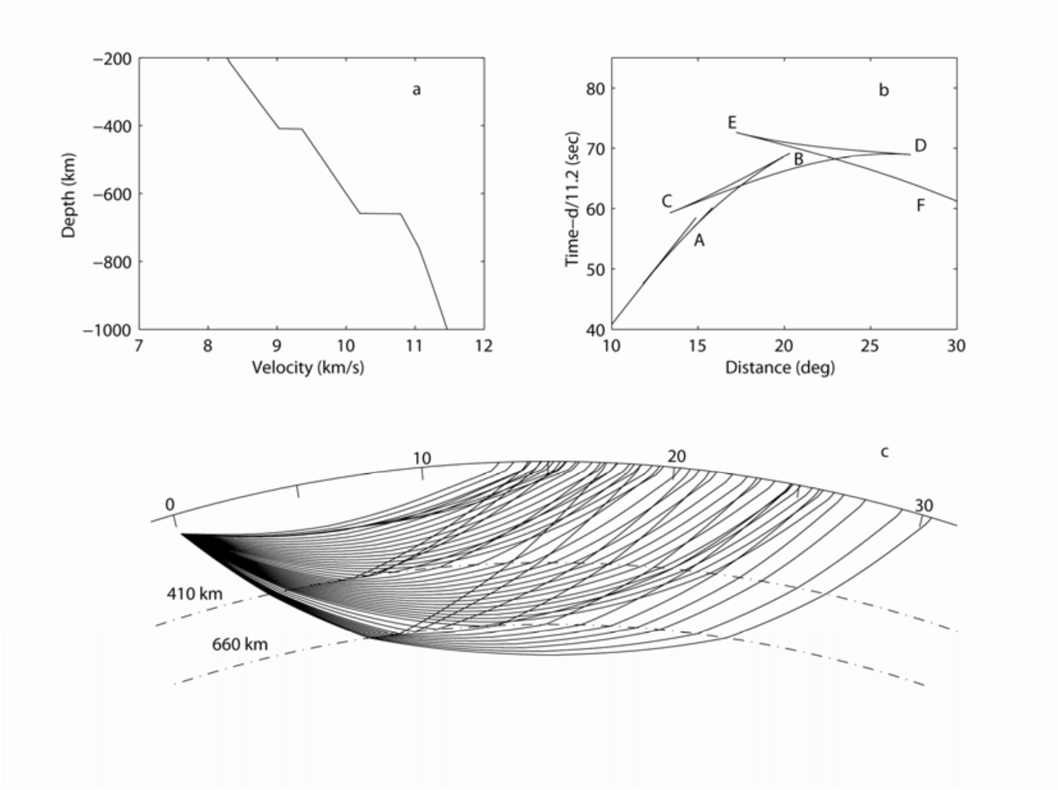

Figure 3.5 (a) The IASPEI compressional velocity model. (b) Travel time curve for the IASPEI compressional velocity model for a source at 80 km depth. (c) The raypaths for the IASPEI compressional velocity model.

significant heterogeneity in the upper 200 km of the mantle beneath the array. To account for this we traced rays using the IASP91 model from the earthquake to the array and calculated the relative timing shifts due to the shallow heterogeneity beneath the stations. The data, both P and S, were shifted to account for these timing variations due to shallow mantle lateral heterogeneity.

At the distances shown in Figures 3.2 and 3.3 P and S waves interact with upper mantle discontinuities resulting in triplicated waveforms. Figure 3.4 shows the S wave IASP91 model as well as the raypaths and travel time curves predicted by the model for upper mantle distances. Figure 3.5 shows the P wave IASP91 model as well as the raypaths and travel time curves predicted by the model for upper mantle distances. Both the P and S models predict similar triplicated arrivals. Branch AB represents arrivals that turn above the 410 km discontinuity. Branch CD represents arrivals turning within the transition zone from 410 to 660 km depth. Finally, branch EF corresponds to waves that have turned below the 660 km discontinuity. The time separation of different branches with distance is most sensitive to the overall velocity increase across the respective discontinuity. Clear multiple arrivals are seen in the data in Figure 3.2 (on the left). For example, arrivals labeled X and Y in Figure 3.2 (on the left) can be seen to separate with distance. The IASP91 model predicts two arrivals separating with distance but note that in the data the arrivals separate much faster than IASP91 predicts. Multiple arrivals are also clearly seen at closer distances in the S wave data but although the IASP91 model predicts multiple arrivals at those distances the predicted relative timing is off and thus the waveforms appear quite different.

The compressional wave seismograms (on the left in Figure 3.3) appear more complex than the S wave data. This is primarily due to the source mechanism of the earthquake as well as the intrinsically higher frequency of the P data than the S data. The P waves in Figure 3.3 (on the left) are near nodal for the Harvard mechanism given in Table 3.1 and the subevents producing the P waves actually change polarity. The SH waves are in the center of the radiation pattern and the source subevents are all of the same polarity. At longer periods noise dominates the vertical components. Beyond 26° there are no large secondary P phases due to upper mantle discontinuities and thus the seismograms at those distances in Figure 3.3 essentially represent the P wave source. We modeled the waveforms at large distance to determine the source function used in the synthetics (on the right in Figure 3.3). Despite the complicated source for the P waves, triplicated arrivals are apparent in the data. Figure 3.6 shows seismograms over a 2° distance range. Note the two pulses that at short distance are clearly distinct but cross at larger distance. The IASP91 model does not predict this behavior but a small jump in velocity near 500 km depth will produce a similar pair of arrivals that cross near 19° distance. At other distances careful analysis shows other multiple arrivals in the P data due to the upper mantle triplications

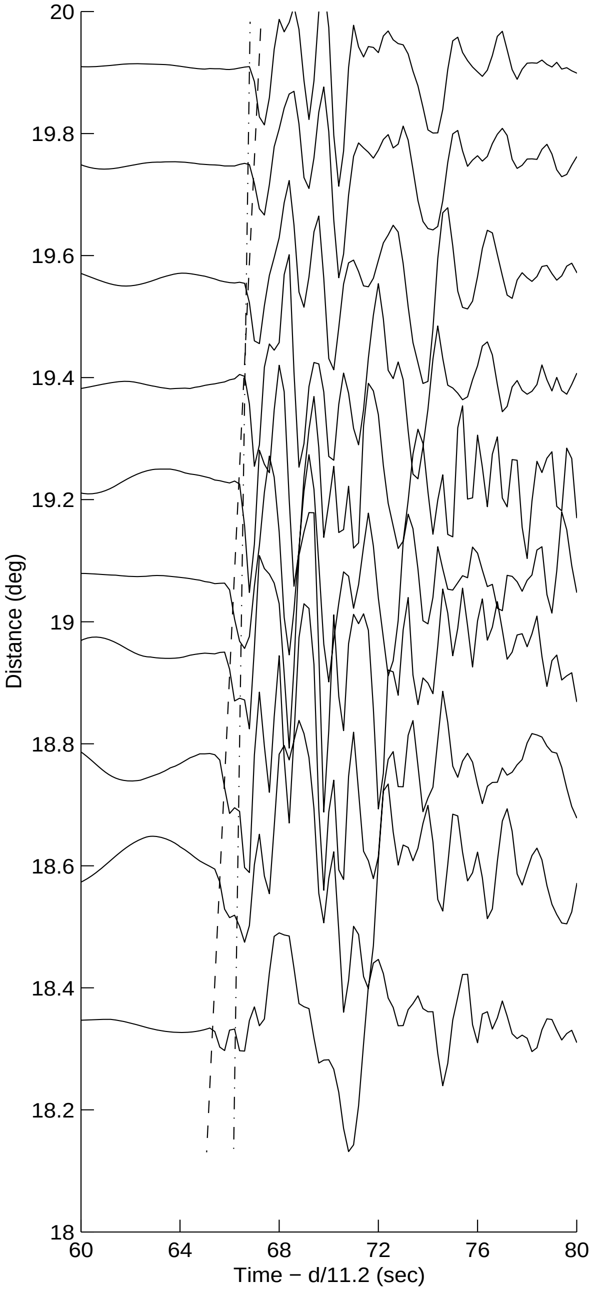

Figure 3.6 Vertical component data from 18º to 20º distance. The dash and dash-dot lines show two arrivals that merge with distance.

although the arrivals are more subtle than for the SH waves. Also it can be seen in Figure 3.3 (on the right) that the predicted travel times of branch CD are earlier than the data at stations between 18 and 21 degrees in distance but are in agreement or later beyond 21º distance. Branch CD represents waves that are turning within the transition according to the IASP91 model. These observations and interpretations reveal significant differences in velocity in the transition zone beneath eastern Mexico relative to the IASP91 reference model.

The seismic waveforms discussed above clearly show all the triplicated branch arrivals due to the upper mantle discontinuities for both P and S waves. It is clear that IASP91 does not match the relative timing of arrivals and thus the waveforms. IASP91 does match the first arrival times reasonably well although there is a clear discrepancy for the P waves at the shorter distances. Other global average models such as PREM and AK135 also do a poor job of fitting the data. The data shown in Figures 3.2 and 3.3 are most sensitive to seismic velocity within the transition zone. If the shallower mantle is slower or faster than IASP91 the result would be primarily a shift in travel time and the misfits in waveform would not be as large as seen. To determine the seismic P and S velocity structure of the transition zone beneath eastern Mexico we used a waveform inversion technique developed by Matzel and Grand (2004) to invert the data shown in Figures 3.2 and 3.3. The technique is discussed in the next section.

3.4 Waveform inversion method

The general nonlinear forward model for a seismic waveform synthetic can be written as

$$\underline{d} = f(\underline{m}, r_{inst}, r_{source}) \tag{3.1}$$

where $\underline{d}$ is the seismic synthetic vector, $\underline{m}$ is an earth model vector, and f is a nonlinear operator that maps the model space M into the data space D and r_{inst} and r_{source} are instrument response and source information (mechanism and time function) respectively. Our objective is to find a model $\underline{m}$ that best fits the seismic observations by minimizing the difference between synthetic and observed waveforms. Here we briefly describe the inversion method. To linearize the non-linear problem, we can write the relation:

$$\underline{d}(\underline{m}, r_{inst}, r_{source}) - \underline{d}_{obs} = f(\underline{m}, r_{inst}, r_{source}) - f(\underline{m}_0, r_{inst}, r_{source}) \tag{3.2}$$

where $\underline{d}(\underline{m}, r_{inst}, r_{source})$ is the updated synthetic waveform and $\underline{d}_{obs}$ is the observed waveform. The first order Taylor series approximation of the term $f(\underline{m}_0, r_{inst}, r_{source})$ becomes:

$$f(\underline{m}_0, r_{inst}, r_{source}) = f(\underline{m}\ \ , r_{inst}, r_{source}) + [\partial f / \partial \underline{m}](\underline{m}_0 - \underline{m}) \tag{3.3}$$

This gives a matrix formulation of the forward problem:

$$\Delta \underline{d} = [\partial f / \partial \underline{m}] \Delta \underline{m} = D \Delta \underline{m} \tag{3.4}$$

where $\Delta\underline{d} = \underline{d} - \underline{d}_{obs}$ is the difference between data and synthetics and $\Delta\underline{m} = \underline{m} - \underline{m}_0$ is the difference between the starting model and the real model of the Earth.

The term $D = [\,\partial f / \partial \underline{m}\,]$ is a matrix of differential seismograms which is a measurement of the sensitivity of the seismograms to the perturbations of $\underline{m}$ (the earth model) for fixed events and receivers. In our inversion the differential seismograms were numerically determined by calculating synthetic seismograms for a velocity model and a perturbed model:

$$\underline{d}(\underline{m} + \delta\underline{m}) = \underline{d}(\underline{m}) + D\delta\underline{m} \tag{3.5}$$

where $\delta\underline{m}$ is a small perturbation to a model $\underline{m}$. We used the reflectivity method (Fuchs and Muller, 1971) to generate the synthetics and the differential seismograms. An advantage of generating the differential seismograms numerically is that it is easy to substitute a different synthetic technique into our code. It is clear that the solution of equation (3.4) depends on the starting model due to the non-linear nature of the original problem.

In this study we solve equation (3.4) using the conjugate gradient algorithm originally applied to seismology by Mora (1988) and used in Matzel and Grand (2004). The conjugate gradient algorithm iteratively minimizes the misfit function (see Appendix C)

$$S(\underline{d}, \underline{m}) = 1/2[\Delta\underline{d}^T C_d^{-1} \Delta\underline{d} + \Delta\underline{m}^T C_m^{-1} \Delta\underline{m}] \tag{3.6}$$

where C_d and C_m are the covariance matrices for data and model spaces respectively (T indicates conjugate transpose). The algorithm for nonlinear least squares by the preconditioned conjugate gradient method is

$$\left\{\begin{array}{l}
\underline{d}_n = \underline{d}(\underline{m}_n) \\
\Delta\underline{d}_n = \underline{d}_n - \underline{d}_{obs}, \Delta\underline{m}_n = \underline{m}_n - \underline{m}_0 \\
\underline{g}_n = \partial S(\underline{d},\underline{m}) / \partial \underline{m} = D_n^T C_d^{-1} \Delta\underline{d}_n + C_m^{-1} \Delta\underline{m}_n \\
\underline{p}_n = C_m \underline{g}_n \\
\underline{c}_n = \underline{p}_n + \dfrac{\underline{p}_n^T(\underline{g}_n - \underline{g}_{n-1})}{\underline{p}_n^T \underline{g}_n} \underline{c}_{n-1}, \quad \underline{c}_1 = \underline{p}_1 \\
\eta_n = \dfrac{\underline{c}_n^T \underline{g}_n}{\underline{c}_n^T D_n^T C_d^{-1} D_n \underline{c}_n + \underline{c}_n^T C_m^{-1} \underline{c}_n} \\
\underline{m}_{n+1} = \underline{m}_n - \eta_n \underline{c}_n
\end{array}\right. \tag{3.7}$$

for n = 1, 2, 3, …, where $\underline{g}_n$ is gradient, D_n is a matrix of differential seismograms, $\underline{p}_n$ is preconditioning, $\underline{c}_n$ is conjugate direction, η_n is step length, and $\underline{m}_{n+1}$ is updated model. The conjugate gradient algorithm converges rapidly for upper mantle waveform problems (Matzel, 2002) and it iteratively minimizes the difference between data and synthetics in a least squares sense to find the local best fitting model. An intermediate solution is obtained by using the gradient vector $\partial S(\underline{d},\underline{m}) / \partial \underline{m}$ to calculate the conjugate vector and the step length and subsequently determines the model update. Seismic synthetics are calculated by the reflectivity method (Fuchs and Muller, 1971) and the earthquake mechanism parameters are taken from Harvard's seismological center (CMT solution). The source functions were derived by forward modeling the largest distance seismograms in our data.

3.5 Inversion results and analysis

A difficulty with a linearized waveform inversion such as we used is that if the starting model predicts synthetics that are more than ½ cycle different than the data the inversion can converge to a wrong model predicting synthetics one cycle off from the data. In this study the point source model is used in seismic modeling due to the epicentral distance and the magnitude characteristics of the event. The shear wave data have relatively stronger long period signal than the P waves. For this reason, we initially perform the waveform inversion on the shear wave data. A second difficulty with a linearized inversion is that many local minima can exist in model space. The conjugate gradient method will find the closest local minima and thus inversion results do depend on the starting model.

3.5.1 Shear velocity model

We attempt inversions with a range of different starting models. We set up three different starting models of shear wave velocity with different size jumps at the 410 km and 660 km discontinuities and varying gradients within the transition zone (Figure 3.7). We hold the phase transition thickness to be 20 km across both discontinuities (Melbourne and Helmberger, 1998) although turning wave data are

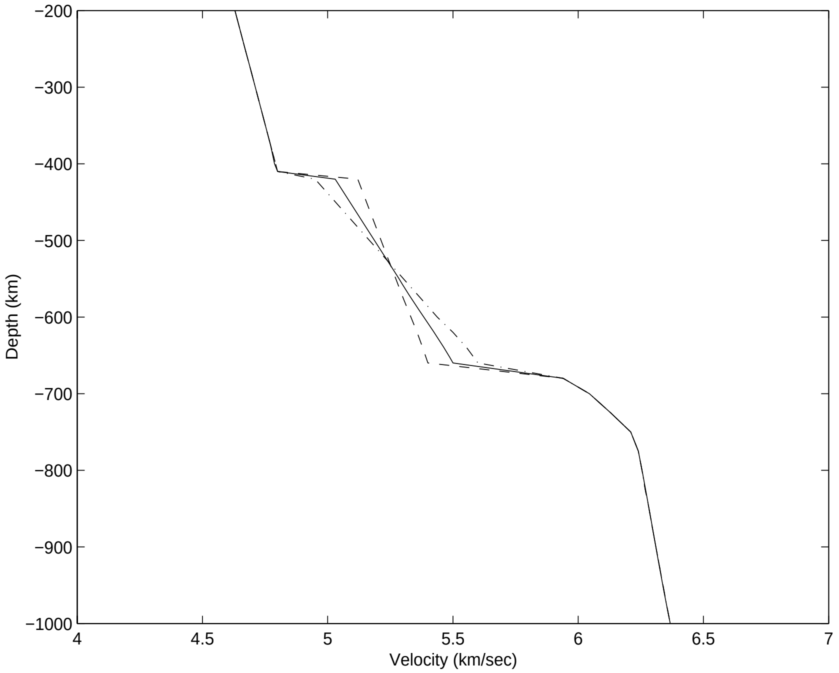

Figure 3.7 Three shear velocity starting models with different jump sizes at the 410 km and 660 km discontinuities as well as changing gradient within the transition zone. The dash-dot line presents the model with the highest gradient, the dash line presents the model with the lowest gradient, and the solid line presents the model with a medium gradient.

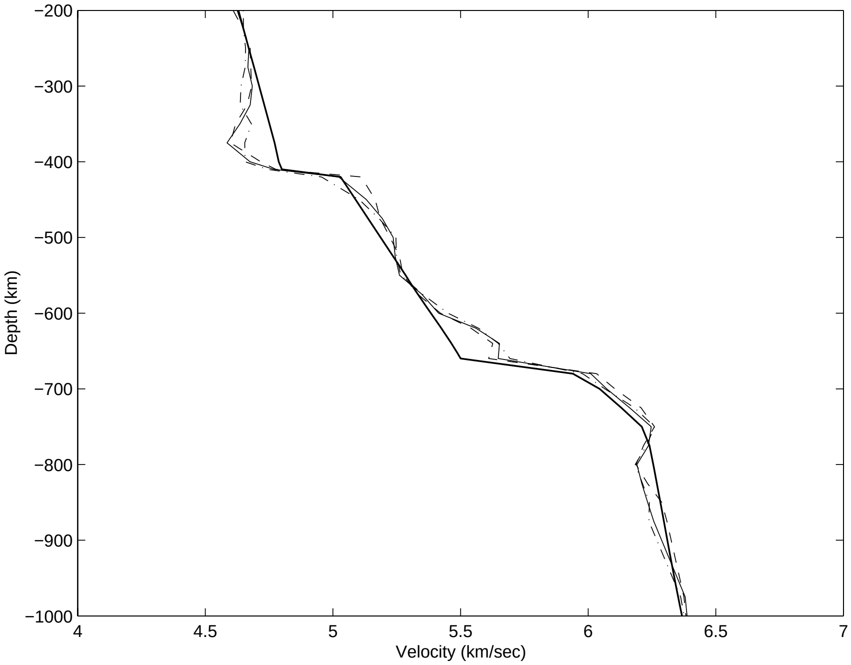

Figure 3.8 Three final velocity models found by the inversion from the starting models shown on Figure 3.7. The dash-dot line presents the final model with the highest starting gradient, the dash line presents the final model with the lowest starting gradient, and the solid line presents the model with a medium gradient. The thick solid line shows the medium gradient starting model (for reference).

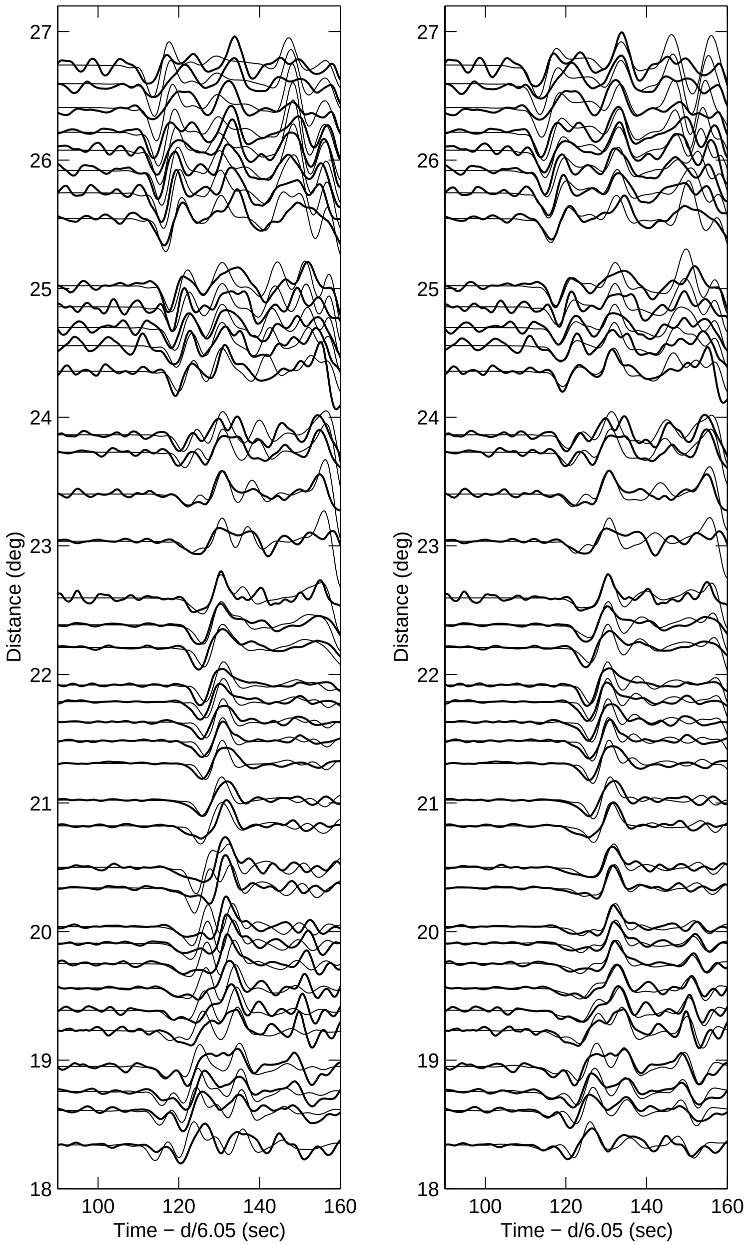

Figure 3.9 Comparison between data and synthetics (a) for the starting and final models with the high gradient. The comparison for the starting model is on the left, and the final model's comparison is shown on the right. The thick solid lines stand for observations, and the thin solid lines stand for synthetics.

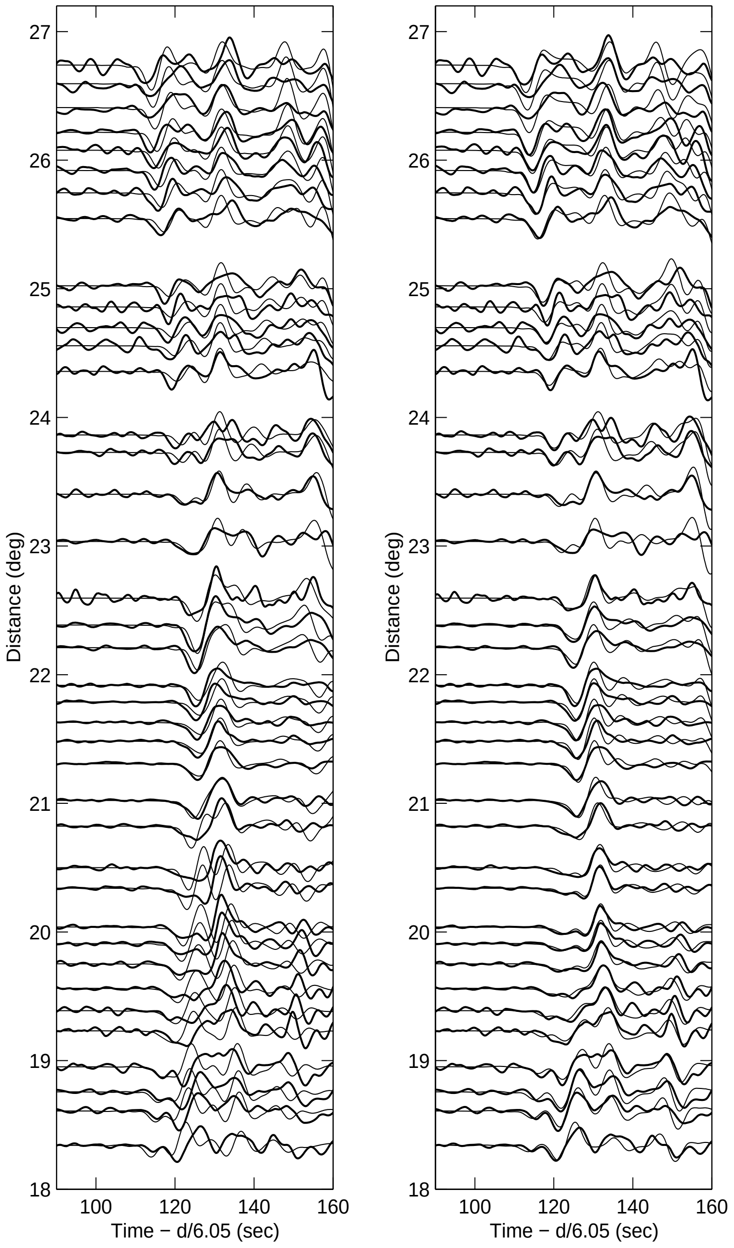

Figure 3.10 Comparison between data and synthetics (b) for the starting and final models with the medium gradient. The comparison for the starting model is on the left, and the final model’s comparison is shown on the right. The thick solid lines stand for observations, and the thin solid lines stand for synthetics.

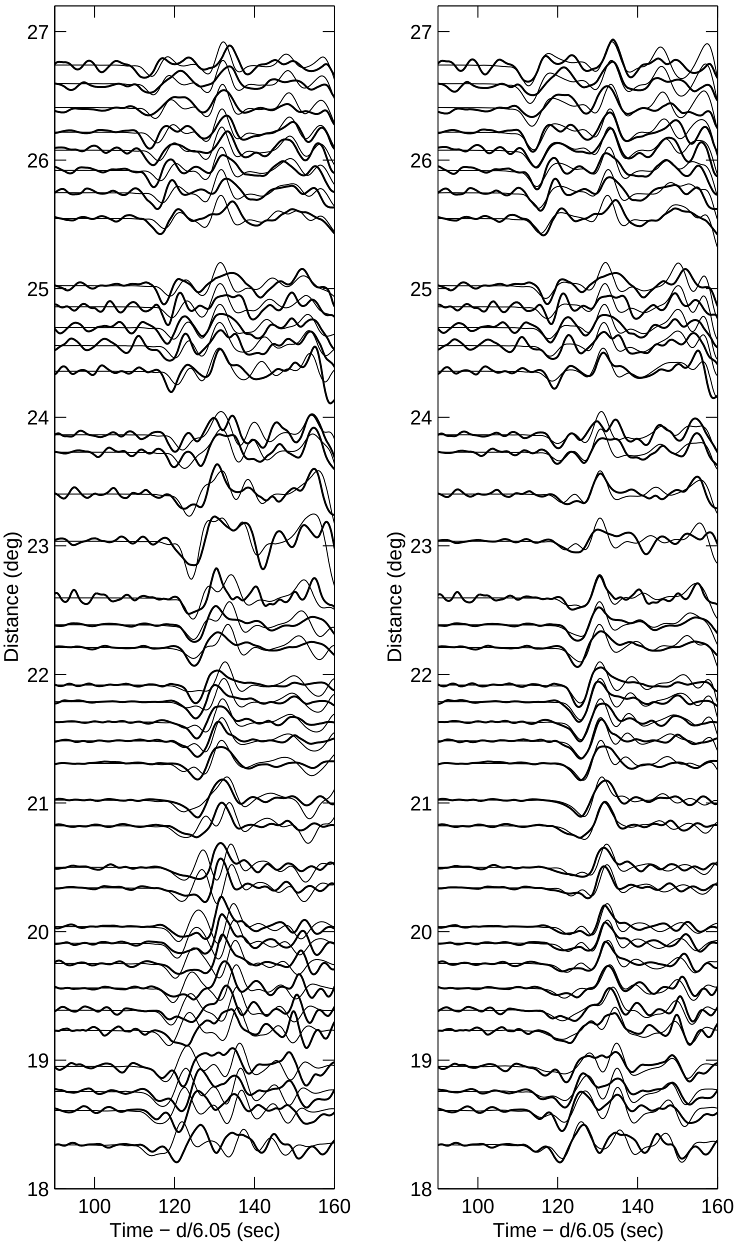

Figure 3.11 Comparison between data and synthetics (c) for the starting and final models with the low gradient. The comparison for the starting model is on the left, and the final model's comparison is shown on the right. The thick solid lines stand for observations, and the thin solid lines stand for synthetics.

not strongly sensitive to discontinuity sharpness. The model with medium gradient in the transition zone is taken from Grand and Helmberger (1984). The inversion results using the starting models in Figure 3.7 are shown in Figure 3.8. It can be seen that the three different starting models produce roughly the same final models after inversion though details over 50 km depth intervals vary a little. All three models show a low velocity zone atop the 410 km discontinuity and an unexpected high velocity gradient beginning at a depth of about 600 km. Figures 3.9 – 3.11 show the comparison between the observations and synthetics for different starting models and the corresponding final models. It is clear that the inversion finds a fit to the data that is much better than any of the starting models provide. The different final models, however, produce fairly similar fits to the data. It can be seen from the comparisons between synthetics produced by the three starting models and observations that there are some common features in the synthetics. For example, the synthetic phases at stations between 18.5° and 21° in distance arrive earlier (faster) than the observations on the CD branch but slower than the observations on EF branch. In addition, their amplitudes are larger than the data. There are also some different features obtained with different starting models. In particular, the phases on the EF branch for the medium and low gradient models are slower than the data whereas this is not the case for the high gradient model. Also, the phases on the CD branch for the high gradient model are fast and their amplitude is smaller than the observations at stations between

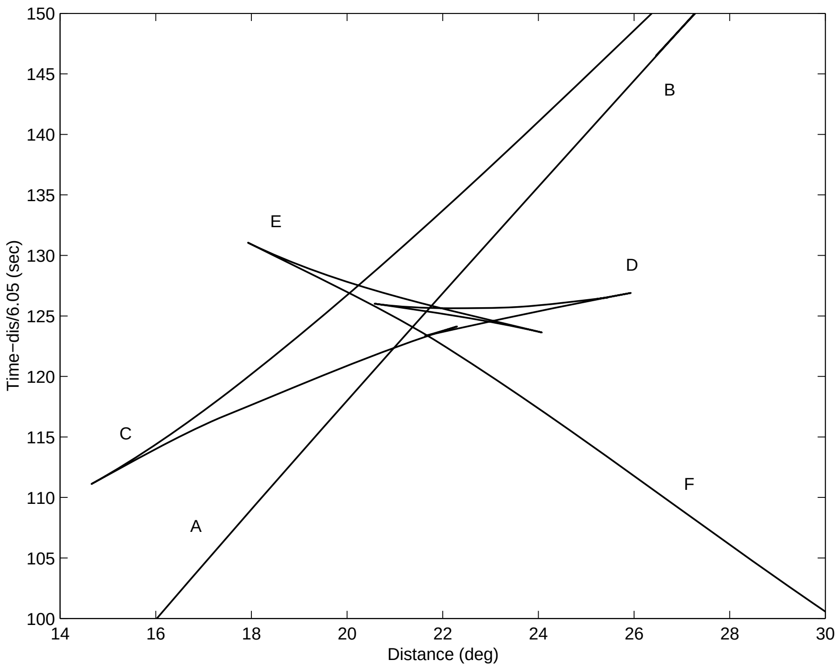

Figure 3.12 Travel time curve predicted by the final model with the medium gradient. It shows a small triplication resulting from a small velocity jump at 600 km depth.

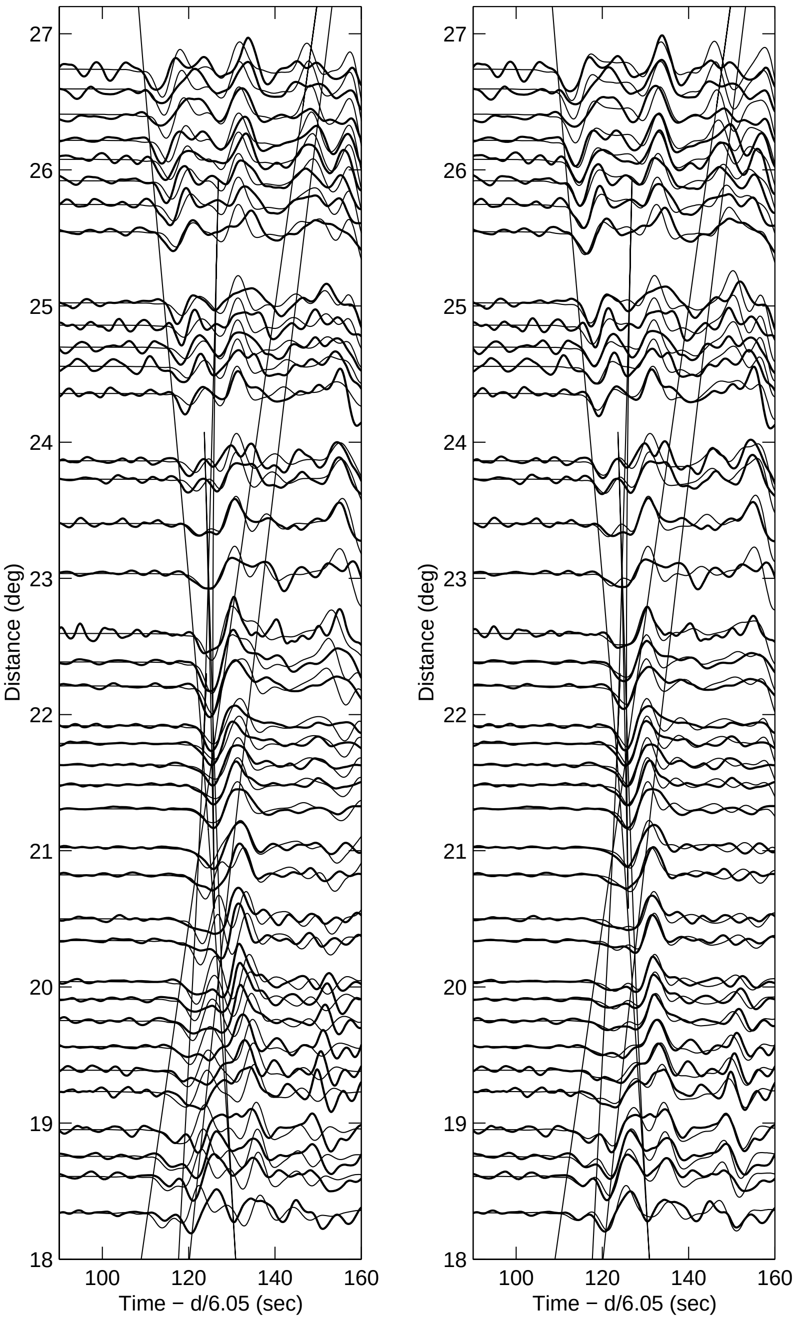

Figure 3.13 Comparison between data and synthetics with the travel time curve predicted by the final model with the medium gradient. It shows a small triplication resulting from a small jump at 600 km depth.

25.5º and 27º in distance. By comparing the synthetics produced by the starting models and their respective final models, it is clear that the low velocity zone atop 410 km discontinuity is delaying the CD branch and decreasing the amplitude of the CD branch arrivals between 18.5º and 21º in distance. However, it is hard to visually identify which features are produced by the small jump at depth of 600 km. From contrast between the seismograms and the travel time curve predicted by the final model (see Figures 3.12 and 3.13) a small jump near 600 km depth seems to be compensating for the amplitude decrease of the phases at stations between 21º and 24º in distance and also compensating for the time delay of the EF branch. Although the time window for the shear waveform inversion is constrained to be from about 110 second to 145 second, the synthetic seismograms produced by the final model fit the observations of sS phases (from 145 second to 160 second) for the closer stations (18.5º – 20.5º) better than produced by the starting models (see Figures 3.9 – 3.11) .

The following figures (Figures 3.14 – 3.23) show the comparisons of the intermediate results of the inverted models and their synthetics with the starting model and data respectively and the rate of convergence of the inversion for shear velocity model with increasing number of iterations. Figure 3.14 through Figure 3.23 show the comparison between the starting model and intermediate inverted models and the data and synthetics for the 3rd, 6th, 9th, 12th, and 15th (final)

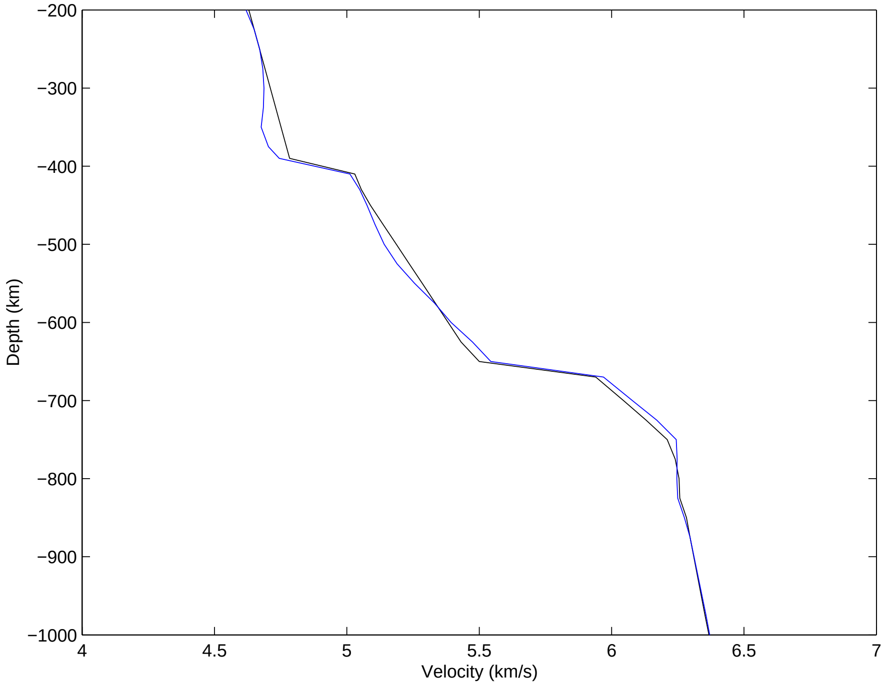

Figure 3.14 Comparison between the starting model (black line) and an intermediate 3rd iteration model (blue lines).

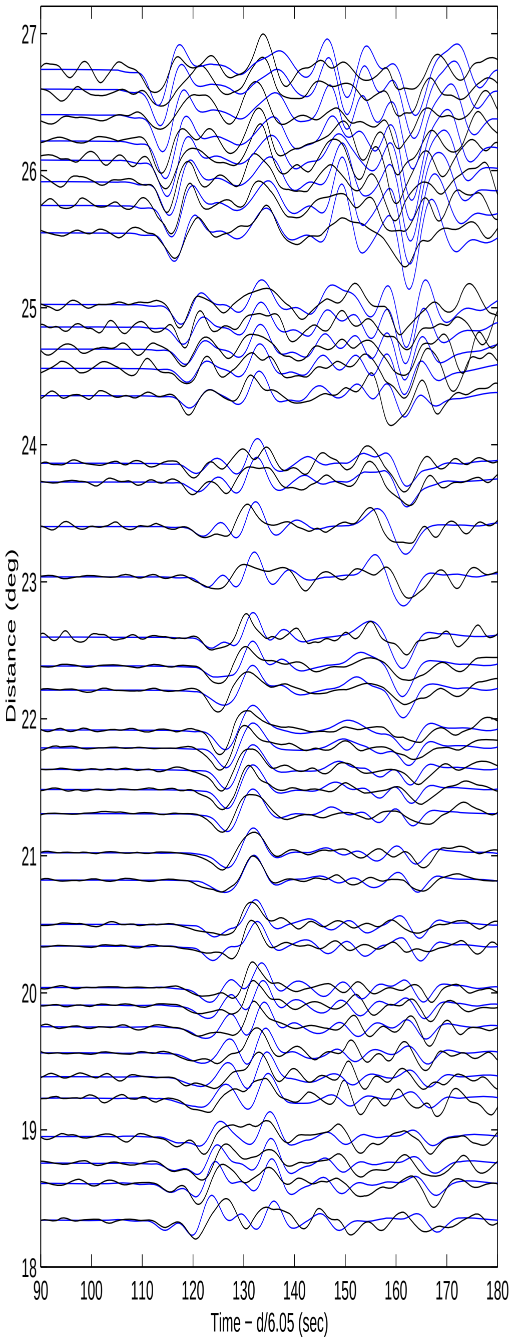

Figure 3.15 Comparison between observed data (black lines) and synthetics (blue lines) for a model with 3 iterations.

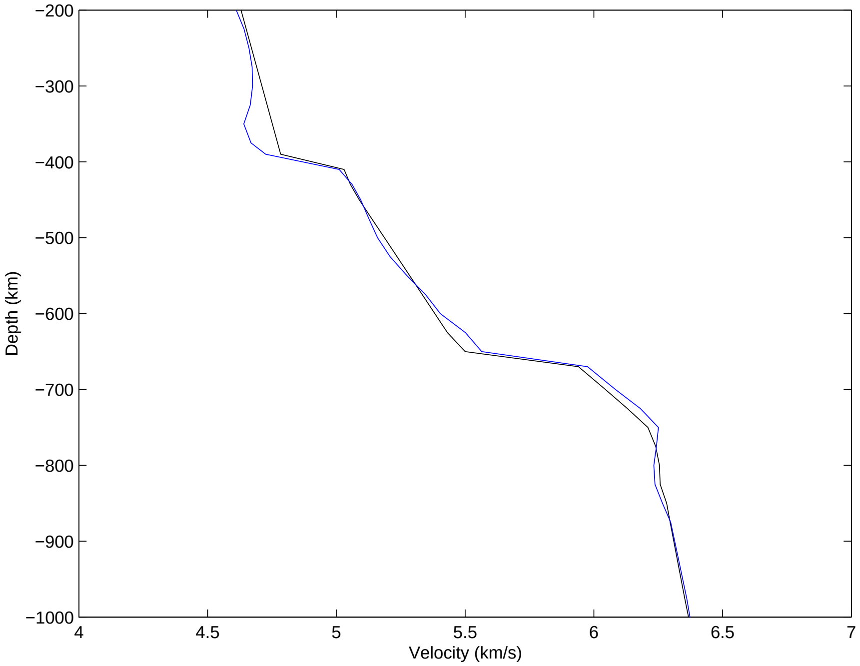

Figure 3.16 Comparison between the starting model (black line) and an intermediate 6th iteration model (blue line).

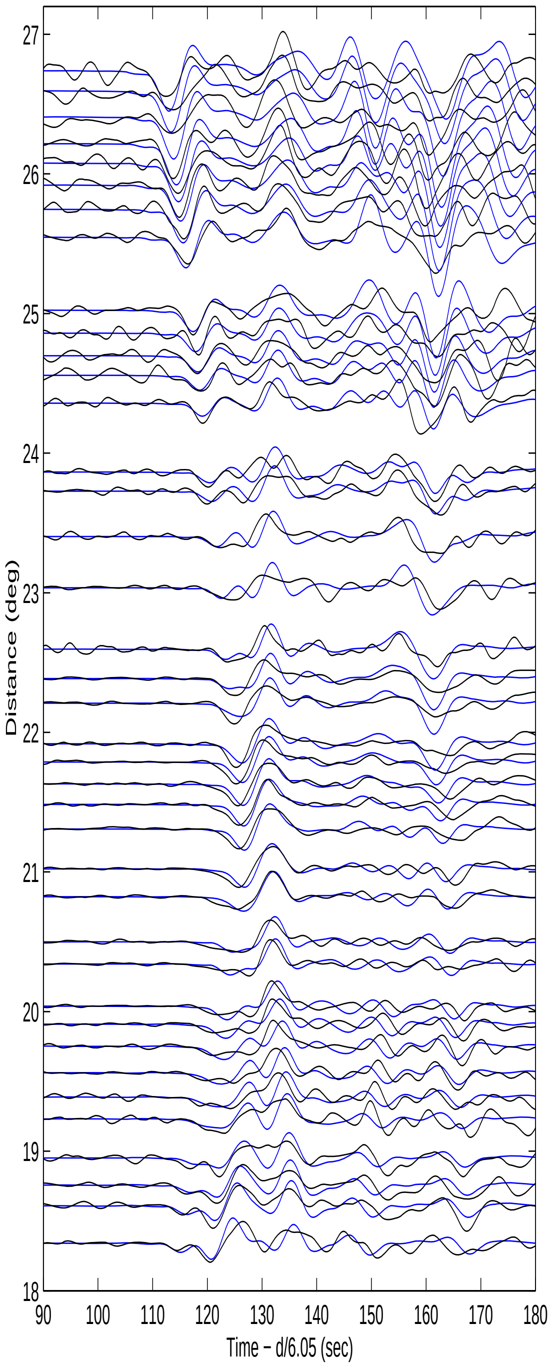

Figure 3.17 Comparison between the data (black lines) and synthetics (blue lines) for the 6th iterative model.

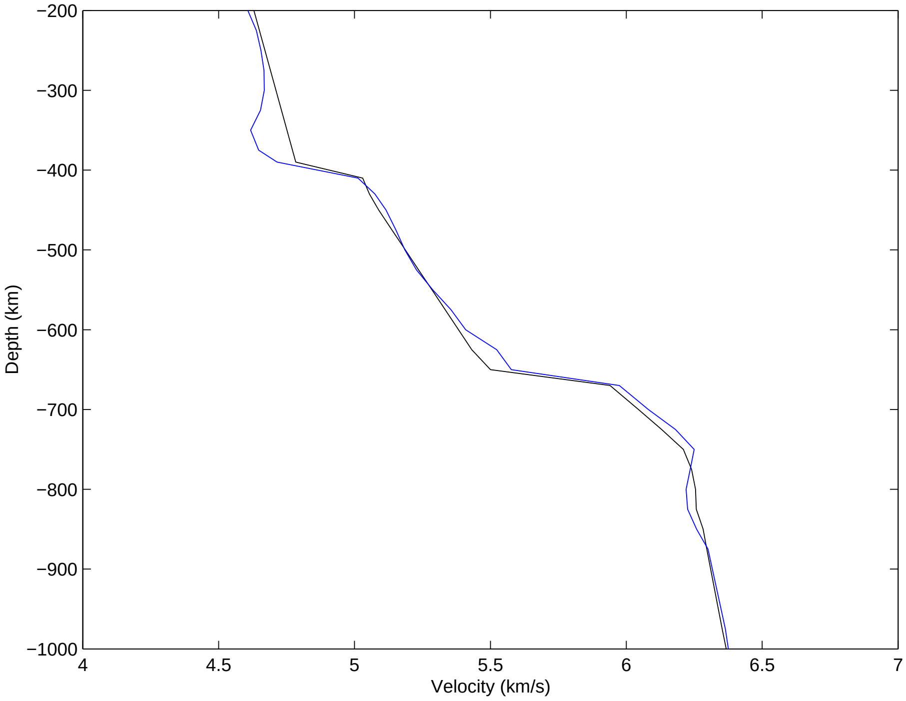

Figure 3.18 Comparison between the starting model (black line) and an intermediate 9th iteration model (blue line).

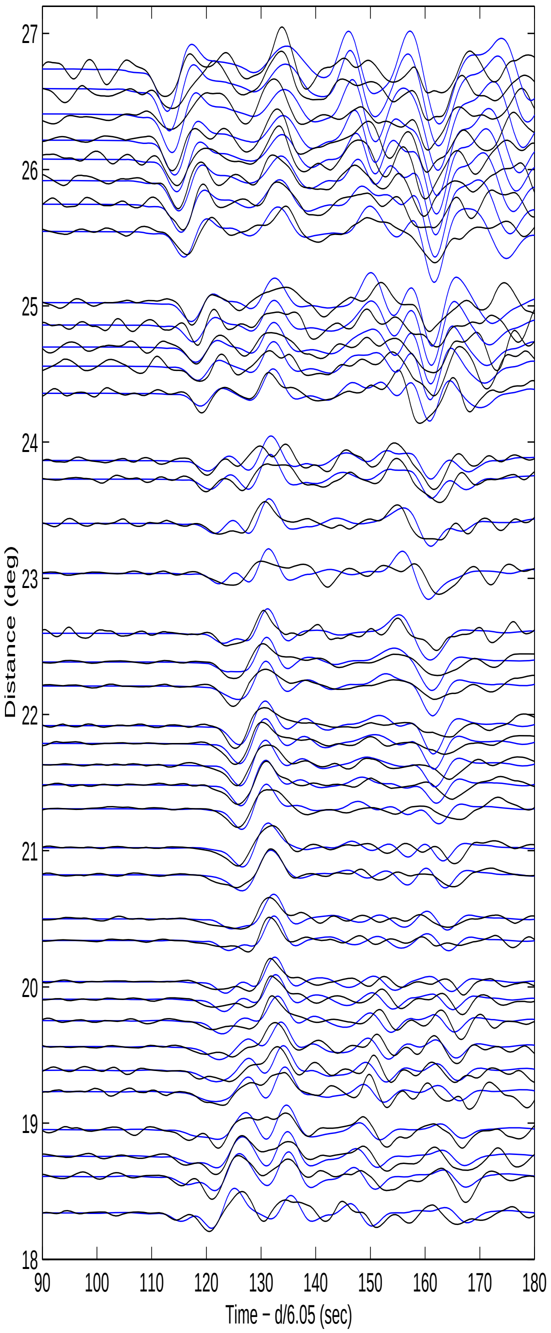

Figure 3.19 Comparison between the data (black lines) and synthetics (blue lines) for a model with 9th iterations.

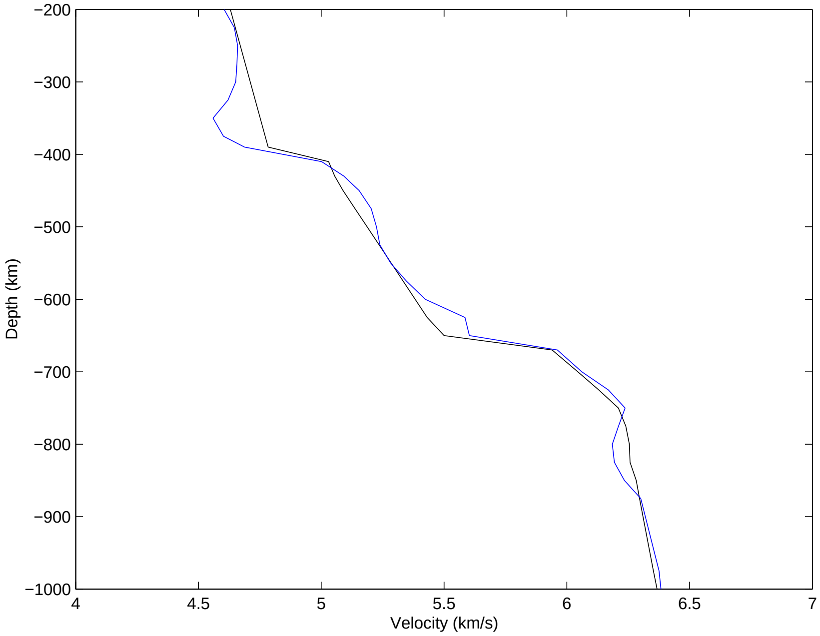

Figure 3.20 Comparison between a starting model and an intermediate model. The black line is a starting model and the blue line presents the model in the 12th iteration.

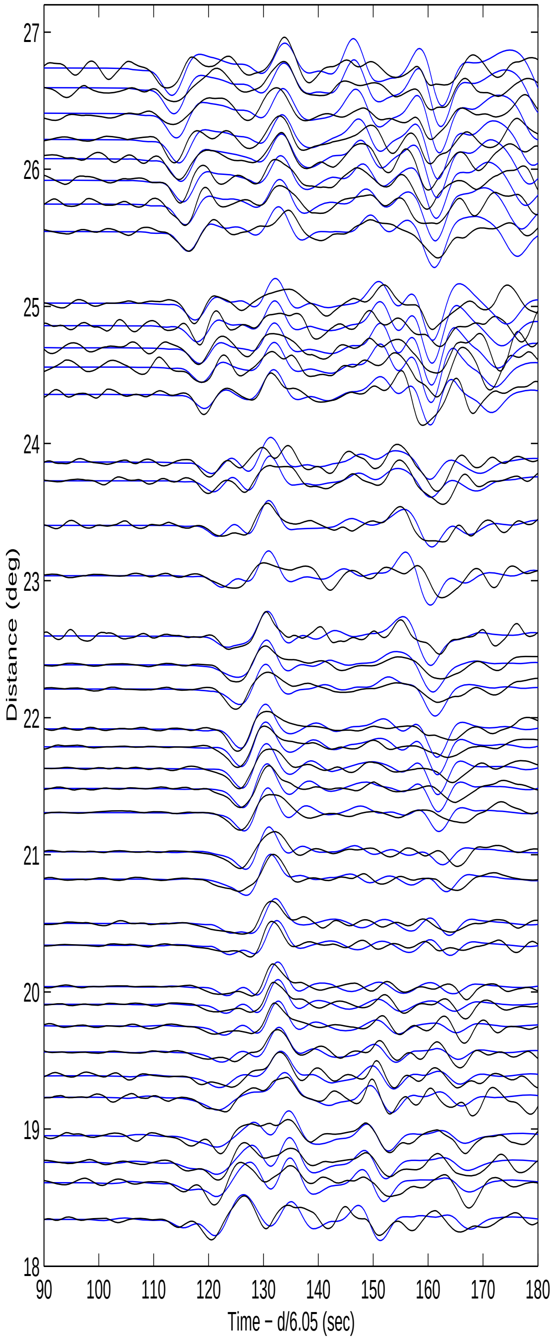

Figure 3.21 Comparison between the data (black lines) and synthetics (blue lines) for the 12th iterative model.

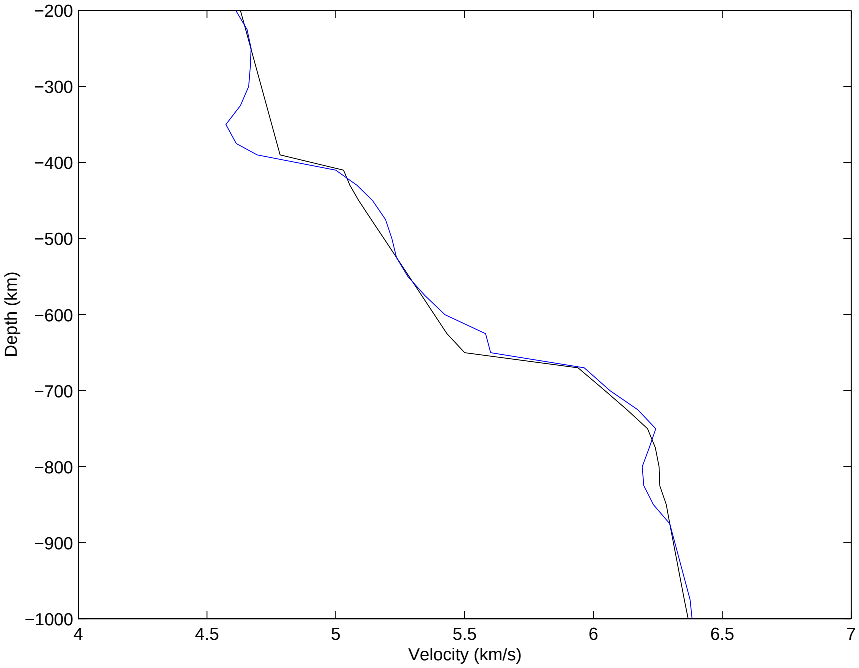

Figure 3.22 Comparison between a starting model and an intermediate model. The black line is a starting model, and the blue line presents model in the 15th iteration.

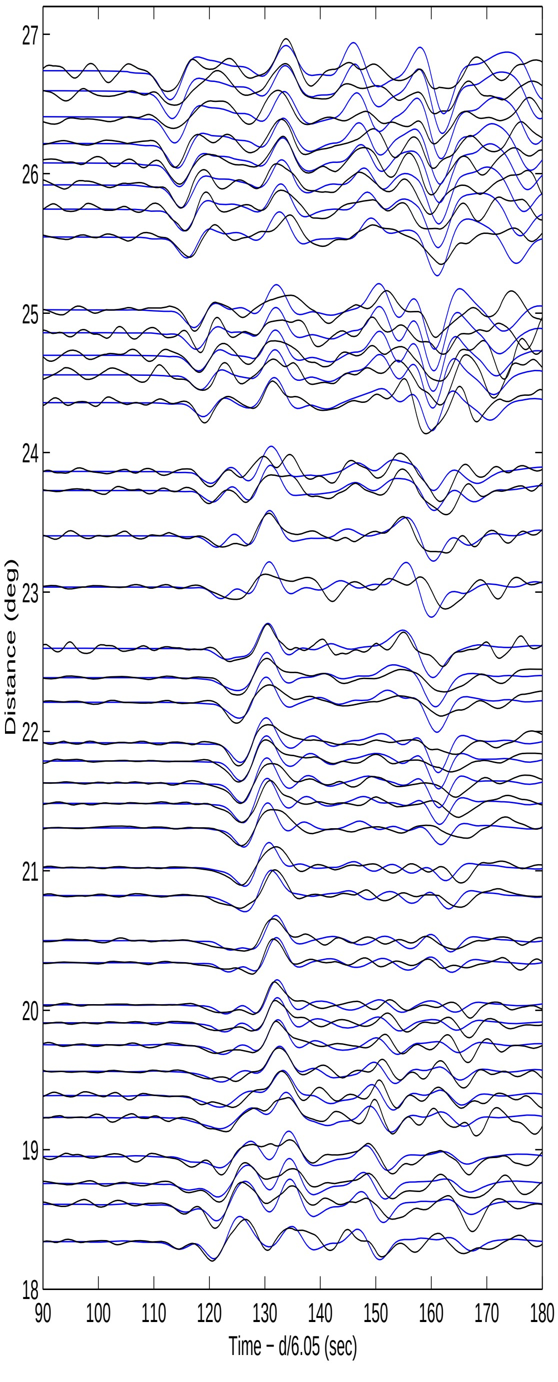

Figure 3.23 Comparison between the data (black lines) and synthetics (blue lines) for the 15th iterative model.

iteration models respectively. It is seen from these figures that the rate of convergence of the waveform inversion is very fast. The features of the low velocity zone above the 410 km discontinuity and the small jump at 600 km depth become progressively clear with increasing iterations as differences between data and synthetics rapidly decreases.

We have also tested the sensitivity of the inversion results to the depths of the discontinuities in the starting model. Figure 3.24 shows the results of the inversion for starting models that have jumps in velocity at 400, 410, and 420 km depth respectively. The fits to the data are similar for the three models and indeed turning wave data are not very sensitive to the exact depth of the discontinuity. The three models all have a low velocity zone above the 410 km discontinuity and a high gradient above the 660 km discontinuity. Table 3.2 shows the final misfit values for inversions using different depths for the discontinuities with a broader range than shown in Figure 3.23. Note, discontinuity depths near 400 and 670 km depth provide better fits than using models with significantly different depth discontinuities consistent with the global average of their depths (Flanagan and Shearer, 1998).

3.5.2 Compressional velocity model

The compressional wave seismograms have weak long period signal relative to noise level due to the source radiation characteristics of this event. At

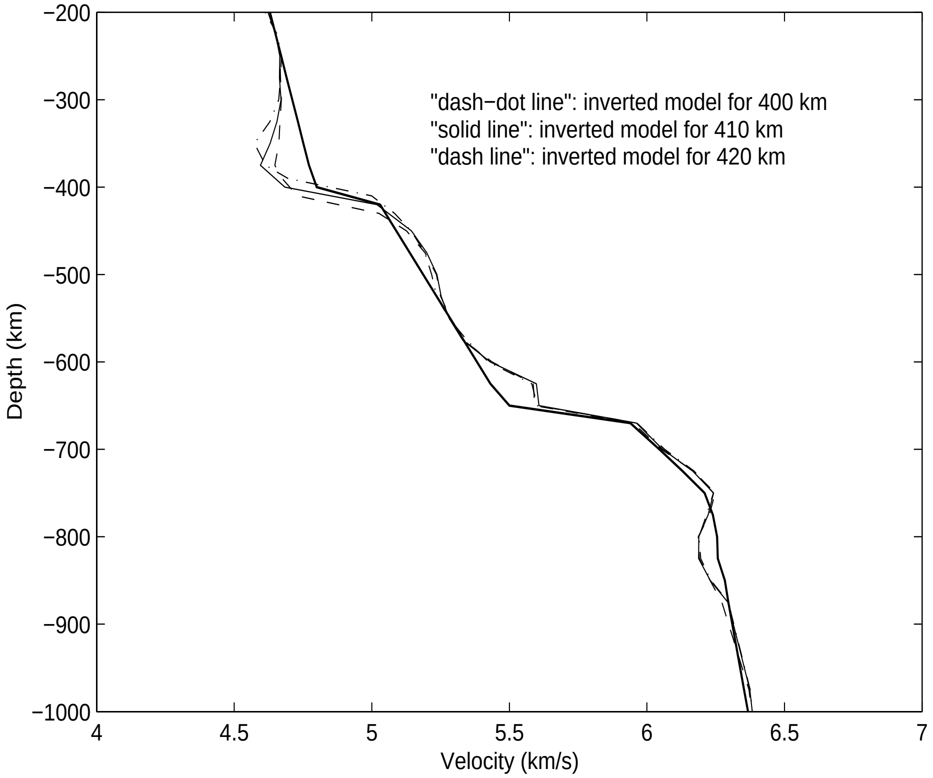

Figure 3.24 Comparison between three shear velocity models. Three shear velocity models produced by the inversion for starting depths of the 410 km discontinuity at 400, 410, and 420 km respectively. The thick solid line is the starting model with the 410 discontinuity at 410 km.

frequencies near 1 Hz, however, the amplitude is well above noise level so we chose to invert the P wave data with a higher passband (up to 1.5 Hz) than the S waves. Although there may be other earthquakes with stronger P waves the advantage to modeling both P and S for the same earthquake is that origin time errors, earthquake location errors, and the volume of mantle sampled by the two types of waves are identical so that the P and S models can be compared directly. In this case, the high frequency compressional seismograms require more detailed information on the source processes than the S wave data. When we construct the compressional wave synthetics for this data set, we have to find a model that describes the seismic structure the waves passed through as well as more detailed information about the source(s). In addition, the dependence of the solution on the starting model is more substantial with increased frequency content making the compressional waveform inversion more complex. At large distances (larger than 26°) the seismograms in Figure 3.3 essentially represent the P wave source(s). Thus we modeled the waveforms at those distances to determine the source function for the P waveform inversion. Also, at the high frequencies present in the P data we were required to forward model the data until the timing was almost correct in order for the inversion to converge properly.

The initial starting model used for the compressional waveform inversion was the S25 model for the Canadian shield (Lefevere and Helmberger, 1989). The P data also showed an extra triplication at close distances (Figure 3.6). This extra

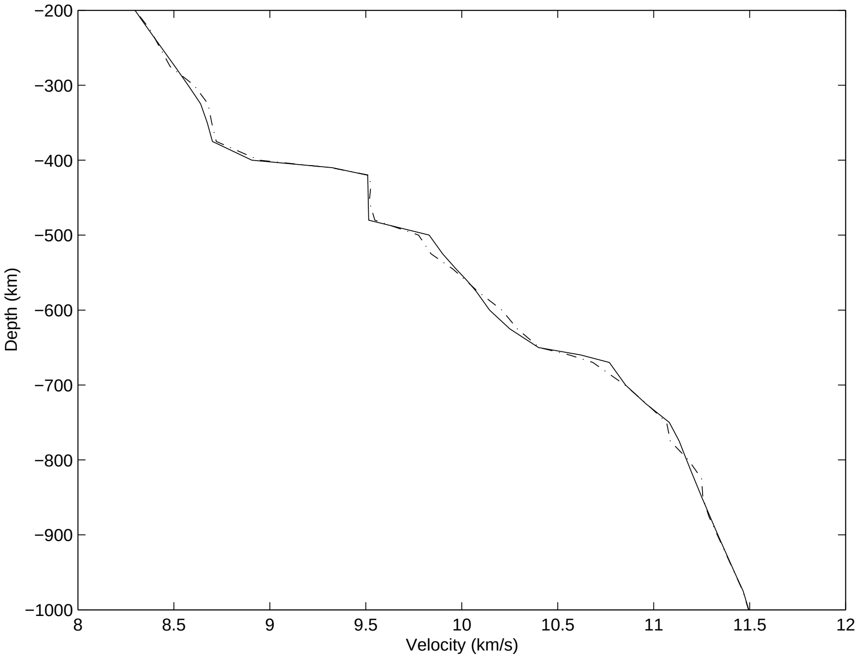

Figure 3.25 Starting and final models for inversion of the P data. The solid line is the starting model.

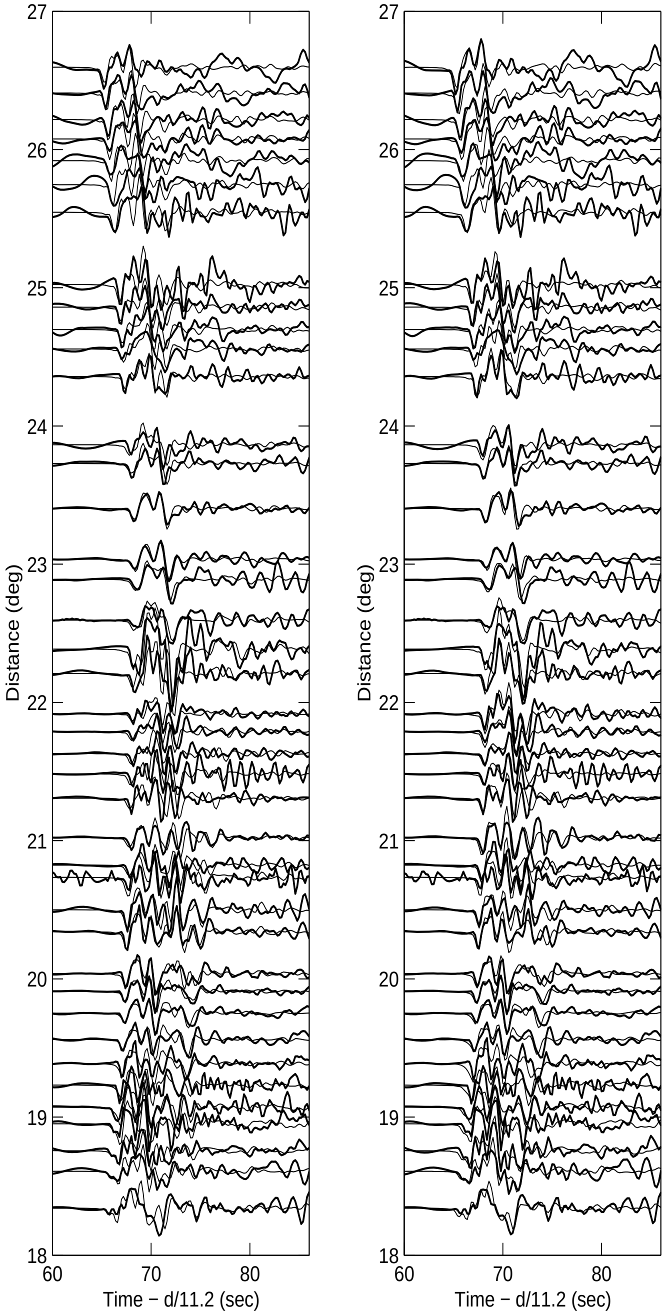

Figure 3.26 Comparison of the P wave data and synthetics. On the left the synthetics were computed using the starting model, and on the right the synthetics were computed using the inverted model. The heavy black lines show the data.

triplication required a discontinuity within the transition zone to model. We found by forward modeling a model that mimicked the features found in the shear wave model, except for the addition of a small jump in velocity near 490 km depth, which also matched the traveltimes of the P data. We used that model as the starting model in our inversion of the P data. Figure 3.25 shows the results of the waveform inversion for the compressional wave observations with model comparisons (starting and final) and Figure 3.26 shows the observed and synthetic waveform comparisons. Two main discontinuities at 410 km and 660 km and a small jump at depth of 490 km can be observed in the upper mantle. The small jump at 490 km in our model accounts for the two low-amplitude phases that merge together with increasing distance (observed from 18.5º to 19.5º, see Figure 3.6). From Figure 3.25 it is evident that the low velocity zone atop the 410 km discontinuity in the compressional model is not as significant as the feature observed in the shear model. Also, the S inversion results showed no discontinuity near 490 km depth.

To make the P and S models more compatible in major features we ran an inversion of the S wave data including a small jump in velocity at 490 km depth in the starting model. The results of inversion are shown in Figures 3.27 and 3.28. It can be seen in Figure 3.27 that the inversion of the S data tends to diminish the size of any jump in velocity near 490 km depth but does not eliminate the jump.

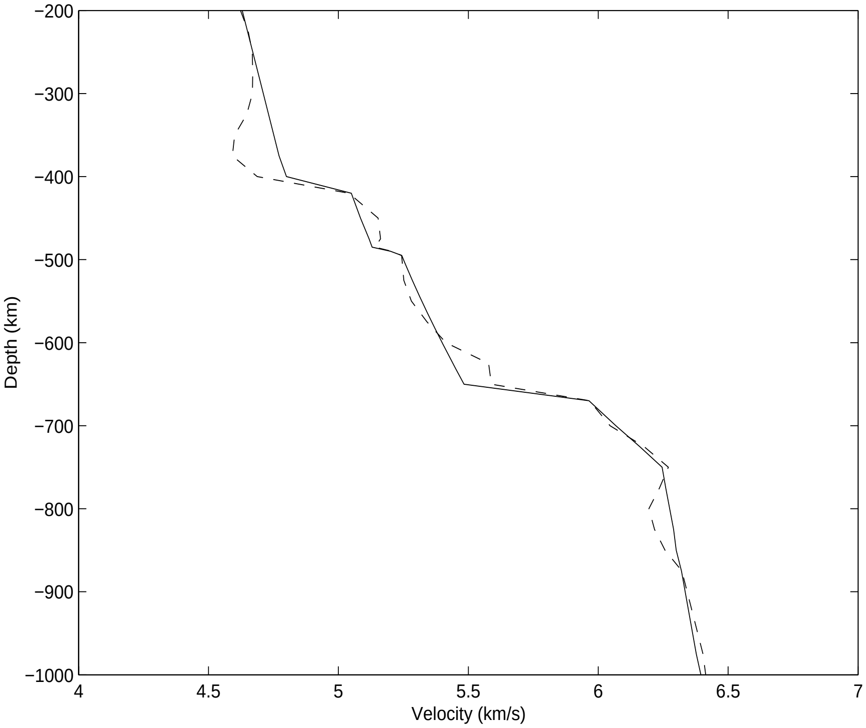

Figure 3.27 Results of the inversion of the shear wave data when a small discontinuity was added at 490 km depth in the starting model. Solid line is the starting model.

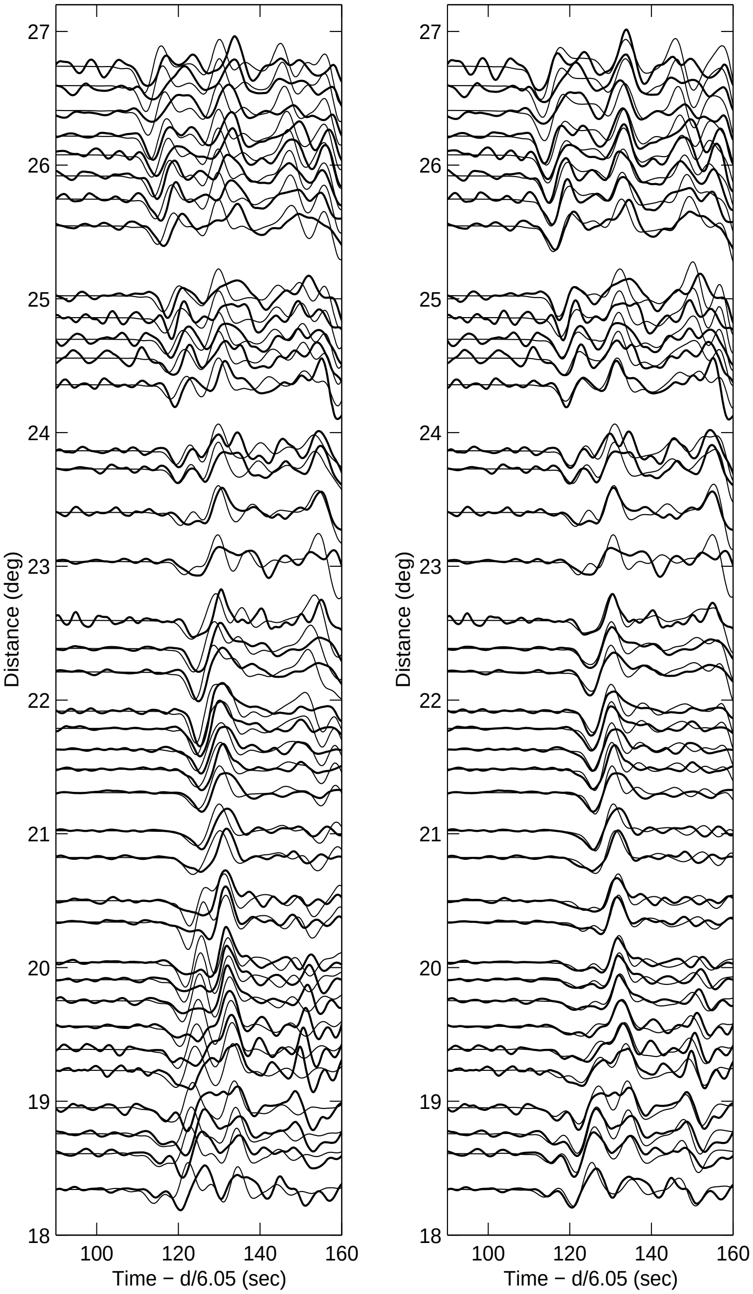

Figure 3.28 Comparison of data and synthetics using the starting model in Figure 3.27 (on the left) and using the inverted model in Figure 3.27 (on the right). The heavy black lines show the data.

The fit of the shear wave data by the model shown in Figure 3.28 is essentially as good as the fits to the data in Figures 3.9 – 3.11.

3.5.3 Uncertainty

It is well known that it is difficult to accurately determine the origin time of an earthquake. The effect of this uncertainty on the seismic modeling is a shifting in time of whole seismograms by several seconds faster or slower. We test the sensitivity of the inversions to errors in origin time of the source. Such errors would have a similar effect to errors in location. Figures 3.29 – 3.31 show the results of inversion for S wave data if the origin time i.e. the data is shifted 3 sec faster or 3 sec slower relative to the results shown above. Most of the changes due to a static time shift occur at very shallow depth. There is some change in velocity in the transition zone but they are small baseline shifts that do not change the size of discontinuities in the inversion nor the gradients. Note that the synthetic to data fits are as good as those shown in Figures 3.9 – 3.11. For the P wave data set the inversions are conducted with different starting models. Figures 3.32 – 3.34 show comparison between the inverted models and the starting model and comparison between data and synthetics for the P wave case respectively. It is seen in Figure 3.31 that the main features on the inverted compressional models do not change significantly.

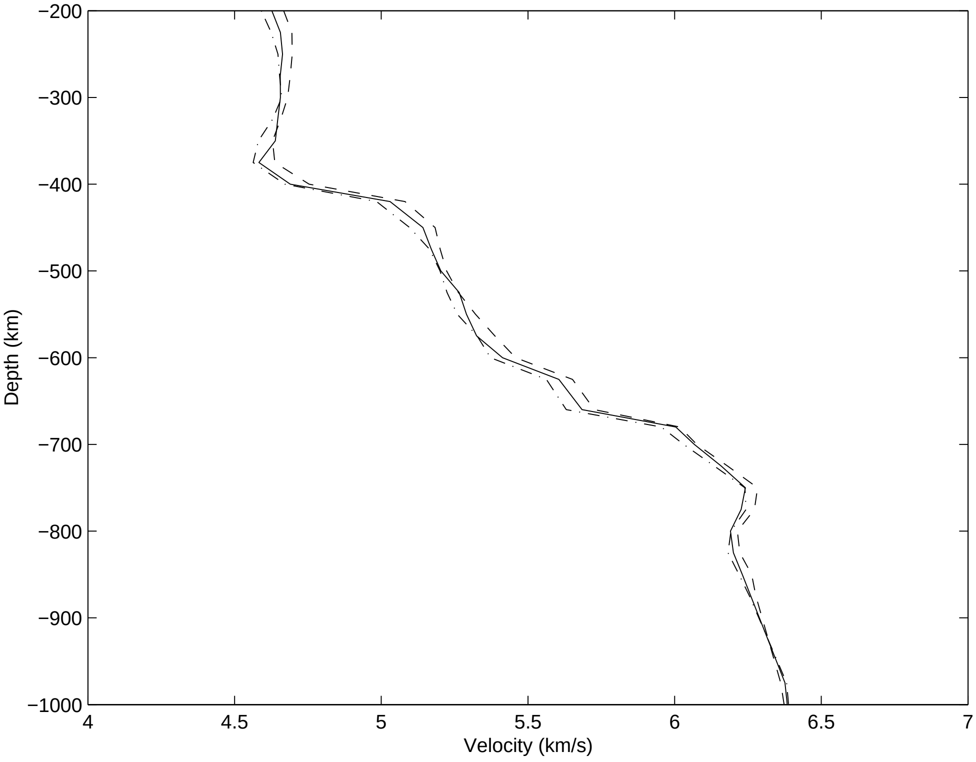

Figure 3.29 Comparison of the three final models. The results of three inversions of the shear wave data with a +3 sec shift in origin time, a 0 shift in origin time, and a -3 sec shift in origin time. The starting model in these inversions is the same as the intermediate gradient starting model in Figure 3.7.

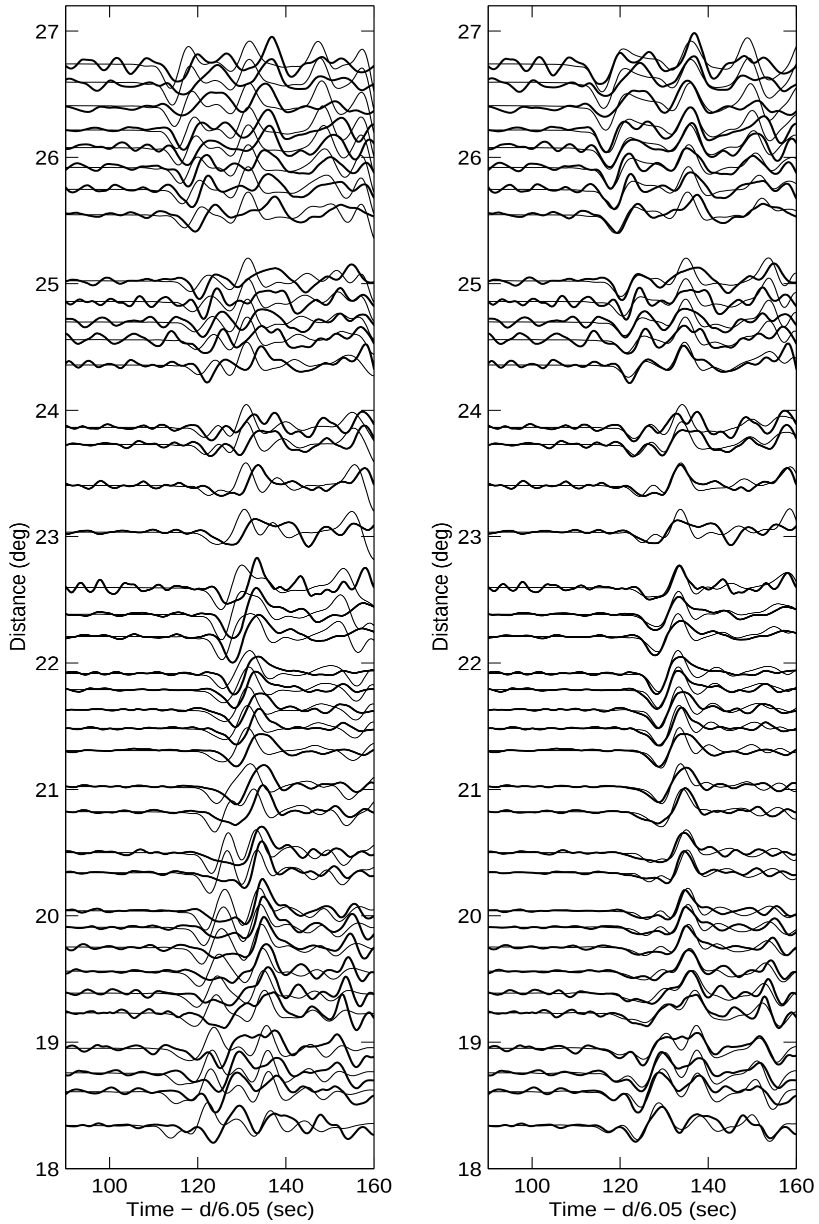

Figure 3.30 Comparison between data and synthetics for the starting model and the final model with a 3 second delay. The thick solid lines stand for observations, and the thin solid lines stand for synthetics. The comparison for the sarting model is shown on the left, and the final model's comparison is on the right.

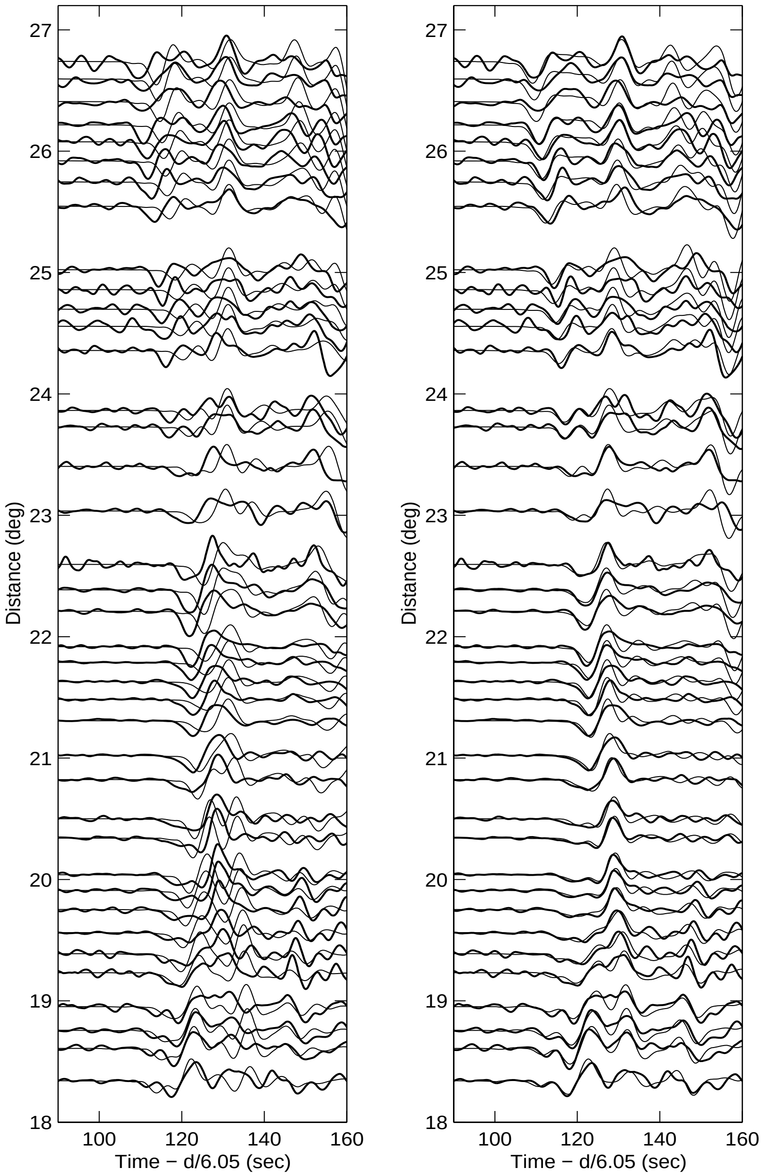

Figure 3.31 Comparison between data and synthetics for the starting model and the final model with a 3 second advance. The thick solid lines stand for observations, and the thin solid lines stand for synthetics. The comparison for the sarting model is shown on the left. On the right is the comparison for the final model.

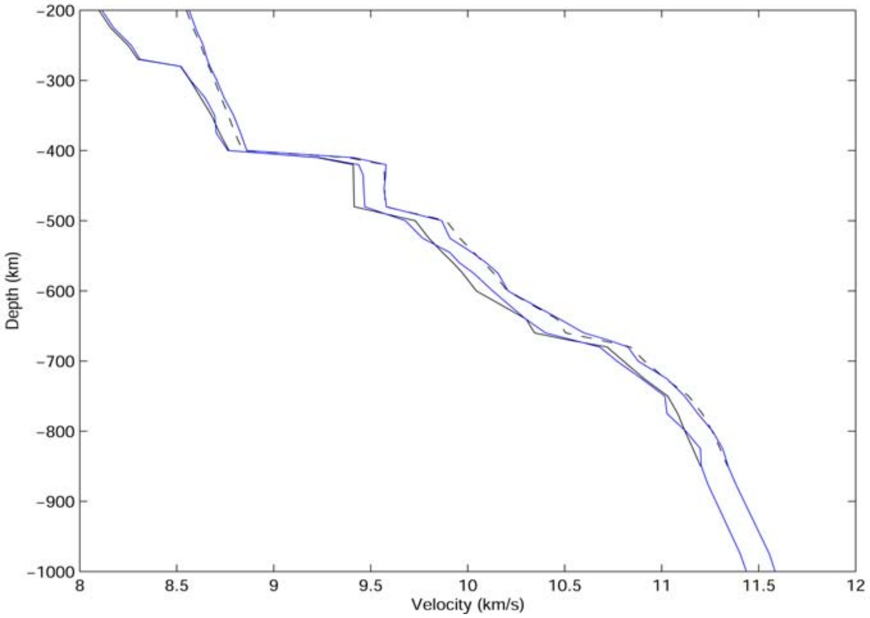

Figure 3.32 Comparison between the starting and final models for the compressional velocity models with a 3 second advance and a 3 second delay. The black and blue solid lines stand for the starting and final models respectively for the 3 second. The black and blue dash lines stand for the starting and final models respectively for 3 second advance.

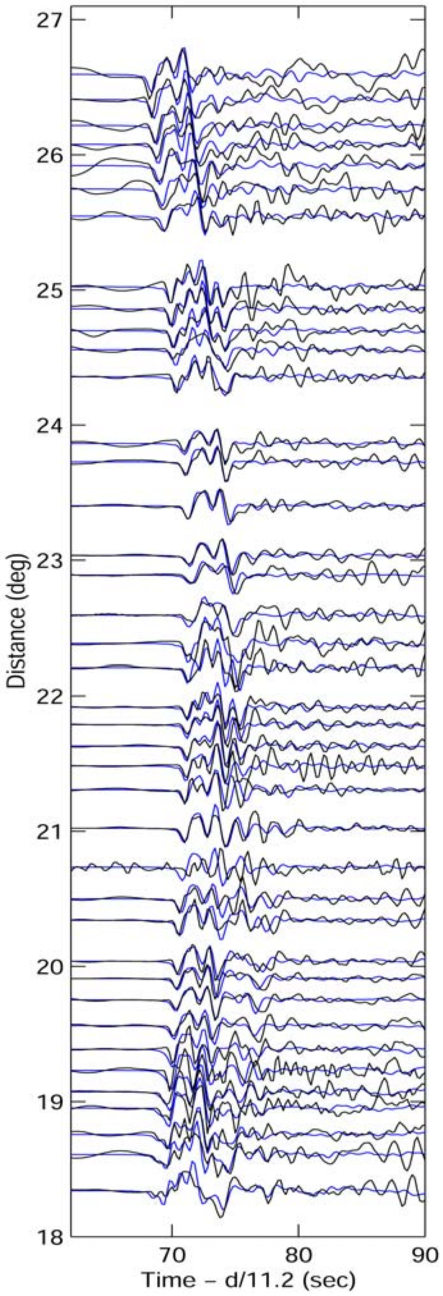

Figure 3.33 Comparison between data and synthetics for the final model (in Figure 3.32) with a 3 second delay. The black lines stand for the observations, and the blue lines stand for the synthetics.

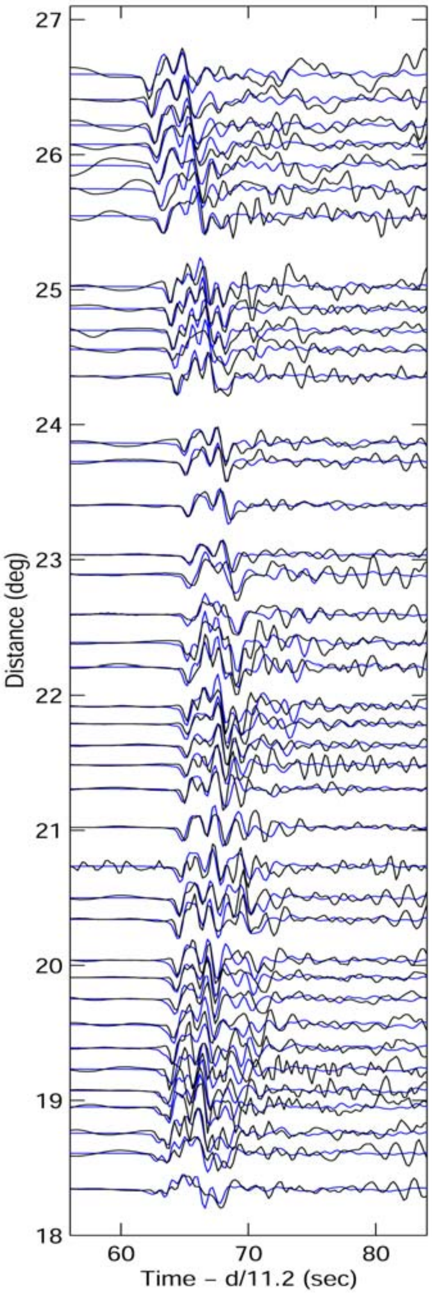

Figure 3.34 Comparison between data and synthetics for the final model (in Figure 3.32) with a 3 second advance. The black lines stand for the observations, and the blue lines stand for the synthetics.

3.6 Discussion

The final models for the P and S velocity beneath eastern Mexico are shown compared to the PREM and IASPEI models in Figure 3.35. Note that for both P and S waves, there appears to be a far larger jump at 410 km depth in our models than either of the global average models although the low velocity zone above the 410 km discontinuity makes it ambiguous to define exactly what the jump at 410 km is. When we take the total velocity increase over 20 km depth to define the discontinuity size (Melbourne and Helmberger, 1998), we find the jump is 6.2% for compressional and is 7.3% for shear at the 410 km discontinuity. The jump in velocity at the 660 km discontinuity is 3.3% for the compressional waves and is about 6.3% for the shear waves. The contrasts across the discontinuities are summarized in Table 3.3. For comparison, PREM has a P jump of 3.4% and an S jump of 4.2% at 410 km depth and a P jump of 5% and an S jump of 7% at 660 km depth. If we use the elasticity data of Sinogeiken et al. (2003) for olivine and its high pressure polymorphs then the P and S velocity jumps at 410 km depth imply 65% olivine content for the mantle beneath eastern Mexico. These values are high even with respect to the pyrolite model but the low velocity zone above the 410 km discontinuity in our model may result in an over estimate of the olivine content when using single crystal mineral physics estimates for what the jump should be. The jumps across 660 km for P and S waves imply an olivine content of 45% and 52.5% respectively, and are less than

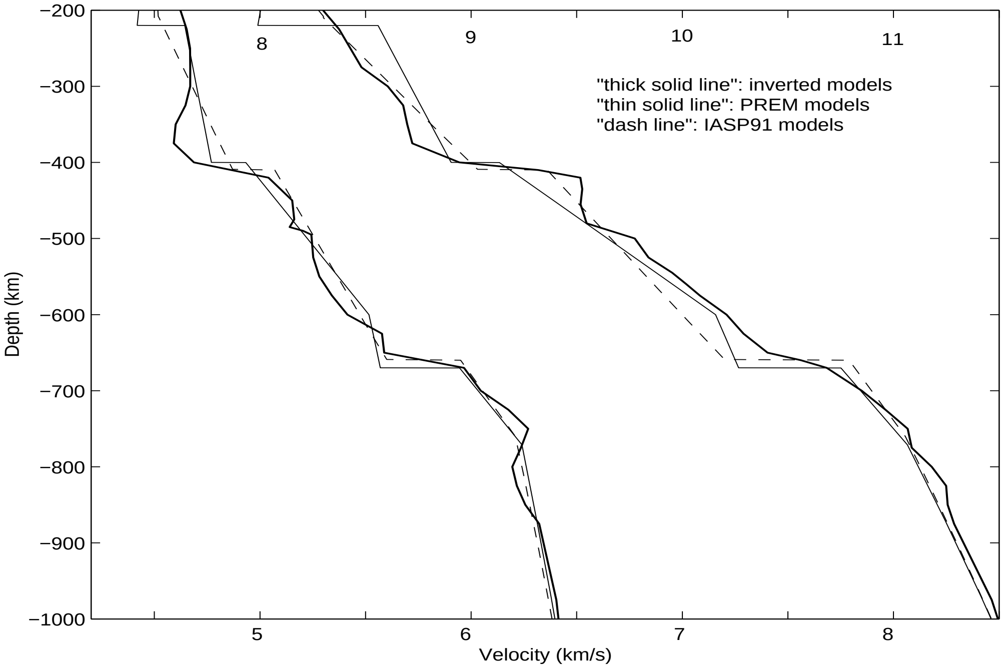

Figure 3.35 Comprison between the final models and the IASP91 and PREM models.

that of a pyrolite composition. The comparison of models in Figure 3.40 clearly shows a relatively small jump in P velocity near 660 km relative to other standard models. Two other unusual features appear in our shear model shown in Figure 3.27. The first is a low velocity zone just above the 410 km discontinuity and the second is a jump in velocity at about 600 km depth, well above the 660 km discontinuity. Neither of these features are strong in the P model and both may be related to subducted slab stagnant in the mantle transition zone.

3.6.1 Low velocity zone atop the 410 km discontinuity

We test the resolution of our model with respect to the low velocity zone above 410 km depth by running inversions of the S wave data where the gradient from 200 to 400 km is constrained to be linear but the velocity is allowed to vary. We used three different gradients in these inversions; A) an intermediate gradient, B) zero gradient, and C) a high gradient. The inverted results are shown in Figures 3.36 – 3.41. Figure 3.36 shows the starting model and the results of the inversion with constraint (A). Figure 3.37 shows the data to synthetic match for the model shown in Figure 3.36. Note that there is significant mismatch between data and synthetics at distances from 18º to 20º for this model and that the inversions that have a low velocity zone above 410 km depth provide much better fits to the data (Figures 3.9 – 3.11). In the case (A), the misfit function becomes worse suggesting that the seismic data require the low zone above the 410 km discontinuity (see Figures 3.36 and 3.37). Figure 3.38 shows the starting model and the results of the inversion with constraint (B). Figure 3.39 shows the data to synthetic match for the model shown in Figure 3.38. In case (B), the fit between the data and synthetics for the model is almost as good as that with the low velocity zone. Song et al. (2004) found a similar result in a study of the transition zone beneath the western United States. For an adiabatic temperature gradient it is highly unlikely that shear velocity would not increase with depth below 200 km (Dziewonski and Anderson, 1981). Also, receiver function analysis and ScS reverberation studies have found indications of a low velocity zone above the 410 km discontinuity in other studies (Revenaugh and Sipkin; 1994; Gilbert et al.; 2003) so that I prefer the model with the low velocity zone over the model with zero gradient from 200 to 400 km depth. Figure 3.40 shows the starting model and the results of the inversion with constraint (C). Figure 3.41 shows the data to synthetic match for the model shown in Figure 3.40. In case (C), the high gradient model between 200 km and 410 km can be easily excluded because the synthetics produced by both starting and final models do not produce a clear AB branch arrival between 18.5° and 19.5° as seen in the data (see Figure 3.41). Thus we conclude that the low velocity zone atop the 410 km discontinuity is a real feature of the upper mantle beneath eastern Mexico although its thickness is not well constrained by our data.

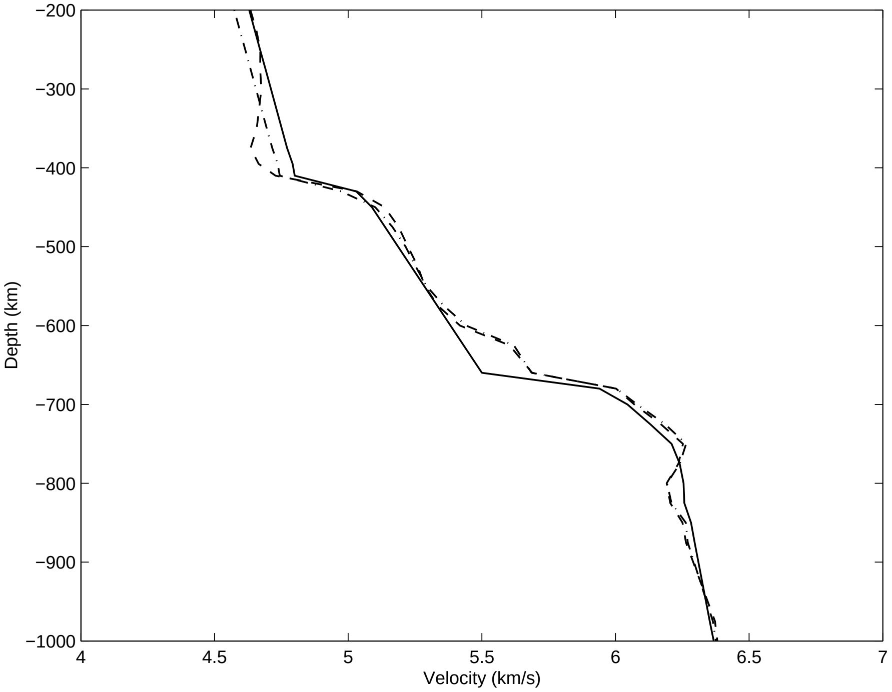

Figure 3.36 Comparison between starting, final, and constrained A final models. The dash line stands for the final model, the dash-dot line stands for the constrained final model, and the solid line stands for the common starting model.

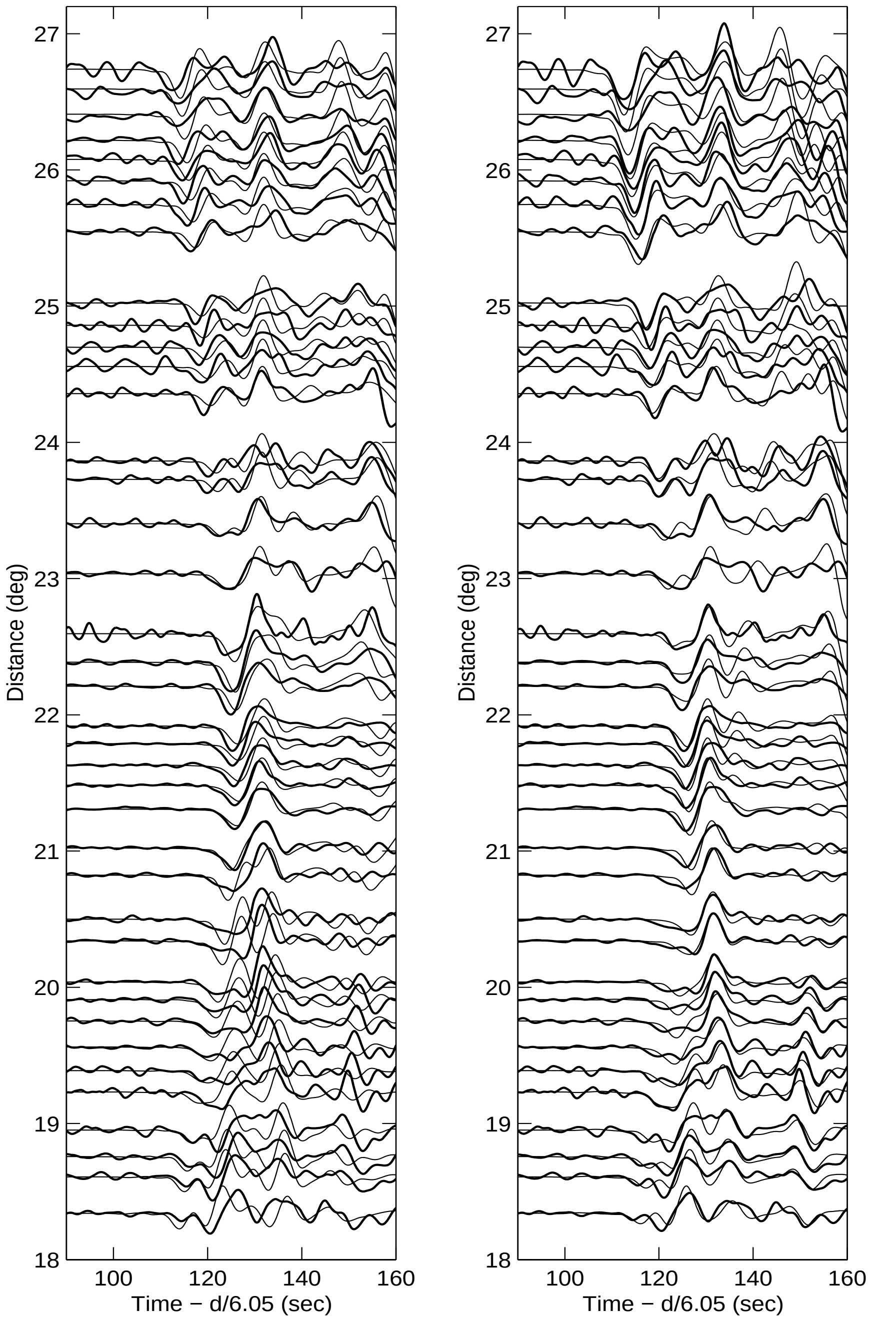

Figure 3.37 Comparison between data and synthetics for the constrained A final model. The thick black lines stand for the observations, and the thin black lines stand for the synthetics.

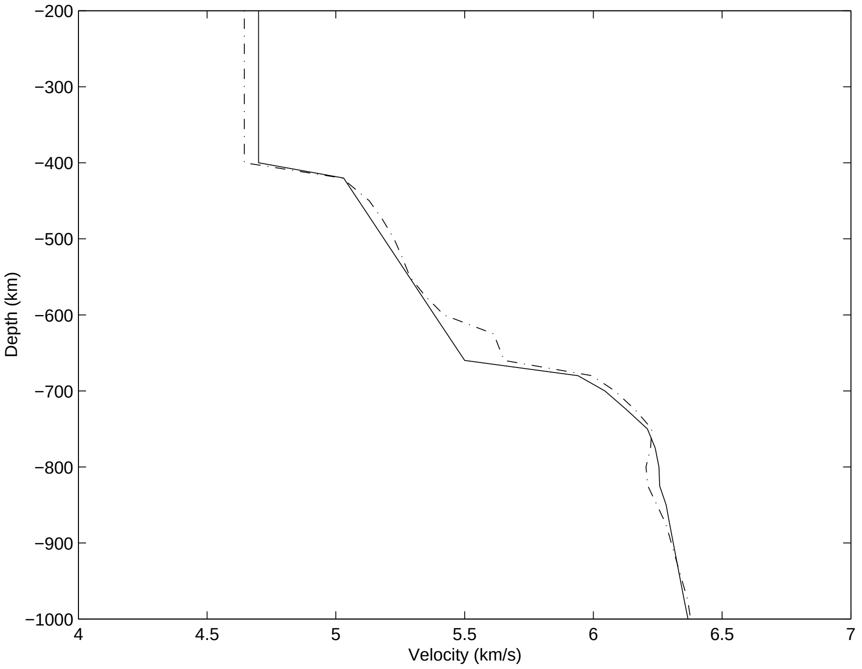

Figure 3.38 Comparison between starting and constrained B final models. The dash-dot line stands for the final model, and the solid line stands for the constrained staring model.

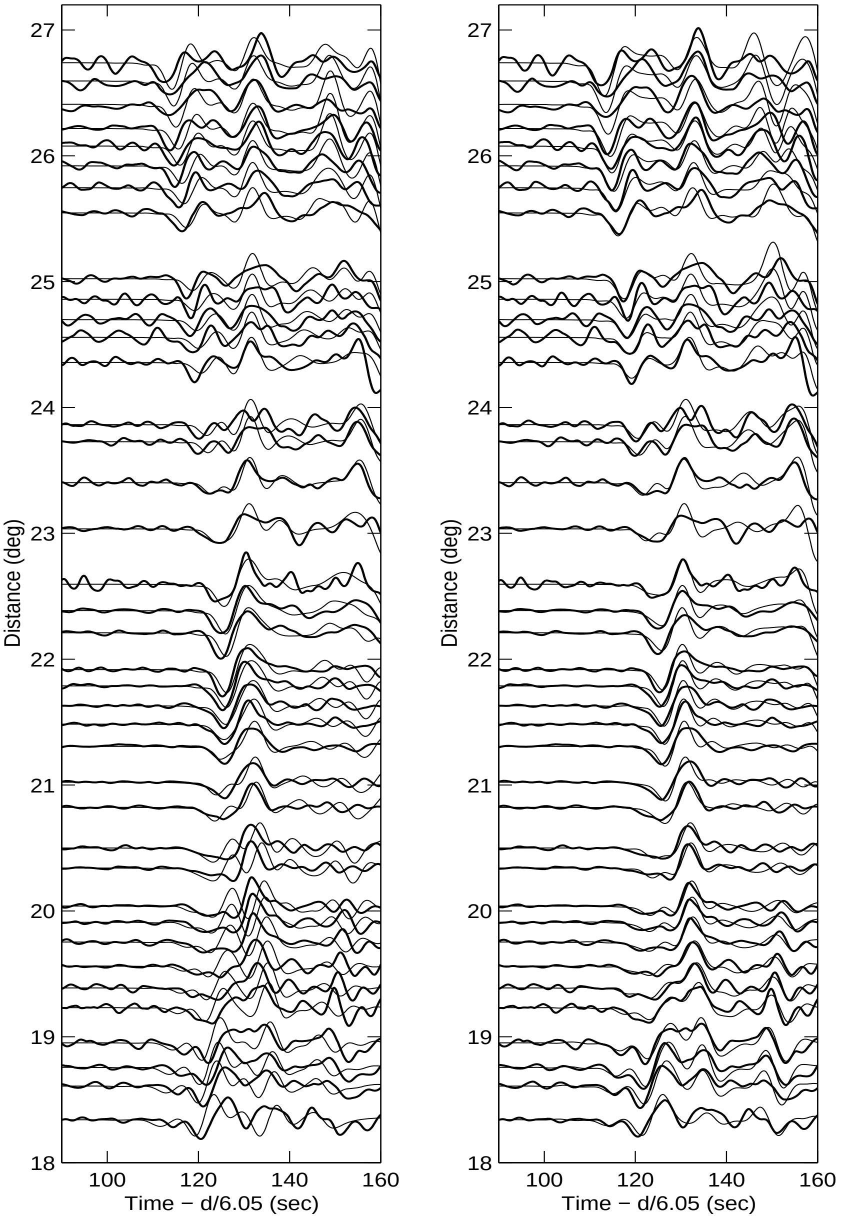

Figure 3.39 Comparison between data and synthetics for the constrained B model shown in Figure 3.38. The thick black lines stand for observations, and the thin black lines stand for the synthetics.

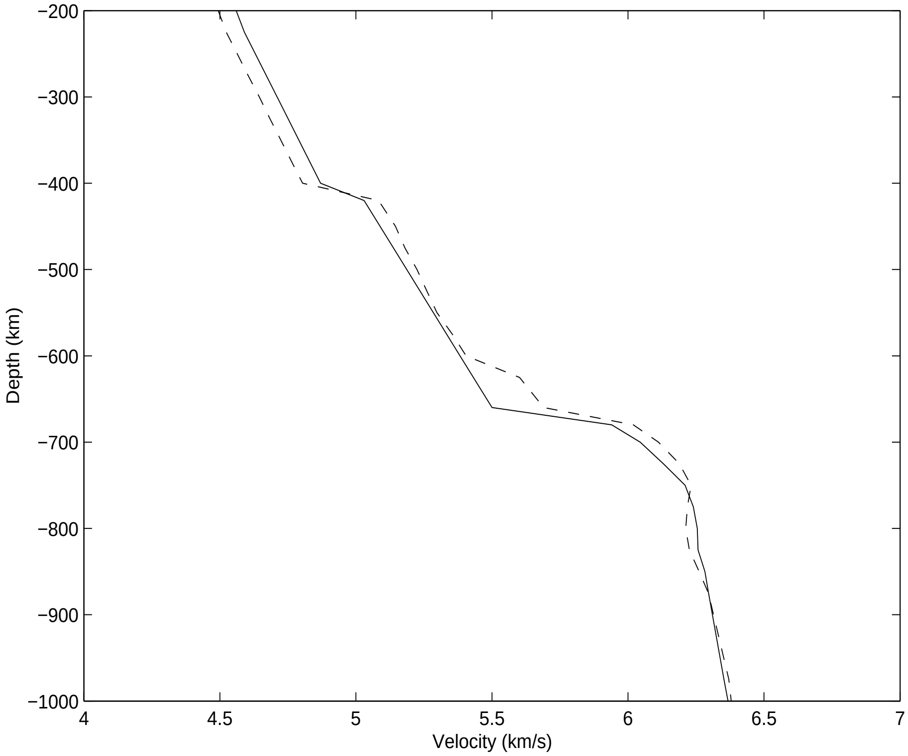

Figure 3.40 Comparison between starting and constrained C final models. The dashed line stands for the constrained final model, and the solid line stands for the starting model.

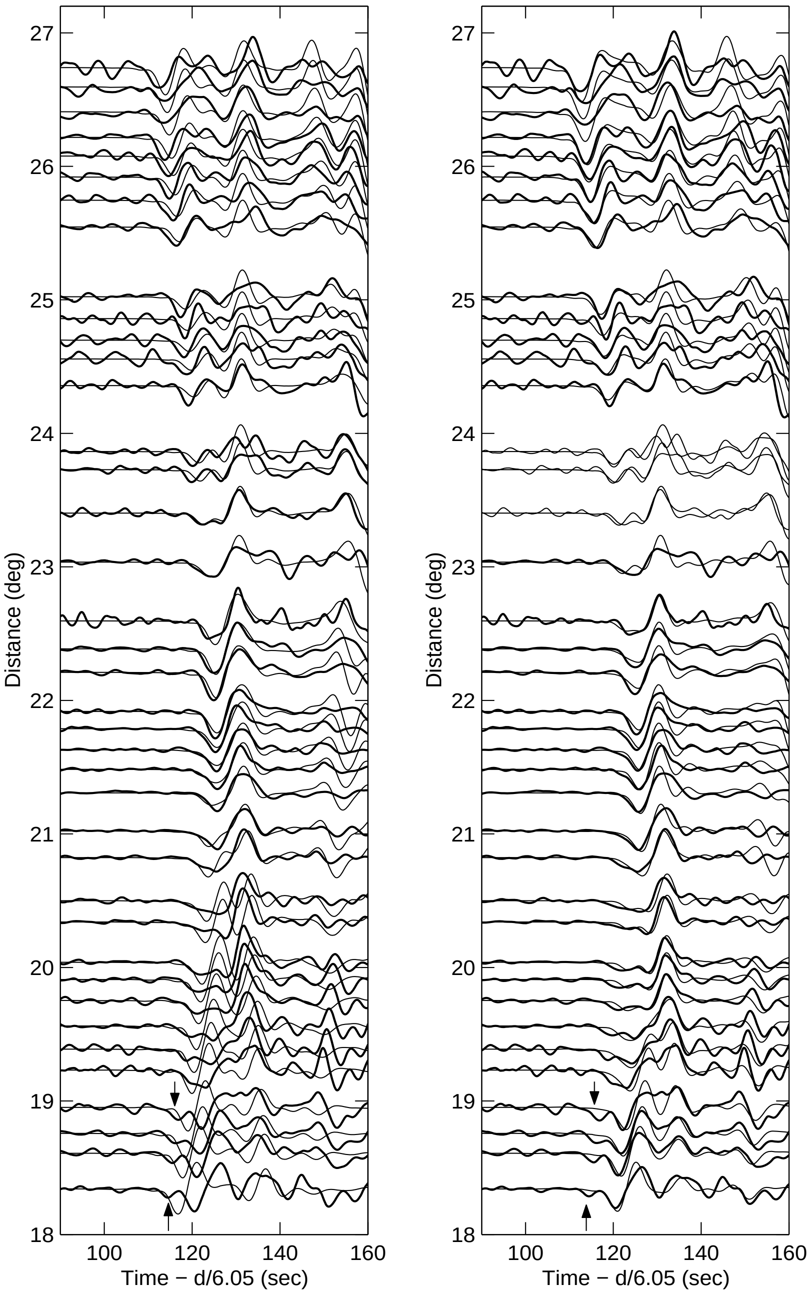

Figure 3.41 Comparison between data and synthetics for the constrained C model shown in Figure 3.40. The thick black lines stand for observations, and the thin black lines stand for the synthetics.

A low velocity zone above 410 km has been found in other studies as well. Most of these studies were in regions associated with subducted slabs (Revenaugh and Sipkin, 1994; Nolet and Zielhuis, 1994; Vinnik et al., 2003; Song et al., 2004). Revenaugh and Sipkin (1994) were the first to find a low velocity zone above 400 km depth in their ScS reverberation study of North China. They interpreted the feature as a zone of partial melting due to volatiles released by the subducting Pacific plate which is presently beneath the low velocity zone. Nolet and Zielhuis (1994) found low shear velocities beneath the Tornquist-Teisseyre zone from 300 to 500 km depth. They interpreted this anomaly as a region with higher water content than normal and postulated that the water was introduced by subduction. More recently Vinnik et al. (2003) and Song et al. (2004) have also found evidence of a low velocity zone near 400 km depth. Both of those studies were in regions where plate convergence has occurred during the past 50 Ma. It is likely the low velocity zone atop the 410 km discontinuity is due to the subduction of the Farallon plate and Cocos plate beneath the North American plate. Today, these plates are likely 600 km deep beneath eastern Mexico (Van der Lee and Nolet, 1995).

Recently, Bercovici and Karato (2003) hypothesized that water rich mantle could cause melting above the 410 km discontinuity but not below. This is due to the higher compatibility of water in transition zone minerals as opposed to olivine as well as the fact that the density of melt near 400 km depth is thought to be greater than the matrix. The fact that we find a far stronger low velocity zone in S than in P is supportive of the low velocity zone being due to partial melt that is likely due to the presence of water or other volatiles introduced in some way by subduction to the west.

3.6.2 Seismic structure within the transition zone

Our final models also have a small discontinuity near 490 km depth in P and S velocity models. Some jump in P velocity near that depth is required to fit the double arrivals shown in Figure 3.6 but there is no clear triplication in the S data that require such a feature. In fact, inversion of the S data with a small jump near 490 km depth tends to minimize the jump. We thus are not confident about the size of this discontinuity although from the P wave data it appears that some small feature exists. This discontinuity is likely the same feature imaged by Shearer (1990) at 520 km depth and may be due to the β to γ phase transition in olivine.

The jump in velocity near 600 km depth in the shear velocity model may be due to cold slab material laying on the 660 km transition zone as proposed by Van der Lee and Nolet (1997). Cammarano et al. (2003) estimated about a 0.8% change in shear velocity per 100º C change in temperature at depths near 600 km. The jump we observe of 2.4% at 600 km would imply a change in temperature of 300º C associated with the slab. This is larger than the estimated 200º C thermal anomaly estimated by Van der Lee and Nolet (1997) for the Farallon plate 26Ma after subduction. Thus, although the high gradient we observe at 600 km depth is likely due to the cold temperatures within a stagnant slab it appears that temperature alone is not sufficient to explain this feature. Perhaps this is an indication of chemical heterogeneity just above the 660 km discontinuity or to a relatively sharp phase transition within a cold transition zone.

In a stable region away from subduction zones we would expect simple structure within the transition zone with generally flat 410 and 660 km discontinuities and possibly a small phase-related discontinuity near a depth of 520 km. However, high-pressure experiments indicate that the compressional increase across the 520 km discontinuity is hard to explain with the β to γ phase transition and may be of chemical origin (Sinogeikin et al., 2003). The introduction of slabs into the transition zone creates complexities due to the subduction behavior of slabs as well as the introduction of varying chemistries and water. For example, slabs are thought to depress the 660 km discontinuity by decreasing the temperature. Consistent with this study, other studies of various subduction regions do not always find significant depressions of 660 km discontinuity and some find high-velocity features within the transition zone (Fukao et al., 1992; Niu and Kawakatsu, 1998; Brudzinski et al., 1997). Tajima and Grand (1995 and 1998) investigated the upper mantle seismic structure beneath northeastern China and Japan Sea using waveform modeling and found both high compressional wave anomalies within the transition zone with a small jump at a depth of 525 km as well as a 30 km depression of the 660 km discontinuity. Others have found seismic signatures within subduction zones (or remnant zones) which may be attributed to slab behavior (i.e. Brudzinski and Chen, 2003). To add to the complexity of the transition zone, some have concluded that there are intermittent multiple discontinuities (possibly additional phase transitions) at some depths within the upper mantle transition zone (Simmons and Gurrola, 2000; Gilbert et al., 2003).

3.6.3 Jump size of P wave velocity at 660 km discontinuity

From the comparison of models shown in Figure 3.35 the jump in velocity at 660 km depth for P waves is significantly smaller than that of the published standard models. Our results are also consistent with the results of Shearer and Flanagan (1999) and Estabrook and Kind (1996) who found far smaller jumps in P velocity at 660 km depth than the PREM model and also found an inconsistency between their seismic results for P wave velocity jump at 660 km depth and predictions for the pyrolite model. In Figures 3.42 and 3.43 we show a comparison of P data and synthetics for an altered model with a larger jump (5%) in velocity at 660 km depth. Note the greater misfit between data and synthetics for this model as compared to our preferred model (Figure 3.35). For the profile examined here the jump in velocity at 660 km depth for P waves must be smaller than in the standard models. We find the P jump at 660 km depth appears to be too small for an olivine rich mantle. The region we have sampled likely has a cold transition zone based on the tomography model of Van der Lee and Nolet (1997). They find higher than average shear velocities from 550 to 650 km depth in eastern Mexico and identify this feature with remnants of the Farallon plate that subducted roughly 30 Ma. It may be that the deep transition zone under eastern Mexico has a chemical anomaly associated with subducted slab – for example a layer of eclogite rich mantle ponded near the 660 km depth discontinuity as proposed by Ringwood and Irifune (1988). Further detailed studies of the transition zone in other regions will likely be required before definitive conclusions can be drawn with regard to a change in major element chemistry in the deep transition zone.

3.7 Conclusion

The seismic structure of the upper mantle beneath eastern Mexico where the Cocos plate is subducted into the transition zone is investigated using triplicated waveform observations recorded by the 950 km long La Ristra seismic array. We applied a waveform inversion technique to one of the most densely spaced coincident P and S profiles studied to date. The compressional and shear wave observations are produced by a common earthquake that occurred at the border of Mexico and Guatemala. Our results reveal that there is a 50 km thick

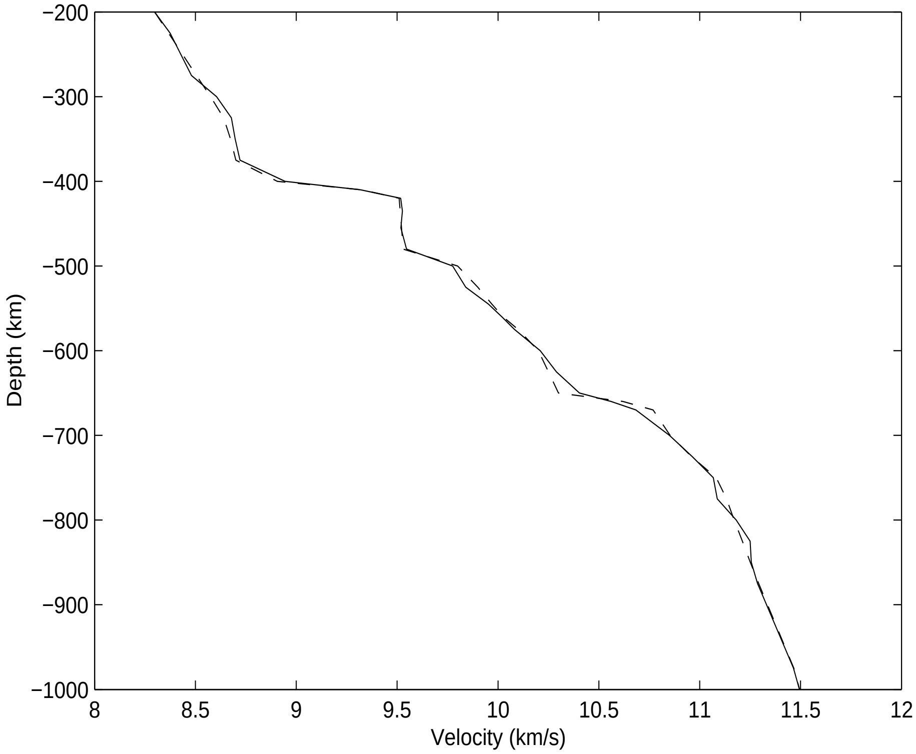

Figure 3.42 Modification of our preferred P model that matches travel times but has a larger jump in velocity at 660 km depth (5%). The solid line is the preferred model shown in Figure 3.25.

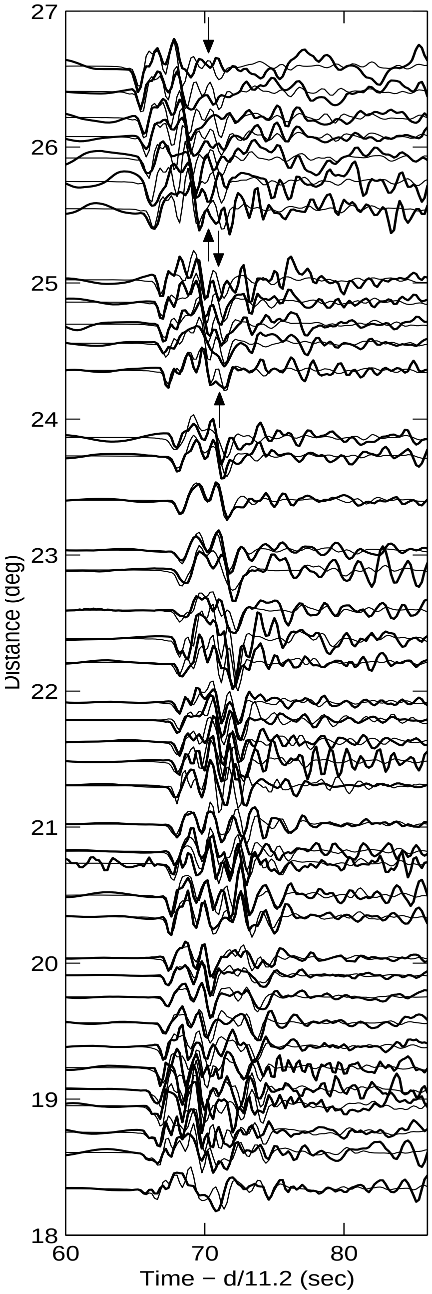

Figure 3.43 Comparison of P data and synthetics calculated using the modified P model shown in Figure 3.42. Arrows indicate misfits in the waveforms that are worse than for our preferred model, and the heavy black lines show the data.

low-velocity zone atop the 410 km discontinuity, which is more prominent in the shear model than in the compressional model. The best fitting models in this study region have velocity increases of 6.2% for compressional velocity and 7.3% for shear velocity across the 410 km discontinuity. Across the 660 km discontinuity, we find velocity jumps of 3.3% for P-wave and 6.3% for S-wave. These models show significantly larger velocity increases across the 410 km discontinuity than the PREM and IASPEI models. Our results show that the velocities in our compressional velocity model within the transition zone are significantly larger than in the standard models (see Figure 3.35). In addition, there is a small jump at 490 km and the S-wave velocities from 600 km to 660 km are significantly larger than those in the SNA model.

From the size of the velocity jumps across the discontinuities, the olivine content can be estimated for the upper mantle. In this study, the velocity increases across the discontinuities imply that the content of olivine are 65% at the 410 km depth and 45% and 52.5% at the 660 km depth for the compressional and shear wave models respectively (see Table 3.4). At face value, these results show that the content of olivine in the upper mantle beneath eastern Mexico changes with depth within the transition zone. This may be due to the presence of a subducted slab stagnant above the 660 km discontinuity. The olivine content calculated for the jump at 490 km is assuming that this feature is associated with the phase change usually referred to as the 520 km discontinuity. A shallow 520 km discontinuity with a larger jump than expected possibly indicates chemical variation combined with a decrease in temperature (Sinogeikin et al., 2003). These results show that the content of olivine in the upper mantle beneath eastern Mexico changes with depth within the transition zone. The mantle composition implied by our models near 400 km depth is closer to pyrolite than what standard upper mantle models imply. Near 660 km depth our models imply a low olivine content and the P and S models are incompatible.

The transition zone of the upper mantle beneath eastern Mexico is likely to have had subducted lithosphere enter it within the last 30 Ma. Tomography also shows that it may be a location where slab is stagnant above the 660 km discontinuity. Given this tectonic regime, we interpret that the low velocity zone near 410 km beneath eastern Mexico is due to partial melting of a dense silicate layer caused by water release associated with the subduction of the Farrallon or Cocos plate as suggested by (Revenaugh and Sipkin, 1994 and Song et al., 2004). We conclude that the difference between P and S jumps at the 660 km discontinuity and the difference of the olivine content between the 410 km and 660 km discontinuities result from chemical heterogeneity generated by the stagnation of the subducted plate near the 660 km discontinuity (Tajima and Grand, 1998). The seismic anomalies within the transition zone in our models, particularly the shear velocity increase from 600 to 660 km, support the idea that the subducting Cocos plate has accumulated within the transition zone in this geographic region.

We have interpreted some unusual features in our models in terms of the effect of subduction. It is unclear, however, how ubiquitous a low velocity zone atop the 410 km discontinuity is or how common are high gradients near 600 km depth. With the advent of large temporary deployments of broad band seismometers more detailed regional studies of the upper mantle transition zone should be possible in many tectonic environments. The results of such studies should lead to better constrained interpretations of the seismic models and thus a better understanding of the mineralogy and dynamics of the upper mantle.

REFERENCES

Bass, J. D. and D. L. Anderson, 1984. Composition of the upper mantle: Geophysical tests of two petrological models, Geophys. Res. Leett., 11, 237-240.

Bercovici, D. and S. Karato, 2003. Whole mantle convection and the transition zone water filter, Nature, 425, 39-44.

Bina, C. R. and B. J., Wood, 1984. The eclogite to garnetite transition: experimental and thermodynamic constraints, Geophys. Res. Lett., 11, 955-958.

Bina, C. R. and B. J., Wood, 1987. Olivine-spinel transitions: experimental and thermodynamic constraints for the nature of the 410 km seismic ddiscontinuity. J. Geophys. Res., 92, 4,853-4,866.

Bina, C. R. and G. Helffrich, 1994. Phase transition Claperon slopes and transition zone seismic discontinuity topography, J. Geophys. Res., 99 (B8), 15,853-15,860.

Bina, C. R., 1993. Mutually consistent estimates of upper mantle composition from seismic contrasts at 400 km depth, Pure Appl. Geophys., 141, 101-109.

Brudzinski, M. R., W.-P. Chen, R. L. Nowack, and B.-S. Huang, 1997. Variations of P wave speeds in the mantle transition zone beneath the northern Philippine Sea, J. Geophys. Res., 102, 11,815-11,827.

Brudzinski, M. R. and W.-P. Chen, 2003. A Petrologic Anomaly Accompanying Outboard Earthquakes Beneath Figi-Tonga: Corresponding Evidence from Broadband P and S Waveforms, Journal of Geophysical Research, 108, B6, 2299, doi:10.1029/2002JB002012.

Cammarano, F., S. Goes, A. Deuss, and D. Giardini, 2005a. Is a pyrolite mantle compatible with seismic data? Earth Planet. Sci. Lett., 232, 227-243.

Cammarano, F., A. Deuss, S. Goes, and D. Giardini, 2005b. One-dimensional physical models for the upper mantle and transition zone: Combining seismic and mineral physicas constraints, J. Geophys. Res., 110, B01306, doi:10.1029/2004JB003272.

Duess, A. and J. Woodhouse, 2001. Seismic observations of splitting of the mid-transition zone discontinuity in the Earth's mantle, Science, 294, 354-357.

Dziewonski, A. and D. Anderson, 1981. Preliminary reference Earth model, Phys. Earth Planet. Int., 25, 297-356.

Estabrook, C. H. and R. Kind, 1996. The nature of the 660-kilometer upper-mantle seismic discontinuity from precursors to the PP phase, Nature, 274, 1179-1182.

Flanagan, M. P. and Shearer, P. M., 1998, Global mapping of topography on transition zone discontinuities by stacking SS precursors, J. Geophys. Res., 103 (B2): 2,673-2,692.

Fuchs, K. and G. Muller, 1971. Computation of synthetic seismograms with the reflectivity method and comparison with observations, Geophys. J. R. Astron. Soc., 23, 417-433.

Fukao, Y., M. Obayashi, H. Inoue, and M. Nenbai, 1992. Subducting slabs stagnant in the transition zone, J. Geophys. Res., 97, 4,809-4,822.

Gao, W., S. P. Grand, W. S. Baldridge, D. Wilson, M. west, J. F. Ni, and R. Aster, 2004. Upper mantle convection beneath the central Rio Grande rift imaged by P and S wave tomography, J. Geophys. Res., 109, B03305, doi:10.1029/2003JB002743.

Gilbert, H. J., A. F., Sheehan, K. G., Dueker, and P. Molnar, 2003. Receiver functions in the western United States, with implications for upper mantle structure and dynamics. J. Geophys. Res. 109(B5), doi:10.1029/2001JB001194.

Grand, S. P. and D. Helmberger, 1984. Upper mantle shear structure of North America, Geophys. J. R. astr. Soc. 76, 399-438.

Grand, S. P., R. D. van der Hilst, and S. Widiyantoro, 1997. Global seismic tomography: A snapshot of convection in the Earth, Geo. Soc. Am. Today, 7(4), 1-7.

Gu, Y., Dziwonski, A. M. & Ekstrom, G. 2003. Simultaneous inversion for mantle and topography of transition zone discontinuities. Geophys. J. Int., 154, 559-583.

Helffrich, G. R. and B. J., Wood, 1996. 410-km discontinuity sharpness and the form of the olivine α–β phase diagram: Resolution of apparent seismic contradictions, Geophys. J. Int., 126, F7-F12.

Helffrich, G. R., E. Asencio, J. Knapp and T. Owens, 2003. Transition zone structure in a tectonically inactive area: 410 and 660 km discontinuity properties under the northern North Sea, Geophys. J. Int., 155, 193-199.

Kennett, B. L. N. and E. R. Engdahl, 1991. Traveltimes for global earthquake location and phase identification, Geophys. J. Int., 105, 429-465.

Kennett, B. L. N. E. R. Engdahl, and R. Buland, 1995. Constraints on seismic velocities in the Earth from travel times, Geophys. J. Int., 122, pp. 403-416.

LeFevre, L. V. and D. V., Helmberger, 1989. Upper mantle P structure of the Canadian shield, J. Geophys. Res., 94, 17,749-17,765.

Li, B., 2003. Compressional and shear wave velocities of ringwoodite γ-Mg_2SiO_4 to 12 GP, American Mineralogist, 88, 1,312-1,317.

Li, B., Y. R. C. Liebermann, and D. J. Weidner, 1998. Elastic Moduli of Wadsleyite (β-Mg_2Sio_4) to 7 Gigapascals and 873 Kelvin, Science, 281, 675-677.

Matzel, E., 2002. The anisotropic seismic structure of the Earth's mantle: Investigations using full waveform inversion, Dissertation, The University of Texas at Austin.

Matzel, E. and S. P. Grand, 2004. The anisotropic seismic structure of the East European platform, J. Geophys. Res.,109, B01302, doi:10.1029/2001JB0.

Melbourne, T. and D. V. Helmberger, 1998. Fine structure of the 410 km discontinuity, J. Geophys. Res., 103, 10,091-10,102.

Mora, P., 1988. Elastic wave-field inversion of reflection and transmission data, Geophysics, 53, 6, 750-759.

Niu, F. and H. Kawakatsu, 1998. Determination of the absolute depths of the mantle transition zone discontinuities beneath China: Effect of stagnant slabs on transition zone discontinuities, Earth, Planets and Space, 50, 965-975.

Nolet, G., S. P. Grand, and B. L. N., Kennett, 1994. Seismic heterogeneity in the upper mantle, J. Geophys. Res., 99, pp. 23,753-23,766.

Nolet, G. and A. Zielhuis, 1994. Low S velocities under the Tornquist-Teisseyre zone: Evidence for water injection into the transition zone by subduction, J. Geophys. Res., 99, 15,813-15,820.

Revenaugh, J., and S.A. Sipkin, 1994. Seismic evidence for silicate melt atop the 410-km mantle discontinuity, Nature, 369, 474-476.

Ringwood, A. E., 1975. Composition and petrology of the Earth’s mantle, McGraw-Hill, New York.

Ringwood, A. E. and T. Irifune, 1988. Nature of the 650-km seismic discontinuity: implications for mantle dynamics and differentiation, Nuture, 331, 131-1136.

Romanowicz, B., 1991. Seismic tomography of the Earth's mantle, Annu. Rev. Earth Planet. Sci., 19, 77-99.

Ryberg, T., F. Wenzel, A. V. Egorkin, and L. Solodilov, 1997. Short-period observation of the 520 km discontinuity in the northern Eurasia, J. Geophys. Res., 102, 5,413-5,422.

Shearer, P. M., 1990. Seismic imaging of upper-mantle structure with new evidence for 520-km discontinuity, Nature, 344, 121-126.

Shearer, P. M., 1993. Global mapping of upper mantle reflectors from long-period SS precursors, Geophys. J. Int., 115, 878-904.

Shearer, P. M. and M. P. Flanagan, 1999. Seismic velocity and density jumps across the 410- and 660-kilometer discontinuities, Science, 285, 1545-1548.

Simmons, N. A. and H. Gurrola, 2000. Multiple seismic discontinuities near the base of the transition zone of the Earth’s mantle, Nature, 405, 559-562.

Sinogeikin, S. V., T. Katsura, and J. D. Bass, 1998. Sound velocities and elastic velocities of Fe-bearing wadsleyite and ringwoodite, J. Geophys. Res., 103, pp. 20,819-20,825.

Sinogeikin, S. V., J. D. Bass, and T. Katsura, 2003. Single-crystal elasticacity of ringwoodite to high pressure and high temperatures: implications for 520 km seismic discontinuity, Phys. Earth. Planet. Inter., 136, 41-66.

Song, T., D. Helmberger, and S. P. Grand, 2004. Low-velocity zone atop the 410-km seismic discontinuity in the northwestern United States, Nature, 427, 530-533.

Tajima, F. and P. Grand, 1995. Evidence of high anomalies in the transition zone associated with southern Kurile subduction zone, Geophys. Res. Lett., 22, 3,139-3,142.

Tajima, F. and P. Grand, 1998. Variation of transition zone high-velocity anomalies and depression of 660 km discontinuity associated with subduction zones from the southern Kuriles to Izu-Bonin and Ryukyu, J. Geophys. Res., 103, 15,015-15,036.

Van der Lee, S. and G. Nolet, 1997. Seismic image of the subducted trailing fragments of the Farallon plate, Nature, 386, 266-289.

Vinnik, L., M. R. Kumar, R. Kind, and V. Farra, 2003. Super-deep low-velocity layer beneath the Arabian plate, Geophys. Res. Lett., 30(7), 1415, doi:10. 1029/2002GL016590.

Walck, M. C., 1984. The P-wave upper mantle structure beneath an active spreading center – the Gulf of California. Geophys. J. R. astr. Soc., 76, 697-723.

Weidner, D. J., 1985. Mineral physics test of a pyrolite mantle, Geophys. Res. Lett., 12, 417-420.

Wilson, D., Aster, R., and the RISTRA Team, 2003. Imaging Crust and Upper Mantle Seismic Structure in the Southwestern United States Using Teleseismic Receiver Functions, The Leading Edge, 22(3), 232-237.

Wilson, D., R. Aster, J. Ni, S. Grand, M. West, W. Gao, W. S. Baldridge, and S. Semken, 2005. Imaging the seismic structure of the crust and upper mantle beneath the Great Plains, Rio Grande Rift, and Colorado Plateau using receiver functions, J. Geophys.Res., 110, B05306, ido:10.1029 2004JB00 3492.

Wood, B., 1995. The effect of H_2O on the 410-kilometer seismic discontinuity, Science, 268, 74-76.

Table 3.1. Event's parameters used in the inversion

Date	Time	Latitude	Longitude	Depth	Mag.	Strike	Dip	Slip
2001/1/19	1:12:55.8	15.33°N	92.93°W	83 km	5.4Mb	140	13	–91

Table 3.2 S wave misfit values for perturbation to the discontinuities

660 km\410 km discontinuity	370 km	400 km	430 km
640 km	0.1452	0.1415	0.1472
670 km	0.1715	0.1384	0.1558
700 km	0.2810	0.1800	0.1615

Table 3.3 Size of jump at the discontinuities

	Jump size (P wave)	Jump size (S wave)
400 km	6.2%	7.3%
490 km	>1.9%	1.8%
660 km	3.3%	6.3%

Table 3.4 Olivine content implied by size of jump at the discontinuities

	Olivine content (P wave)	Olivine content (S wave)
400 km	65%	65%
490 km	>90%	62%
660 km	45%	52.5%

Chapter 4

JOINT INVERSION OF SEISMIC BODY AND SURFACE WAVES FOR REGIONAL SCALE UPPER MANTLE

4.1 Abstract

Body and surface wave tomography have complementary strengths when applied to regional scale studies of the upper mantle. We present a straight-forward tecnique for their joint inversion which hinges on treating surface waves as horizontally-propagating rays with deep sensitivity kernels. This formulation allows surface wave phase or group measurements to be integrated directly into existing body wave tomography inversions with modest effort. We apply the joint inversion to the synthetic case and to data from the La Ristra project in the southwest United States. The results of synthetic resolution tests and real data inversions demonstrate that the joint inversion produces a better fit to the combined dataset, not merely a compromise. For large arrays, this method offers an improvement over augmenting body wave tomography with a one-dimensional model. The joint inversion combines the absolute velocity of a surface wave model with the high resolution afforded by body waves—both qualities that are required to understand regional-scale mantle phenomena.

4.2 Introduction

Seismic tomography, based on dense regional networks, has proven to be one of the most powerful tools for understanding the tectonic regimes which comprise the Earth including continental shields (e.g., James et al., 2001), transforms (e.g. Thurber et al., 2003), continental rifts (e.g. Gao et al., 2004), oceanic plates (e.g. The MELT Seismic Team, 1998), subduction zones (e.g. Zhao et al., 1992) and mid-ocean ridges (e.g. Dunn et al., 2000). Models of seismic velocity have been used to infer the thickness of the crust and lithosphere, thermal structure, density, magma content, and mineralogy—all principle controls on plate tectonics.

The most common type of regional tomography uses teleseismic body wave traveltimes to distinguish velocity perturbations beneath the array with upper mantle resolution as fine as 50 km. Source-side mantle heterogeneities are tacitly assumed to effect the entire array in a similar fashion. As discussed in Chapter 2, to allow for distant structure, it is necessary to remove the mean delay time for each event. This process limits the data to constrainting the relative lateral differences in velocity structure. Surface waves offer a different view of the mantle and are widely used to determine mantle shear velocity structure for large aperture investigations. Since surface waves sweep progressively across Earth's surface, absolute velocity can be determined from inter-station traveltimes. The principal drawback is the limited lateral sensitivity inherent in measuring long-period signals over short baselines. The lateral scale of resolved features for surface wave methods is frequently an order of magnitude greater than the corresponding body wave tomography.

Because the two types of data are complementary, their joint interpretation is of wide interest. Such joint inversions have been done on a global scale for some time (e.g., Antolik et al., 2003), however, different issues exist for regional-scale joint inversions since body waves are typically demeaned first. The simplest approach is to augment relative tomography results by adding a 1-D structure extracted from a global surface wave model (Lévêque and Masson, 1999). This approach depends optimistically on the local accuracy of the global model. Allen et al. (2002) eliminate this uncertainty by deriving an optimum 1-D model specific to the region of study. When the study area is sufficiently large that surface wave velocities change across the array, a 1-D profile is no longer a suitable "background" structure. However, the variation in surface wave velocities can be exploited to refine features within the array, in addition to determining absolute velocity. Here, we demonstrate the benefits of a true joint inversion on synthetic and real data from the La Ristra experiment. While there are several ways to achieve a joint interpretation of body and surface wave data (e.g., Van der Lee et al., 2003), our goal is to provide a method that builds on the widely-used concepts (and codes) of regional body wave tomography and can be implemented with modest effort.

4.3 Method

The sensitivity of a body wave travel time to slowness in an arbitrary gridded model is, in a ray theoretical sense, the ray length in each block (Figure 4.1). These sensitivities can be inverted with residual traveltimes to predict models that better fit the data. Phase and group velocities of Rayleigh and Love waves can be measured by one of severals techniques. Some include higher modes (e.g. Nolet, 1975), and/or multipathing (e.g. Forsyth et al., 1998). Though a few waveform-based techniques do not require a direct measure of velocities (e.g., Nolet, 1990) we assume here that a set of surface wave velocities is extracted from the data.

The crux of our approach is to treat surface wave measurements as travel times between stations. Many surface wave algorithms produce velocity, but the conversion of velocity (and associated errors) into travel time is trivial. Each travel time corresponds to a ray traveling horizontally through a series of blocks in the model. It is the same formulation used for body waves, except that the surface wave “ray” has a sensitivity that is very wide in depth (Figure 4.1). If the same model space is used to parameterize the surface and body wave problems, then the sensitivity terms take the same form, $\partial t_i/\partial S_j$, and the surface wave terms

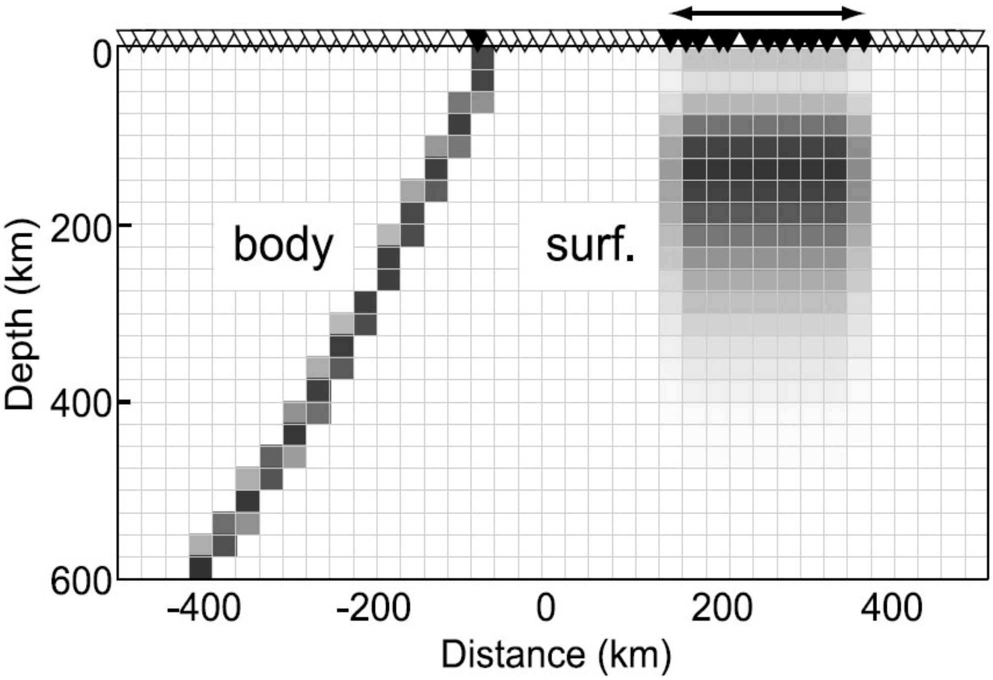

Figure 4.1 Some typical kernels ($\partial t_i/\partial S_j$) for the body and surface waves superimposed on the model parameterization. The seismic stations are shown in white. The body wave kernel is for a teleseismic S wave recorded at the black station. The surface wave kernel is for a 90 sec Rayleigh wave recorded across a suite of stations in black. Darker cells have a larger influence on the traveltime.

can be added as an additional set of equivalent ray paths. These terms can be derived from velocity-based 1-D sensitivity kernels as

$$\frac{\partial t_i}{\partial S_j} = l_{i,j} \cdot \frac{\partial C(P_i)}{\partial Vs_j} \cdot \left(\frac{Vs_j}{C(P_i)} \right)^2 \tag{4.1}$$

where $C(P_i)$ is the phase (or group) velocity of the ith ray with period P, and $l_{i,j}$ is the horizontal length of the ith ray in the jth model block. $\partial C/\partial Vs$ are phase (or group) velocity derivatives with respect to shear velocity integrated over the depth range of block j. The final term converts the sensitivities from velocity to slowness, based on the starting model.

A weighting scheme is necessary to balance the different measurement errors and number of samples in the body and surface wave datasets. Body wave errors are based on the variance in travel times from clusters of events. Surface wave errors are derived from comparisons of multiple events propagating both directions along the array. The inclusion of surface wave travel time errors is particularly important because they vary greatly with period and station spacing. The simplified representation of surface and body waves as rays introduces errors as well (Spetzeler et al., 2002; Tanimoto, 2003). Though difficut to quantify, this error has been roughly estimated for the surface waves (West et al., 2004). We invert the data using a weighted damped least squares inversion to incorporate these errors and to allow for regularization.

$$G\Delta S = \Delta t \tag{4.2}$$

where Δt is a vector of body and syrface wave traveltime residuals, G contains body and surface wave sensitivity kernels ($\partial t_i/\partial S_j$), and ΔS is the shear wave slowness improvement. We solve equation (4.2) with a kind of the conjugate gradient algorithms (Press, 1992). Generally the two types of kernels seek slightly different models. The surface wave terms may seek an offset in absolute velocity, while the body wave terms seek roughly equal proportions of high and low perturbations. This difference is easily accommodated by using a 1-D starting model optimized to fit surface waves.

4.4 Synthetic tests

We test the approach on an artificial model with challenges for each type of data. Velocities from AK135 Earth model (Kennett et al. 1995) are sampled onto constant velocity blocks that are 0.25 degrees in width by 25 km in depth (Figure 4.1). We add to this a high velocity sub-crustal layer across the model to mimic a shield-like lithosphere (Figure 4.2). Half of the model includes a low velocity asthenospheric channel. Just above the transition zone we include three narrower high velocity features.

We base our body and surface wave coverage on the data and geometry of the recent Ristra project in the southwestern United States. S wave coverage includes 2164 S, ScS and SKS arrivals normalized by backazimuth and epicentral distance discussed in Chapter 2. Fundamental mode Rayleigh wave measurements include 650 inter-station traveltimes at periods of 30-150 s (West et al., 2004).

We first invert the surface and body wave data independently. The inverted results show in Figures 4.2 and 4.3 respectively. The surface wave inversion recovers broad shallow velocity features. The lithosphere and low velocity channel are recovered though smeared in depth due to the smooth nature of the surface wave sensitivities. The deeper features are too narrow to be resolved though they do elevate velocities across this depth. At these depths, features must be several hundred kilometers wide to overcome the higher measurement error of long period waves. The body wave inversion demonstrates different strengths. The point features above the transition zone are well-resolved. It is consistent with the results of checkerboard tests shown in Chapter 2 that demonstrated that 50 km blocks are well resolved to depths of 600 km beneath most of the array. Because the travel times have been demeaned, the anomalies show up as small alternating high and low anomalies. Figure 4.3 looks worse than typical resolution tests because the mean lateral anomalies are non-zero. However, the peak to peak amplitudes are similar to the synthetic model. The low velocity channel is detected, but it is smeared significantly in depth. As before, the low velocity channel shows up as fast on the right side and slow on the left. The continuous lithosphere is not resolved since it affects all rays in a similar fashion. The joint inversion returns a much improved model (Figure 4.4). If the

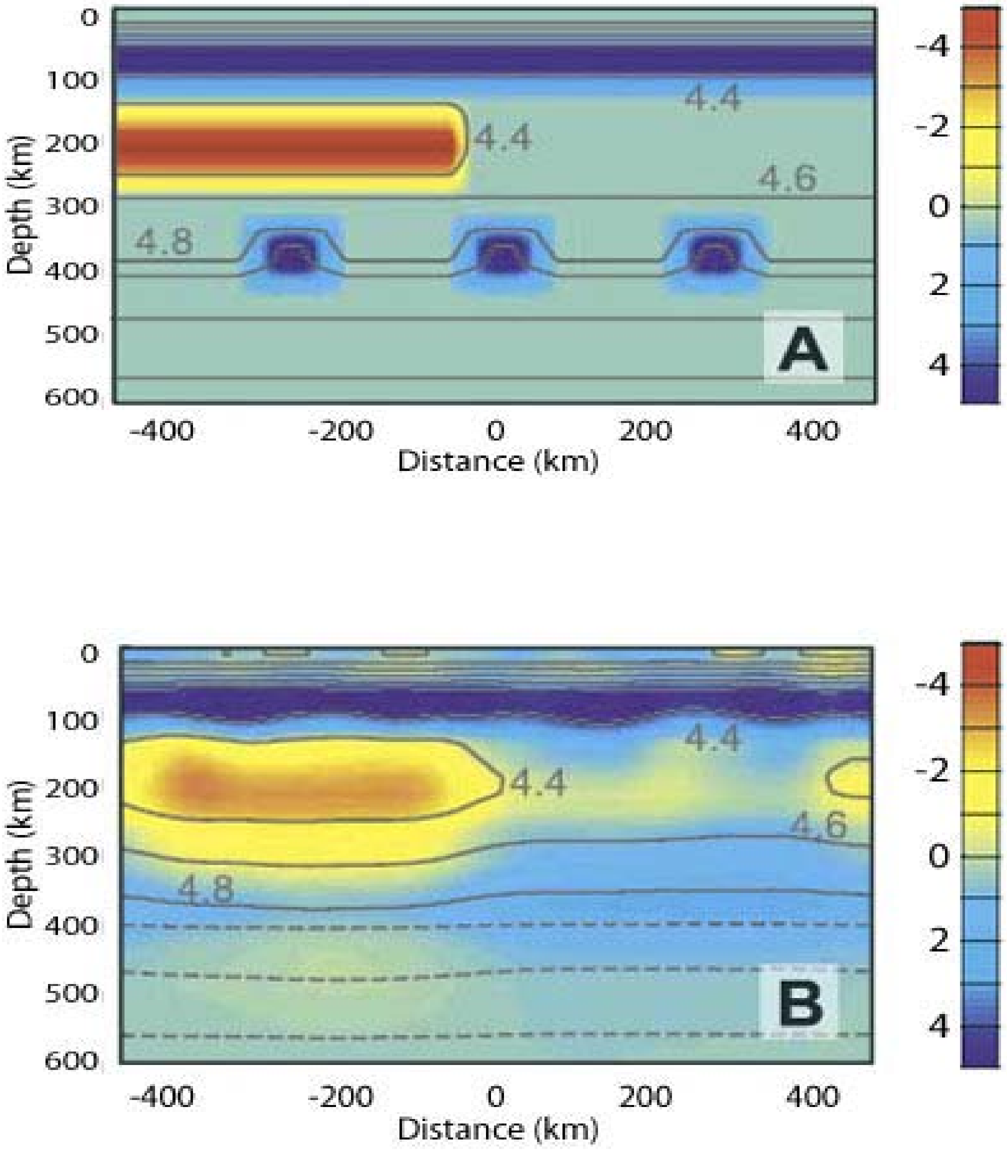

Figure 4.2 Synthetic resolution test for the surface wave inversion. The top panel shows the test input structure. The lower panel shows the result from inverting surface wave data alone. The color bar represents velocity perturbation (%).

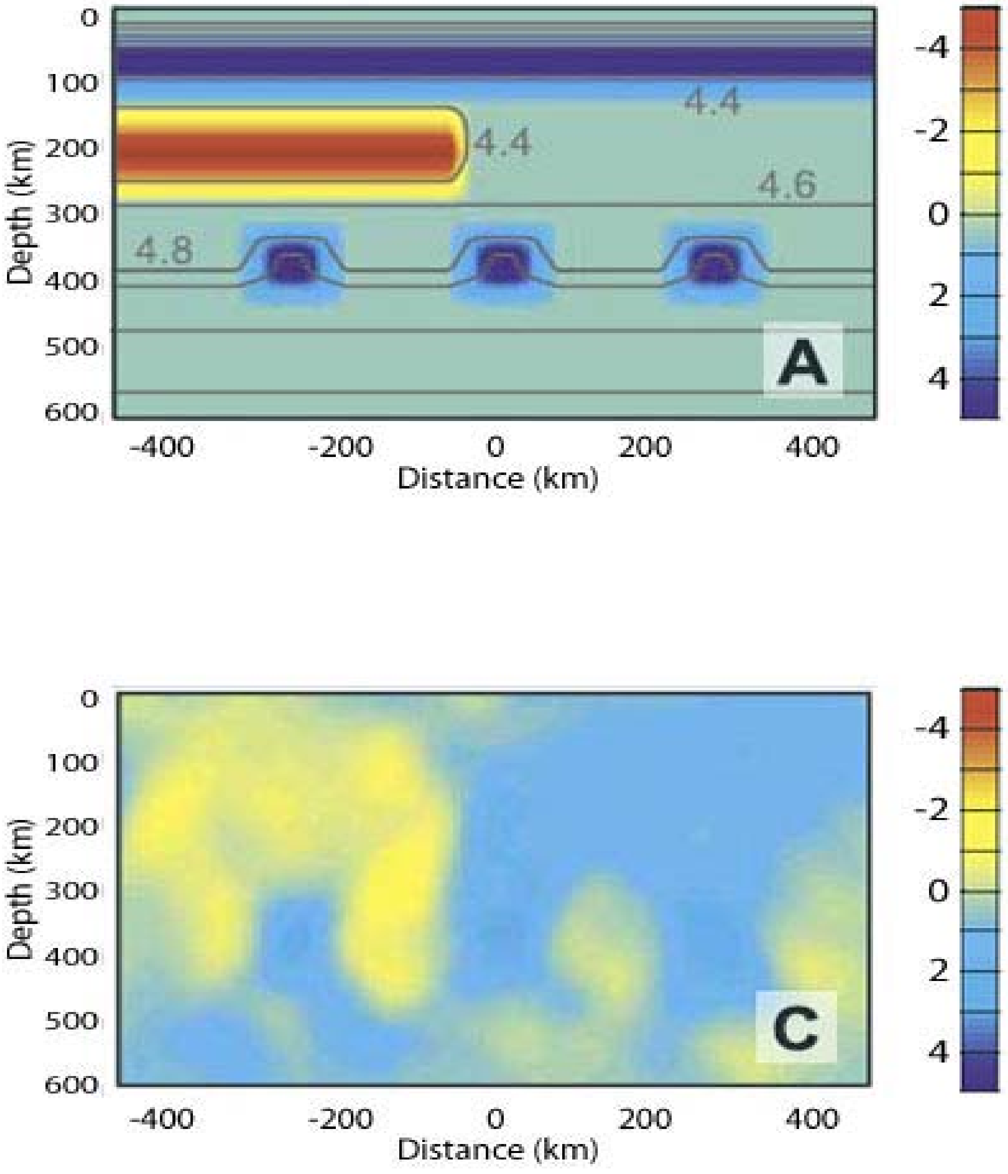

Figure 4.3 Synthetic resolution test for the body wave inversion. The top panel shows the test input structure. The lower panel shows the result from inverting body wave data alone. The color bar represents velocity perturbation (%).

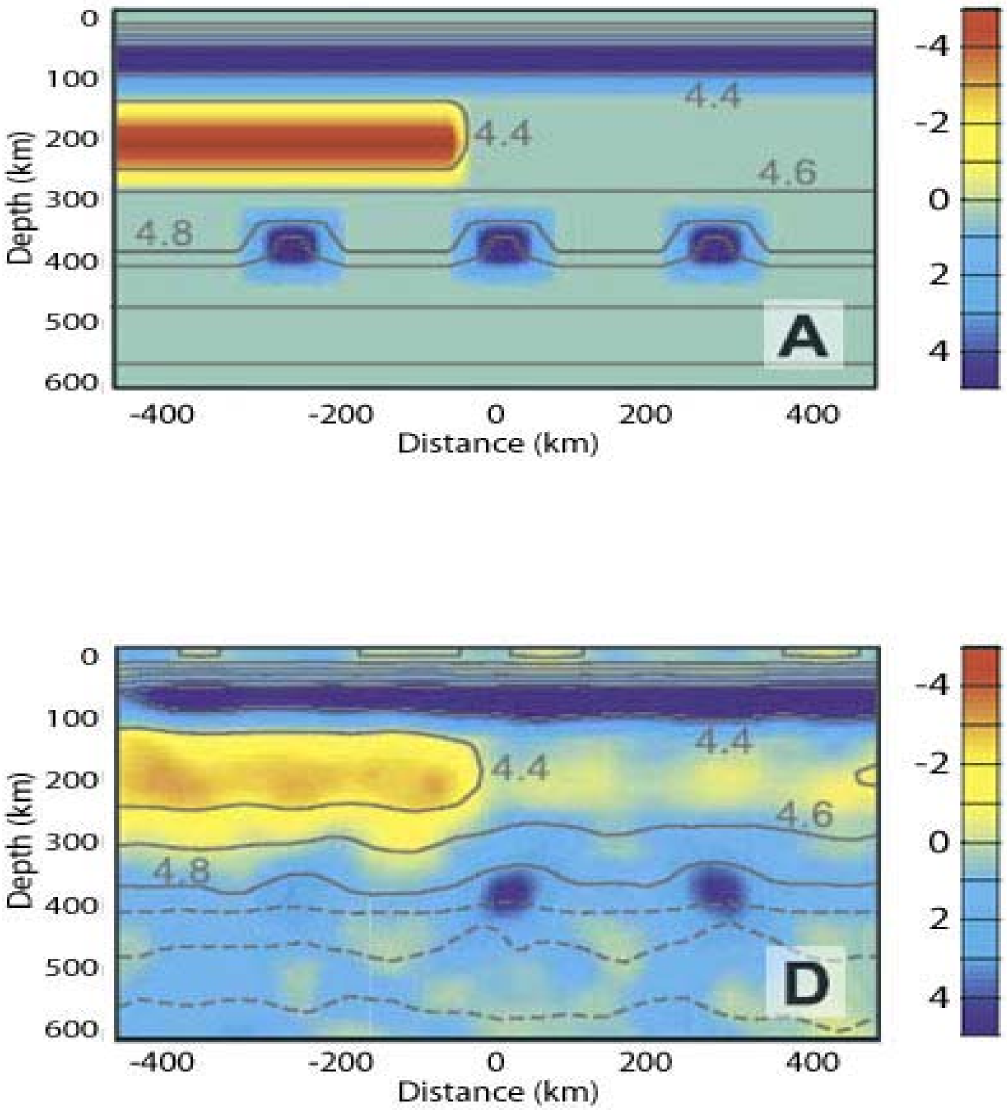

Figure 4.4 Synthetic resolution test for the body and surface wave joint inversion. The top panel shows the test input structure. The lower panel shows the result from inverting body and surface wave data together. The color bar represents velocity perturbation (%).

body wave results had simply been imposed on a 1-D structure, the low velocity channel at 200 km would have been largely missed. From these synthetic resolution tests it can be seen that the joint inversion result is obviously better than any one of independent inversion results.

4.5 Application to the La Ristra array

The La Ristra project typifies the modern dataset suited to this methodology (Figure 4.5). At 950 km in length it is wide enough for even long period surface waves to experience significant velocity variations. Since it spans the stable North American shield and the tectonic western United States (Grand, 1994; Van der Lee and Nolet, 1997), the gross structure cannot be characterized by any single 1-D velocity profile. Yet the Rio Grande rift provides a narrow target that requires the higher resolving power of body waves. While our linear array cannot constrain all aspects of anisotropy, we note that the sub-vertical S rays and Rayleigh waves respond similarly to radial anisotropy. Shear wave splitting shows a roughly uniform horizontal fast direction across the array (Gok et al., 2003) suggesting that lateral velocity variations can be largely attributed to average velocity, with minimal anisotropic effects. An explicit crust and sedimentary basin structure is included based on Wilson et al. (2003) and West et al. (2004). The body and surface wave residuals are adjusted for crustal structure, so we damp the inversion in the top 50 km and include the a priori crust is added to the final model.

Features in the surface wave image correspond closely to the Colorado Plateau, Rio Grande rift and Great Plains (Figure 4.6). No features are resolved below ~350 km. The variation across the array demonstrates the inappropriateness of any single 1-D velocity structure for the region. The body wave image is sharply defined with robust features less than 100 km in width (Figure 4.7). A clear low velocity feature is seen in the shallow mantle beneath the Rio Grande rift. It is roughly 9% slower than similar depths beneath the Great Plains. The high velocity mantle beneath the Great Plains extends to 300 km and appears to continue below 410 km into the transition zone. The shallow mantle beneath the Colorado Plateau is complex suggesting some mix of both high and low velocity regions.

The joint inversion maintains the basic features of the body wave features but with several improvements, including the addition of absolute velocity above ~350 km and more lateral continuity of features (Figure 4.8). The region beneath the Rio Grande rift is as low as 4.25 km/s, indicating solidus temperatures and the existence of partial melt (Cammarano et al. 2003). Velocities in the adjacent Colorado Plateau and Great Plains provinces reach 4.55 and 4.65 km/s, respectively—typical of cool well-developed lithosphere. Velocities beneath the Great Plains are quite high in the upper 200 km and remain elevated into the

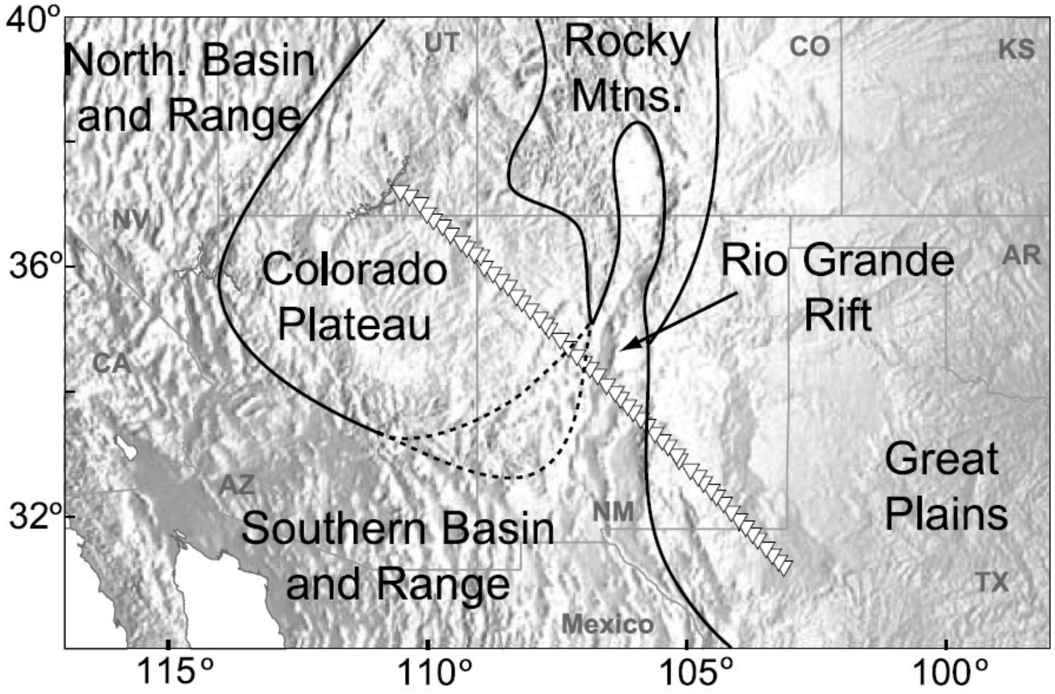

Figure 4.5 Shaded topographic map of the southwest United States. The white triangles mark stations in the La Ristra deployment. The major tectonic provinces are labeled and outlined in black.

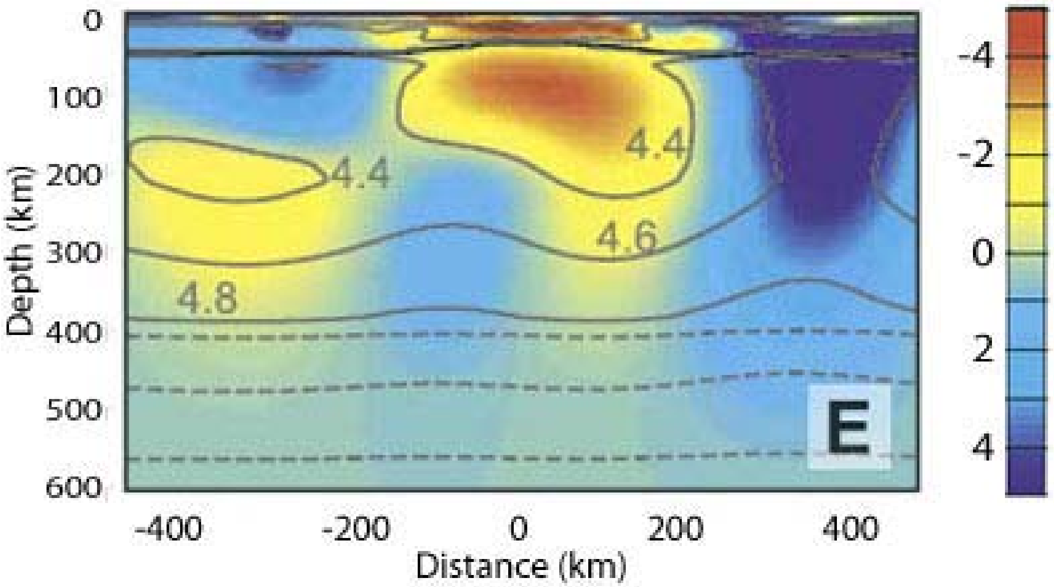

Figure 4.6 Velocity model derived from the surface wave data alone. The color bar represents velocity perturbation (%).

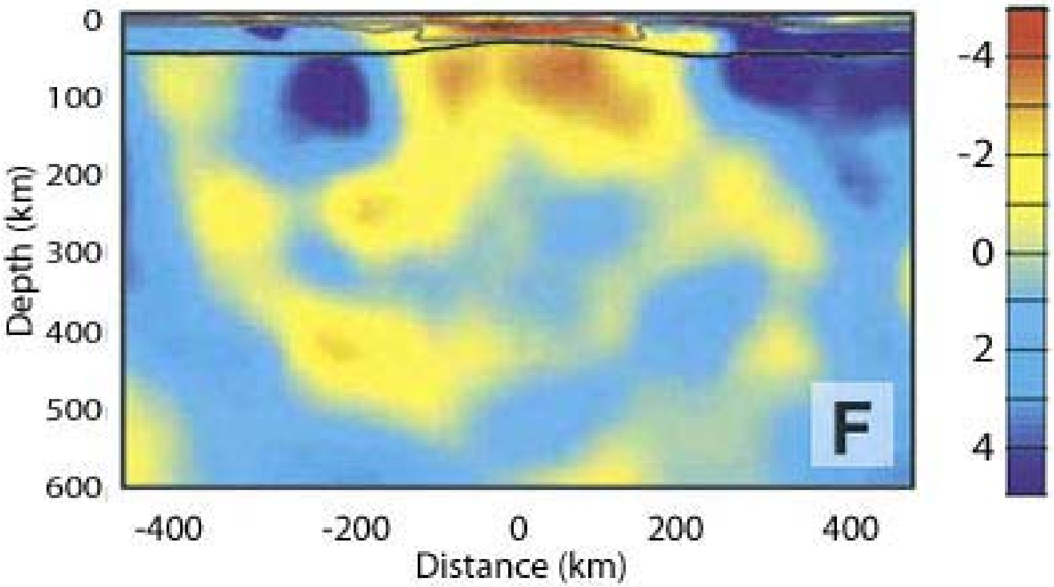

Figure 4.7 Velocity model derived from the body wave data alone. The color bar represents velocity perturbation (%).

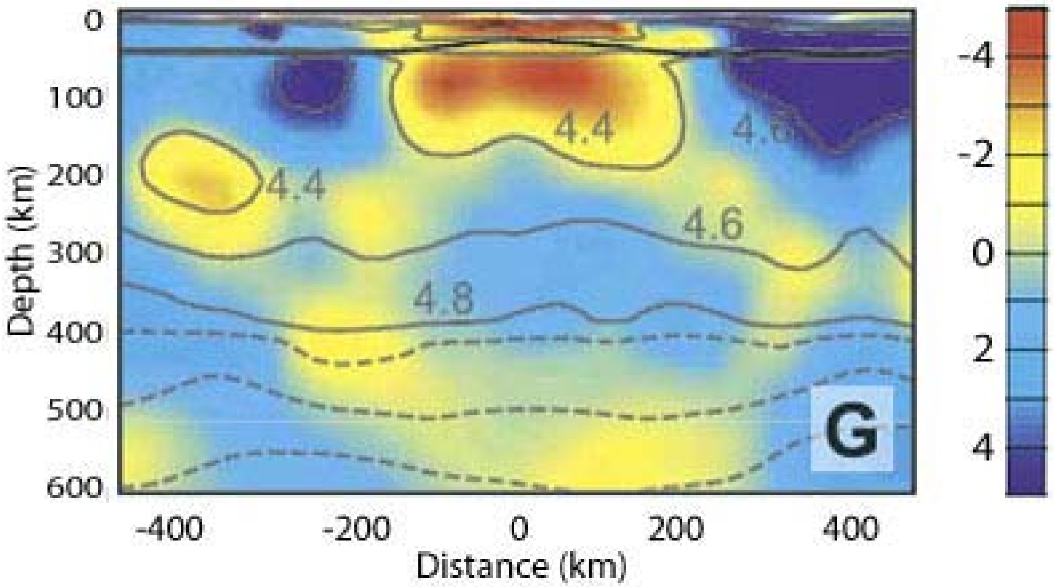

Figure 4.8 Velocity model derived from the body and surface wave data together. The color bar represents velocity perturbation (%).

transition zone. Beneath the Colorado Plateau they transition below 150 km to a region of low velocity (4.3 km/s) suggesting a warm asthenospheric channel which may help buoy the Colorado plateau at its 2 km elevation (West et al. 2004).

The lateral velocity gradients are the result of thermal variations which could drive small-scale convection. Temperature gradients, a controlling parameter for small-scale convection, are difficult to discern. While the surface waves give an indication of temperature, the model smoothness obscures the scale length of these changes. Conversely, body wave tomography reveals small-scale velocity structures, but cannot be reliably interpreted for temperature because of the non-linear velocity-temperature relationship (Karato, 1993; Cammarano et al., 2003). The joint inversion provides high resolution and absolute velocity. Extracting the necessary parameters (density, temperature and mineralogy) to make contributions to contemporary issues such as lithospheric composition and small-scale convection require both.

4.6 Conclusion

Though many techniques for regional upper-mantle scale tomography exist, most of them involve intermediate steps to extract either body wave travel time residuals or period-dependent surface wave velocities. We present a new approach that provides a simple technique for integrating these two types of measurements into a single interpretation. The technique hinges on treating surface waves as horizontally-propagating rays with deep sensitivity kernels. This formulation allows surface wave measurements to be integrated directly into existing body wave tomography inversions with modest effort.

The joint inversion of body and surface waves has two principle strengths. The first one is the combination of high resolution and absolute velocity. Absolute velocity is required, yet any regional interpretation requires good resolution as well. New seismic contributions to contemporary issues such as lithospheric composition and small-scale convection require both. The second strength of the joint inversion is the ability to provide a better-constrained picture of the upper mantle. Joint inversion provides a more accurate model than that derived from any one of the two types alone because each data type is sensitive (or, more appropriately, insensitive) to very different aspects of the mantle structure, not merely a compromise model for the two type datasets.

REFERENCES

Allen, R. M., G. Nolet, W. J. Morgan, K. Vogfjörd, B. H. Bergsson, P. Erlendsson, G. R. Foulger, S. Jakobsdóttir, B. R. Julian, M. Pritchard, S. Ragnarsson, and R. Stefánsson, 2002. Imaging the mantle beneath Iceland using integrated seismological techniques, J. Geophys. Res., 107 (12), 2325, doi:10.1029/2001JB000595.

Antolik, M., J. Gu, G. Ekstrom, and A. M. Dzeiwwonski, 2003. J362D28: A new joint model of compressional and shear velocity in the Earth's mantle, Geophys. J. Int., 153, 443-466.

Cammarano, F., S. Goes, P. Vacher, and D. Giardini, 2003. Inferring upper mantle temperatures from seismic velocities, Phys. Earth Planet. Int., 138, 197-222.

Dunn, R. A., D. R. Toomey, and S. C. Solomon, 2000. Three-dimensional seismic structure and physical properties of the crust and shallow mantle beneath the East Pacific Rise at 9 degrees 30'N, J. Geophys. Res., B, 105 (10), 23,537-23,555.

Forsyth, D. W., S. C. Webb, L. M. Dorman, and Y. Shen, 1998. Phase velocities of Rayleigh waves in the MELT Experiment on the East Pacific Rise, Science, 280, 1235-1238.

Gao, W., S. P. Grand, W. S. Baldridge, D. Wilson, M. West, J. F. Ni, and R. Aster, 2004. Upper mantle convection beneath the central Rio Grande Rift imaged by P and S wave tomography, J. Geophys. Res., 109, doi:10.1029/2003JB002743.

Gok, R., J. Ni, E. Snadvol, D. Wilson, W. S. Baldridge, R. Aster, M. West, S. Grand, W. Gao, F. Tilmann, and S. Semken, 2003. Shear wave splitting and mantle flow beneath the LA RISTRA array, Geophys. Res. Lett, 30(12), 1614, doi:10.1029/2002GL016616.

Grand, S. P., 1994. Mantle shear structure beneath the Americas and surrounding oceans, J. of Geophys. Res., 99 (6), 11,591-11,621.

James, D. E., M. J. Fouch, J. C. VanDecar, and S. Van der Lee, 2001. Tectospheric structure beneath southern Africa, Geophys. Res. Lett., 28, 2485-2488.

Karato, S., 1993. Importance of anelasticity in the interpretation of seismic tomography, Geophys. Res. Lett., 20, 1,623-1,626.

Kennett, B. L. N., E. R. Engdahl, and R. Buland, 1995. Constraints on seismic velocities in the Earth from travel times, Geophys. J. Int., 122, 108-124.

Lévêque, J. -J., and F. Masson, 1999. From ACH tomographic models to absolute velocity models, Geophys. J. Int., 137, 621-630.

Nolet, G., 1975. Higher Rayleigh modes in western Europe, Geophys. Res. Lett., 2 (2), 60-62.

Nolet, G., 1990. Partitioned waveform inversion and two-dimensional structure under the Network of Autonomously Recording Seismographs, Journal of Geophysical Research, B, Solid Earth and Planets, 95 (6), 8499-8512.

Press, W., 1992. Numerical recipes in C: the art of scientific computing, 994 pp., Cambridge University Press, Cambridge.

Spetzler, J., J. Trampert, and R. Snieder, 2002. The effect of scattering in surface wave tomography, Geophys. J. Int., 149, 755-765.

Tanimoto, T., 2003. Geometrical approach to surface wave finite frequency effects, Geophys. Res. Lett., 30(19), doi:10.1029/2003GL017475.

The MELT Seismic Team, 1998. Imaging the deep seismic structure beneath a mid-ocean ridge: the MELT experiment, Science, 280, 1215-1218.

Thurber, C., S. R. K. Roecker, M. P. L. Gold, and K. Rittger, 2003. Earthquake locations and three-dimensional fault zone structure along the creeping section of the San Andreas Fault near Parkfield, CA; preparing for SAFOD, Geophysical Res. Lett., 30, no. 3 (3), 1112, doi:10.1029/2002GL016004.

Van der Lee, S. and G. Nolet, 1997. Upper mantle S velocity structure of North America, J. Geophys. Res., 102 (10), 22,815-22,838.

Van der Lee, S., J. VanDecar, M. Fouch, and D. James, 2003. Upper mantle structure beneath southern Africa from multidisciplinary constraints, Geophys. Res. Abstr., 5, Abstract 05918.

West, M., J. Ni, W. S. Baldridge, D. Wilson, R. Aster, W. Gao, and S. Grand, 2004. Crust and upper mantle shear-wave structure of the Southwest U.S.:

implications for rifting and support for high elevation, J. Geophys. Res., 109, doi:10.1029/2003JB002575.

Wilson, D., R. Aster, W.S. Baldridge, W. Gao, R. Gok, S. Grand, J. Ni, E. Sandvol, S. Semken, and M. West, 2003. Imaging crust and upper mantle seismic structure in the southwestern United States using teleseismic receiver functions, The Leading Edge, 22 (3), 232-237.

Zhao, D., A. Hasegawa, and S. Horiuchi, 1992. Tomographic imaging of P and S wave velocity structure beneath northeastern Japan, J. Geophys. Res., 97, 19,909-19,928.

APPENDIX A

LSQR Algorithm

The LSQR method is a variant of the conjugate gradient method, but it has numerical advantages over the standard conjugate gradient method. Let us see how the method works:

Suppose we have a linear system,

$$\boldsymbol{A}\,\boldsymbol{x} = \boldsymbol{b}. \qquad \text{(A.1)}$$

where ***A*** is an *m* by *n* matrix, ***b*** is a vector of length *m*, and ***x*** is a vector of length *n* that is unkown.

We will make a lower bidiagonalized matrix that starts with vector ***b*** and transforms matrix ***A*** by iteratively choosing two orthogonal bases, [$\boldsymbol{u}_1$, $\boldsymbol{u}_2$, …] and [$\boldsymbol{v}_1$, $\boldsymbol{v}_2$, …] based on ***A*** and ***b*** in the equation (A.1)

$$\beta_1 \boldsymbol{u}_1 = \boldsymbol{b},$$

$$\alpha_1 \boldsymbol{v}_1 = \boldsymbol{A}^{\boldsymbol{T}} \boldsymbol{u}_1 \qquad \text{(A.2)}$$

$$\left.\begin{aligned} \beta_{i+1}\boldsymbol{u}_{i+1} &= \boldsymbol{A}\boldsymbol{v}_i - \alpha_i \boldsymbol{u}_i \\ \alpha_{i+1}\boldsymbol{v}_{i+1} &= \boldsymbol{A}^{\boldsymbol{T}}\boldsymbol{u}_{i+1} - \beta_{i+1}\boldsymbol{v}_{i+1} \end{aligned}\right\} \qquad \boldsymbol{i} = 1,\ 2,\ \ldots$$

where α_i and β_i are normalization parameters (constant), $\alpha_i \geq 0$ and $\beta_i \geq 0$ are chosen so that $\|\boldsymbol{u}_i\| = \|\boldsymbol{v}_i\| = 1$, $\boldsymbol{u}_i$ is an m by 1vector, and $\boldsymbol{v}_i$ is an n by 1 vector. Or rewrite them in the matrix forms by changing the sequence of the terms in (A.2)

$$\beta_1 \boldsymbol{u}_1 = \boldsymbol{b},$$

$$\boldsymbol{A}\boldsymbol{v}_i = \alpha_i \boldsymbol{u}_i + \beta_{i+1}\boldsymbol{u}_{i+1}, \quad \boldsymbol{i} = 1,2,\ldots$$

$$\begin{cases} \boldsymbol{A}^T \boldsymbol{u}_1 = \alpha_1 \boldsymbol{v}_1, \\ \boldsymbol{A}^T \boldsymbol{u}_{i+1} = \beta_{i+1}\boldsymbol{v}_{i+1} + \alpha_{i+1}\boldsymbol{v}_{i+1}, \quad \boldsymbol{i} = 1,2,\ldots \end{cases}$$

Then

$$\boldsymbol{U}_{k+1}(\beta_1 \boldsymbol{e}_1) = \boldsymbol{b}, \tag{A.3}$$

$$\boldsymbol{A}\boldsymbol{V}_k = \boldsymbol{U}_{k+1}\boldsymbol{B}_k, \tag{A.4}$$

$$\boldsymbol{A}^T\boldsymbol{U}_{k+1} = \boldsymbol{V}_k \boldsymbol{B}_k^T + \alpha_{k+1} \nu_{k+1} \boldsymbol{e}_{k+1}^T, \tag{A.5}$$

where $\boldsymbol{B}_k$ is a lower bidiagonal matrix and $\boldsymbol{U}_{k+1}$ and $\boldsymbol{V}_k$ are orthogonal

$$\boldsymbol{B}_k = \begin{bmatrix} \alpha_1 & & & & \\ \beta_2 & \alpha_2 & & & \\ & \beta_3 & \cdot & & \\ & & \cdot & \cdot & \\ & & & \cdot & \cdot \\ & & & & \cdot \quad \alpha_k \\ & & & & \beta_{k+1} \end{bmatrix},$$

$$U_{k+1} = [\, \boldsymbol{u}_1,\ \boldsymbol{u}_2,\ \ldots,\ \boldsymbol{u}_{k+1}\,],$$

$$V_k = [\, \boldsymbol{v}_1,\ \boldsymbol{v}_2,\ \ldots,\ \boldsymbol{v}_k\,],$$

$$\boldsymbol{U}_{k+1}^T \boldsymbol{U}_{k+1} = \boldsymbol{I}, \text{ and } \boldsymbol{V}_k^T \boldsymbol{V}_k = \boldsymbol{I}, \qquad (k = 1, 2, \ldots)$$

$$\boldsymbol{e}_1^T = (1, 0, 0, \ldots, 0),$$

$$\boldsymbol{e}_{k+1}^T = (0, \ldots, 0, 1, 0, \ldots, 0),$$

We then create an upper biadiagonal matrix starting with vector $\boldsymbol{A}^T \boldsymbol{b}$, that transforms $\boldsymbol{A}$ by iteratively choosing two sets of orthogonal bases vectors, $[\boldsymbol{v}_1, \boldsymbol{v}_2, \ldots]$ and $[\boldsymbol{p}_1, \boldsymbol{p}_2, \ldots]$ based on $\boldsymbol{A}$ and $\boldsymbol{b}$ in the equation (A.1)

$$\begin{aligned}
&\theta_1 \boldsymbol{v}_1 = \boldsymbol{A}^T \boldsymbol{b}, \\
&\rho_1 \boldsymbol{p}_1 = \boldsymbol{A}\boldsymbol{v}_1, \qquad\qquad (\text{A.6}) \\
&\left.\begin{aligned}
\theta_{i+1}\boldsymbol{v}_{i+1} &= \boldsymbol{A}^T \boldsymbol{p}_i - \rho_i \boldsymbol{v}_i, \\
\rho_{i+1}\boldsymbol{p}_{i+1} &= \boldsymbol{A}\boldsymbol{v}_{i+1} - \theta_{i+1}\boldsymbol{p}_i,
\end{aligned}\right\} \quad \boldsymbol{i} = 1,\ 2,\ \ldots
\end{aligned}$$

where ρ_i and θ_i are normalization parameters (constant), and $\rho_i \geq 0$ and $\theta_i \geq 0$ are chosen so that $\|\boldsymbol{p}_i\| = \|\boldsymbol{v}_i\| = 1$, and $\boldsymbol{p}_i$ is an m by 1 vector and $\boldsymbol{v}_i$ is a n by 1 vector. Or rewrite them in the matrix forms by changing the sequence of the terms in (A.6)

$$\theta_1 \boldsymbol{v}_1 = \boldsymbol{A}^T \boldsymbol{b},$$

$$\begin{cases} \boldsymbol{A}\boldsymbol{v}_1 = \rho_1 \boldsymbol{p}_1, \\ \boldsymbol{A}\boldsymbol{v}_{i+1} = \theta_{i+1}\boldsymbol{p}_i + \rho_{i+1}\boldsymbol{p}_{i+1}, \quad \boldsymbol{i} = 1,2,\ldots \end{cases}$$

$$\boldsymbol{A}^T \boldsymbol{p}_i = \rho_i \boldsymbol{v}_i + \theta_{i+1}\boldsymbol{v}_{i+1}, \qquad \boldsymbol{i} = 1,2,\ldots$$

Then

$$\boldsymbol{V}_k(\theta_1 \boldsymbol{e}_1) = \boldsymbol{A}^T \boldsymbol{b}, \qquad \text{(A.7)}$$

$$\boldsymbol{A}\boldsymbol{V}_k = \boldsymbol{P}_k \boldsymbol{R}_k, \qquad \text{(A.8)}$$

$$\boldsymbol{A}^T \boldsymbol{P}_k = \boldsymbol{V}_k \boldsymbol{R}_k^T + \theta_{k+1} \boldsymbol{v}_{k+1} \boldsymbol{e}_k^T, \qquad \text{(A.9)}$$

where $\boldsymbol{R}_k$ is an upper bidiagonal matrix, $\boldsymbol{P}_k$ are orthogonal and $\boldsymbol{V}_k$ are the same as that in the lower bidiagonalization

$$\boldsymbol{R}_k = \begin{bmatrix} \rho_1 & \theta_2 & & & \\ & \rho_2 & \theta_3 & & \\ & & \ddots & \ddots & \\ & & & \rho_{k-1} & \theta_k \\ & & & & \rho_k \end{bmatrix},$$

$$\boldsymbol{P}_k = [\, \boldsymbol{p}_1, \boldsymbol{p}_2, \ldots, \boldsymbol{p}_k \,],$$

$$\boldsymbol{V}_k = [\, \boldsymbol{v}_1, \boldsymbol{v}_2, \ldots, \boldsymbol{v}_k \,],$$

$$\boldsymbol{P}_k^T \boldsymbol{P}_k = \boldsymbol{I}, \text{ and } \boldsymbol{V}_k^T \boldsymbol{V}_k = \boldsymbol{I}, \qquad (k = 1, 2, \ldots).$$

$\boldsymbol{e}_1^T = (1, 0, \dots, 0),$

$\mathbf{e}_k^T = (0, \dots, 0, 1, 0, .., 0),$

Using equations (A.4) and (A.8) we have

$$\boldsymbol{B}_k^T \boldsymbol{B}_k = \boldsymbol{R}_k^T \boldsymbol{R}_k, \qquad (\text{A.10})$$

and $\boldsymbol{R_k}$ can be obtained from the QR factorization* of $\boldsymbol{B_k}$

$$\boldsymbol{Q}_k \boldsymbol{B}_k = \begin{bmatrix} \boldsymbol{R_k} \\ \boldsymbol{O} \end{bmatrix} . \qquad (\text{A.11})$$

where $\boldsymbol{Q}_k$ is an orthogonal matrix, $\boldsymbol{Q}_k{}^T \boldsymbol{Q}_k = \boldsymbol{I}$. The connection (A.11) is the key relation, which gives the main meaning of the LSQR algorithm. Also the relations below hold:

$$\boldsymbol{U}_{k+1} = [\ \boldsymbol{U}_k, \boldsymbol{u}_{k+1}\ ] = [\ \boldsymbol{P_k}, \boldsymbol{r}_k / \|\ \boldsymbol{r}_k\ \|\ ]\ \boldsymbol{Q}_k, \qquad (\text{A.12})$$

for some vector $\boldsymbol{r_k}$. From equation (A.10), we also have the identities

$$\alpha_1^2 + \beta_2^2 = \rho_1^2,\ \alpha_1 \beta_1 = \theta_1,$$

$$\alpha_i^2 + \beta_{i+1}^2 = \rho_i^2 + \theta_i^2, \qquad (\text{A.13})$$

$$\alpha_i \beta_i = \rho_{i-1} \theta_i, \qquad (\text{ for } i > 1).$$

In terms of the quantities generated from $\boldsymbol{A}$ and $\boldsymbol{b}$ by the bidiagonalizations we can change the least-squares problem, min $\|\ \boldsymbol{b} - \boldsymbol{A}\ \boldsymbol{x}\ \|$ into another equivalent form.

Let the quantities

$$\boldsymbol{x}_k = \boldsymbol{V}_k \boldsymbol{y}_k, \qquad (\text{A.14})$$

$$\boldsymbol{r}_k = \boldsymbol{b} - \boldsymbol{A}\,\boldsymbol{x}_k, \qquad \text{(A.15)}$$

$$\boldsymbol{t}_{k+1} = \beta_1 \boldsymbol{e}_1 - \boldsymbol{B}_k \boldsymbol{y}_k\,, \qquad \text{(A.16)}$$

be defined in terms of some vector $\boldsymbol{y}_k$. Based on the equations (A.3) and (A.4) that the equation

$$\boldsymbol{r}_k = \boldsymbol{U}_{k+1}\,\boldsymbol{t}_{k+1}\,. \qquad \text{(A.17)}$$

holds. Because we want $\| \boldsymbol{r}_k \|$ to be small, and $\boldsymbol{U}_{k+1}$ is bounded and orthogonal, this immediately suggests choosing $\boldsymbol{y}_k$ to minimize $\| \boldsymbol{t}_{k+1} \|$. Hence we are naturally led to the least-squares problem

$$min \, \| \, \beta_1 \boldsymbol{e}_1 - \boldsymbol{B}_k\, \boldsymbol{y}_k \, \| \,. \qquad \text{(A.18)}$$

which forms the basis for LSQR.

The algorithm based on the upper bidiagonalization is the least squares conjugate gradient method (Paige, 1974), the algorithm is defined by the equations

$$\boldsymbol{x}_k = \boldsymbol{V}_k\, \boldsymbol{y}_k, \qquad \text{(A.19)}$$

$$\boldsymbol{R}_k^T \boldsymbol{R}_k \boldsymbol{y}_k = \theta_1 \boldsymbol{e}_1, \qquad \text{(A.20)}$$

$$\boldsymbol{R}_k^T \boldsymbol{f}_k = \theta_1 \boldsymbol{e}_1, \qquad \text{(A.21)}$$

$$\boldsymbol{x}_k = \boldsymbol{V}_k\, \boldsymbol{R}_k^{-1} \boldsymbol{f}_k\,, \qquad \text{(A.22)}$$

In this solving procedure, it is effectively solving the least-squares problem, min$\| \, \beta_1 \boldsymbol{e}_1 - \boldsymbol{B}_k\, \boldsymbol{y}_k \, \|$ by using the corresponding normal equations. But the LSQR algorithm based on the equation:

$$\boldsymbol{B}_k^T \boldsymbol{B}_k \boldsymbol{y}_k = \boldsymbol{B}_k^T \beta_1 \boldsymbol{e}_1 = \alpha_1 \beta_1 \boldsymbol{e}_1, \qquad (\text{A.23})$$

Using the relations between the two bidiagonalized matrices, equations (A.10) and (A.12), it is equivalent to the equation, $\boldsymbol{R}_k^T \boldsymbol{R}_k \boldsymbol{y}_k = \theta_1 \boldsymbol{e}_1$.

Computationally, to find min $\| \beta_1 \boldsymbol{e}_1 - \boldsymbol{B}_k \boldsymbol{y}_k \|$ the standard QR factorization of $\boldsymbol{B}_k$ is used, that is, the same factorization as in (A.10) that links the two bidiagonalized matricess. This takes the form

$$\boldsymbol{Q}_k [\, \boldsymbol{B}_k \;\; \beta_1 \boldsymbol{e}_1 \,] = \begin{bmatrix} \boldsymbol{R}_k & \boldsymbol{f}_k \\ & \bar{\boldsymbol{\phi}}_{k+1} \end{bmatrix}$$

$$= \begin{bmatrix} \rho_1 & \theta_2 & & & & & \phi_1 \\ & \rho_2 & \theta_3 & & & & \phi_2 \\ & & \cdot & \cdot & & & \cdot \\ & & & \cdot & \cdot & & \cdot \\ & & & & \cdot & \cdot & \cdot \\ & & & & \rho_{k-1} & \theta_k & \phi_{k-1} \\ & & & & & \rho_k & \phi_k \\ & & & & & & \bar{\phi}_{k+1} \end{bmatrix}. \qquad (\text{A.24})$$

where $\boldsymbol{Q}_k \equiv \boldsymbol{Q}_{k,k+1} \ldots \boldsymbol{Q}_{2,3} \boldsymbol{Q}_{1,2}$ is a product of plane rotations designed to eliminate the subdiagonals β_2, β_3, …of $\boldsymbol{B}_k$. The vectors $\boldsymbol{y}_k$ and $\boldsymbol{t}_{k+1}$ could then be found from

$$\boldsymbol{R}_k \boldsymbol{y}_k = \boldsymbol{f}_k, \qquad (\text{A.25})$$

$$\boldsymbol{t}_{k+1} = \boldsymbol{Q}_k^T \begin{bmatrix} \boldsymbol{O} \\ \bar{\boldsymbol{\phi}}_{k+1} \end{bmatrix}. \qquad (\text{A.26})$$

$$\boldsymbol{x}_k = \boldsymbol{V}_k \boldsymbol{R}_k^{-1} \boldsymbol{f}_k \equiv \boldsymbol{D}_k \boldsymbol{f}_k, \qquad (\text{A.27})$$

where $\boldsymbol{D}_k \equiv [\, \boldsymbol{d}_1, \ \boldsymbol{d}_2, \dots, \boldsymbol{d}_k \,]$.

$$\boldsymbol{R}_k^T \ \boldsymbol{D}_k^T = \boldsymbol{V}_k^T, \qquad (\text{A.28})$$

$$\boldsymbol{d}_0 = \boldsymbol{0}\,, \quad \boldsymbol{x}_0 = \boldsymbol{0}\,, \qquad (\text{A.29})$$

$$\boldsymbol{d}_k = (\ 1/\rho_k\ )(\ \boldsymbol{v}_k - \theta_k\, \boldsymbol{d}_{k-1}\ )\,, \qquad (\text{A.30})$$

$$\boldsymbol{x}_k = \boldsymbol{x}_{k-1} + \phi_k\, \boldsymbol{d}_k\,. \qquad (\text{A.31})$$

The above description gives the outline of algorithm LSQR.

[*] QR factorization

Given an m by n matrix $\boldsymbol{A}$, with $m \geq n$, we seek an m by m orthogonal matrix $\boldsymbol{Q}$ such that

$$\boldsymbol{A} = \boldsymbol{Q}\begin{bmatrix} \boldsymbol{R} \\ \boldsymbol{O} \end{bmatrix}$$

where $\boldsymbol{R}$ is n by n and upper triangular. Such a QR factorization transforms (Heath, 1997) the linear least squares problem $\boldsymbol{Ax} \approx \boldsymbol{b}$ into a triangular least squares problem having the same solution because

$$\|\boldsymbol{b}\text{-}\boldsymbol{Ax}\|_2 = \|\ \boldsymbol{b}\text{-}\boldsymbol{Q}[\begin{bmatrix} \boldsymbol{R} \\ \boldsymbol{O} \end{bmatrix}\boldsymbol{x}\|_2 = \|\boldsymbol{Q}^T\boldsymbol{b}\text{-}\begin{bmatrix} \boldsymbol{R} \\ \boldsymbol{O} \end{bmatrix}^T\boldsymbol{x}\|_2.$$

REFERENCES

Michael T. Heath, 1997. Scientific Computing: An introductory Survey, WCB /McGraw-Hill.

Paige, C. C., and M. A. Saunders, 1982. LSQR: An algorithm for sparse linear equations and sparse least squares, ACM Transactions on Mathematical Software, 8, 43-71.

Paige, C. C., 1974. Bidiagonallization of matrices and solution of linear equations, SIAM J. Numer. Anal. 11, 197-209.

APPENDIX B

Sparse matrix technique

Suppose the matrix $\boldsymbol{A}$ in linear system $\boldsymbol{A}\,\boldsymbol{x} = \boldsymbol{b}$ is a m by n matrix with few non-zero elements. In solving linear system only $\boldsymbol{A}\,\boldsymbol{x}$ and $\boldsymbol{A}^T\boldsymbol{y}$ need calculation by the LSQR and SIRT algorithms, so we want to use several small matrices to represent the non-zero elements in matrix $\boldsymbol{A}$ that save disk space, i.e., the sparse matrix technique. The sparse matrix technique makes calculations on $\boldsymbol{A}\,\boldsymbol{x}$ and $\boldsymbol{A}^T\boldsymbol{y}$ easy and saves time and memory on computer. In matrix $\boldsymbol{A}$

$$\boldsymbol{A} = \begin{bmatrix} a_{1,1} & a_{1,2} & \cdot & \cdot & \cdot & \cdot & \cdot & \cdot & a_{1,n} \\ a_{2,1} & a_{2,2} & \cdot & \cdot & \cdot & \cdot & \cdot & \cdot & a_{2,n} \\ \cdot & \cdot & & & & & & & \cdot \\ \cdot & \cdot & & & & & & & \cdot \\ \cdot & \cdot & & & & & & & \cdot \\ \cdot & \cdot & & & & & & & \cdot \\ \cdot & \cdot & & & & & & & \cdot \\ \cdot & \cdot & & & & & & & \cdot \\ \cdot & \cdot & & & & & & & \cdot \\ \cdot & \cdot & & & & & & & \cdot \\ \cdot & \cdot & & & & & & & \cdot \\ a_{m,1} & a_{m,2} & \cdot & \cdot & \cdot & \cdot & \cdot & \cdot & a_{m,n} \end{bmatrix} \qquad (\text{B.1})$$

here are non-zero elements, a_{1,i_1}, a_{1,i_2}, …, a_{1,i_l}, a_{2,j_1}, a_{2,j_2}, …, a_{2,j_m}, …, a_{m,k_1}, a_{m,k_2}, …, a_{m,k_n}, and n_1 is the number of non-zero elements in first row, i_1, i_2, …,

i_l are their subscripts of the column, n_2 is the number of non-zero elements in second row, $j_1, j_2, \ldots, j_m$ are their subscripts of the column, ……, n_m is the number of non-zero elements in mth row, $k_1, k_2, \ldots, k_n$ are their subscripts of the column. We use three matrices to express the non-zero elements in matrix $\boldsymbol{A}$ below

$$\boldsymbol{a} = [\, a_{1,i_1}, a_{1,i_2}, \ldots, a_{1,i_l}, a_{2,j_1}, a_{2,j_2}, \ldots, a_{2,j_m}, \ldots, a_{m,k_1}, a_{m,k_2}, \ldots, a_{m,k_n} \,]$$

$$\equiv [\, a_1, a_2, \ldots, a_{n_1}, a_{n_1+1}, a_{n_1+2}, \ldots, a_{n_1+n_2}, \ldots\ldots, a_{(\sum_{k=1}^{m-1} n_k)+1}, a_{(\sum_{k=1}^{m-1} n_k)+2}, \ldots, a_{\sum_{k=1}^{m} n_k} \,] \qquad (\text{B.2})$$

$$\boldsymbol{c} = [i_1, i_2, \ldots, i_l, j_1, j_2, \ldots, j_m, \ldots\ldots, k_1, k_2, \ldots, k_n]$$

$$\equiv [\, c_1, c_2, \ldots, c_{n_1}, c_{n_1+1}, c_{n_1+2}, \ldots, c_{n_1+n_2}, \ldots\ldots, c_{(\sum_{k=1}^{m-1} n_k)+1}, c_{(\sum_{k=1}^{m-1} n_k)+2}, \ldots, c_{\sum_{k=1}^{m} n_k} \,]$$

$$\boldsymbol{n} = [\, n_1, n_2, \ldots\ldots, n_m \,]$$

and

$$\boldsymbol{x} = [\, x_1, x_2, \ldots\ldots, x_n \,]^T$$

$$\boldsymbol{y} = [\, y_1, y_2, \ldots\ldots, y_m \,]^T$$

let us express $\boldsymbol{A}\,\boldsymbol{x}$ by $\boldsymbol{a}$, $\boldsymbol{c}$, $\boldsymbol{n}$ and $\boldsymbol{x}$

$$\boldsymbol{A}\,\boldsymbol{x} = \begin{bmatrix} a_{1,1} & a_{1,2} & \cdot\ \cdot\ \cdot\ \cdot\ \cdot\ \cdot\ \cdot & a_{1,n} \\ a_{2,1} & a_{2,2} & \cdot\ \cdot\ \cdot\ \cdot\ \cdot\ \cdot\ \cdot & a_{2,n} \\ \cdot & \cdot & & \cdot \\ \cdot & \cdot & & \cdot \\ \cdot & \cdot & & \cdot \\ \cdot & \cdot & & \cdot \\ \cdot & \cdot & & \cdot \\ \cdot & \cdot & & \cdot \\ \cdot & \cdot & & \cdot \\ \cdot & \cdot & & \cdot \\ \cdot & \cdot & & \cdot \\ a_{m,1} & a_{m,2} & \cdot\ \cdot\ \cdot\ \cdot\ \cdot\ \cdot\ \cdot & a_{m,n} \end{bmatrix} \begin{bmatrix} x_1 \\ x_2 \\ \cdot \\ \cdot \\ \cdot \\ \cdot \\ \cdot \\ \cdot \\ \cdot \\ \cdot \\ \cdot \\ x_n \end{bmatrix}$$

$$\boldsymbol{A}\,\boldsymbol{x} = \begin{bmatrix} a_{1,i_1} x_{i_1} + a_{1,i_2} x_{i_2} + \ldots + a_{1,i_l} x_{i_l} \\ a_{2,j_1} x_{j_1} + a_{2,j_2} x_{j_2} + \ldots + a_{2,j_m} x_{j_m} \\ \cdot \\ \cdot \\ \cdot \\ \cdot \\ \cdot \\ \cdot \\ \cdot \\ \cdot \\ \cdot \\ a_{m,k_1} x_{k_1} + a_{m,k_2} x_{k_2} + \ldots + a_{m,k_n} x_{k_n} \end{bmatrix}$$

$$\boldsymbol{A}\,\boldsymbol{x} = \begin{bmatrix} a_{c_1} x_{c_1} + a_{c_2} x_{c_2} + \ldots + a_{c_{n_1}} x_{c_{n_1}} \\ a_{c_{n_1+1}} x_{c_{n_1+1}} + a_{c_{n_1+2}} x_{c_{n_1+2}} + \ldots + a_{c_{n_1+n_2}} x_{c_{n_1+n_2}} \\ . \\ . \\ . \\ . \\ . \\ . \\ . \\ . \\ . \\ a_{c_{(\sum_{k=1}^{m-1} n_k)+1}} x_{c_{(\sum_{k=1}^{m-1} n_k)+1}} + a_{c_{(\sum_{k=1}^{m-1} n_k)+2}} x_{c_{(\sum_{k=1}^{m-1} n_k)+2}} + \ldots + a_{c_{\sum_{k=1}^{m} n_k}} x_{c_{\sum_{k=1}^{m} n_k}} \end{bmatrix}$$

$$= \begin{bmatrix} \sum_{k=1}^{n_1} a_{c_k} x_{c_k} \\ \sum_{k=n_1+1}^{n_1+n_2} a_{c_k} x_{c_k} \\ . \\ . \\ . \\ . \\ . \\ . \\ . \\ . \\ . \\ \sum_{k=(\sum_{k=1}^{m-1} n_k)+1}^{\sum_{k=1}^{m} n_k} a_{c_k} x_{c_k} \end{bmatrix} \qquad \text{(B.3)}$$

Like this above procedure, we can use the sparse matrix technique to easily calculate $\boldsymbol{A}^T \boldsymbol{y}$.

$$\boldsymbol{x} = \boldsymbol{A}^T \boldsymbol{y} = \begin{bmatrix} a_{1,1} & a_{2,1} & \cdot & \cdot & \cdot & \cdot & \cdot & \cdot & \cdot & \cdot & \cdot & a_{m,1} \\ a_{1,2} & a_{2,2} & \cdot & \cdot & \cdot & \cdot & \cdot & \cdot & \cdot & \cdot & \cdot & a_{m,2} \\ \cdot & \cdot & & & & & & & & & & \cdot \\ \cdot & \cdot & & & & & & & & & & \cdot \\ \cdot & \cdot & & & & & & & & & & \cdot \\ \cdot & \cdot & & & & & & & & & & \cdot \\ \cdot & \cdot & & & & & & & & & & \cdot \\ \cdot & \cdot & & & & & & & & & & \cdot \\ a_{1,n} & a_{2,n} & \cdot & \cdot & \cdot & \cdot & \cdot & \cdot & \cdot & \cdot & \cdot & a_{m,n} \end{bmatrix} \begin{bmatrix} y_1 \\ y_2 \\ \cdot \\ \cdot \\ \cdot \\ \cdot \\ \cdot \\ \cdot \\ y_m \end{bmatrix} \qquad (\text{B.4})$$

the calculation of $\boldsymbol{A}^T \boldsymbol{y}$ is not obvious, let us find that below. All non-zero product items are given below using $\boldsymbol{a}$, $\boldsymbol{c}$, and $\boldsymbol{n}$:

$x_1(c_1) = a_1 y_1, \quad x_1(c_2) = a_2 y_1 \quad , \ldots, \quad x_1(c_{n_1}) = a_{n_1} y_1 ,$

$x_2(c_{n_1+1}) = a_{n_1+1} y_2, \quad x_2(c_{n_1+2}) = a_{n_1+2} y_2 , \ldots, \quad x_2(c_{n_1+n_2}) = a_{n_1+n_2} y_2,$

……

$x_m(c_{(\sum_{k=1}^{m-1} n_k)+1}) = a_{c_{(\sum_{k=1}^{m-1} n_k)+1}} y_m, \quad x_m(c_{(\sum_{k=1}^{m-1} n_k)+2}) = a_{c_{(\sum_{k=1}^{m-1} n_k)+2}} y_m , \ldots,$

$x_m(c_{\sum_{k=1}^{m} n_k}) = a_{c_{\sum_{k=1}^{m} n_k}} y_m,$

let $m_1, m_2, \ldots, m_l, \ldots, m_{max}$ express a sequence from minimum to maximum

$m_1 = min(c_1, \ldots, c_{\sum_{k=1}^{m} n_k}),$

$m_2 = min(c_1,, \ldots, c_{\sum_{k=1}^{m} n_k} \mid except\ m_1)$

……

$m_l = min(c_1,, \ldots, c_{\sum_{k=1}^{m} n_k} \mid except\ m_1, m_2, \ldots, and\ m_{l-1})$

……

$m_{max} = max(c_1, \ldots, c_{\sum_{k=1}^{m} n_k}),$

combinating same subscripts items

$x(m_1) = \sum_{l=1}^{m} x_l(m_1),$

$x(m_2) = \sum_{l=1}^{m} x_l(m_2),$

……

$x(m_l) = \sum_{l=1}^{m} x_l(m_l),$

……

$x(m_{max}) = \sum_{l=1}^{m} x_l(m_{\max}),$

finally $\boldsymbol{x} = \boldsymbol{A}^T \boldsymbol{y}$

$$\boldsymbol{x} = [\quad \cdots \quad x(m_1) \quad \cdots \quad x(m_2) \quad \cdots \quad x(m_l) \quad \cdots \quad \cdots \quad x(m_{\max}) \quad \cdots \quad]^T \quad (\text{B.5})$$

note: other elements in (B.5) are zero except $x(m_k)$.

APPENDIX C

Conjugate Gradient Algorithm

The conjugate gradient method is a method to find the extreme value of a function. If solving linear equation can be changed into an equivalent problem of finding extreme value of a function, the conjugate gradient method can be used in solving linear equations.

Suppose matrix $\boldsymbol{A}$ in a linear equation system, $\boldsymbol{A}\,\boldsymbol{x} = \boldsymbol{b},$ is symmetric and positive definite, let us consider optimization problem of the quadratic function

$$\boldsymbol{F}(\,\boldsymbol{x}\,) = \frac{1}{2}(\,\boldsymbol{A}\,\boldsymbol{x}, \boldsymbol{x}\,) - (\,\boldsymbol{b}, \boldsymbol{x}\,), \qquad (\text{ C.1 })$$

A theorem states that if $\boldsymbol{A}$ is symmetric and positive definite, then vector $\boldsymbol{x}^*$ is the solution of the linear equation $\boldsymbol{A}\,\boldsymbol{x} = \boldsymbol{b}$ if and only if $\boldsymbol{x}^*$ is the minimum point of $\boldsymbol{F}(\,\boldsymbol{x}\,)$ in (C.1). When $\boldsymbol{A}$ is an n by n symmetric and positive definite matrix, $\boldsymbol{x}$ and $\boldsymbol{y}$ are two vectors in $\boldsymbol{R}^n$ space, if $(\,\boldsymbol{A}\,\boldsymbol{x}, \boldsymbol{y}\,) = (\,\boldsymbol{x}, \boldsymbol{A}\,\boldsymbol{y}\,) = 0$, we call that $\boldsymbol{x}$ and $\boldsymbol{y}$ are $\boldsymbol{A}$-conjugate, and $\boldsymbol{x}$ and $\boldsymbol{y}$ are $\boldsymbol{I}$-conjugate if $\boldsymbol{x}$ and $\boldsymbol{y}$ are orthogonal each other.

The conjugate gradient method means that each modified direction is conjugate with the pre-modified directions for each iteration, i.e.

$$(\,\boldsymbol{p}^{(i)},\ \boldsymbol{A}\,\boldsymbol{p}^{(j)}\,) = 0 \quad (i,\ j = 0, 1,\ \ldots,\ n,\ and\ if\ i \neq j), \qquad (\text{ C.2 })$$

The process of finding the solution by the conjugate gradient method is given below

$$\boldsymbol{p}^{(0)} = \boldsymbol{r}^{(0)} = \boldsymbol{b} - \boldsymbol{A}\,\boldsymbol{x}^{(0)}, \tag{C.3}$$

$$\alpha_k = (\,\boldsymbol{r}^{(k)}, \boldsymbol{r}^{(k)}\,)/(\,\boldsymbol{p}^{(k)},\ \boldsymbol{A}\,\boldsymbol{p}^{(k)}\,), \tag{C.4}$$

$$\boldsymbol{x}^{(k+1)} = \boldsymbol{x}^{(k)} + \alpha_k\,\boldsymbol{p}^{(k)}, \tag{C.5}$$

$$\boldsymbol{r}^{(k+1)} = \boldsymbol{b} - \boldsymbol{A}\,\boldsymbol{x}^{(k+1)}, = \boldsymbol{r}^{(k)} + \alpha_k\,\boldsymbol{A}\boldsymbol{p}^{(k)}, \tag{C.6}$$

$$\beta_{k+1} = (\,\boldsymbol{r}^{(k+1)}, \boldsymbol{r}^{(k+1)}\,)/(\,\boldsymbol{r}^{(k)},\ \boldsymbol{r}^{(k)}\,), \tag{C.7}$$

$$\boldsymbol{p}^{(k+1)} = \boldsymbol{r}^{(k+1)} + \beta_k\,\boldsymbol{p}^{(k)}, \tag{C.8}$$

Theoretically, we can find the solution in n steps or less if there are no rounding off errors and machine errors.

In the linear system in tomographic inversions, $\boldsymbol{A}\,\boldsymbol{x} = \boldsymbol{b}$, generally, matrix $\boldsymbol{A}$ is an m by n ($m \geq n$) matrix and it is ill-conditional and vector $\boldsymbol{b}$ is noisy. If we want to apply the standard conjugate gradient method to find solution $\boldsymbol{x}$ in a least-squares sense, the equation, $\boldsymbol{A}\ \boldsymbol{x} = \boldsymbol{b}$, needs to be changed into the normal equations, $\boldsymbol{A}^T\boldsymbol{A}\,\boldsymbol{x} = \boldsymbol{A}^T\boldsymbol{b}$.

REFERENCES

Abers, G. A., 2000. Hydrated subducted crust at 100-250 km depth, Earth and Planet. Sci. Lett., 176, 323-330.

Aki, K., A. Christofferson, and E. S. Husebye, 1977. Determination of the three-dimensional seismic structure of the lithosphere, J. Geophys. Res., 82, 277-296.

Allen, R. M., G. Nolet, W. J. Morgan, K. Vogfjörd, B. H. Bergsson, P. Erlendsson, G. R. Foulger, S. Jakobsdóttir, B. R. Julian, M. Pritchard, S. Ragnarsson, and R. Stefánsson, 2002. Imaging the mantle beneath Iceland using integrated seismological techniques, J. Geophys. Res., 107 (12), 2325, doi:10.1029/2001JB000595.

Antolik, M., J. Gu, G. Ekstrom, and A. M. Dzeiwwonski, 2003. J362D28: A new joint model of compressional and shear velocity in the Earth's mantle, Geophys. J. Int., 153, 443-466.

Atwater, T., 1970. Implications of plate tectonics for the Cenozoic tectonic evolution of western North America, Geol. Soc. Am. Bull. 81, 3,513-3,536.

Axelrod, D. I. And H. P. Bailey, 1976. Tertiary vegetation, climate and altitude of the Rio Grande depression, New Mexico-Colorado, Paleobiology, 2, 235-254.

Baldridge, W. S., F. V. Perry, D. T. Vaniman, L. D. Nealey, B. D. Leavy, A. W. Laughlin, P. R. Kyle, Y. Bartov, G. Steintz, and E. S. Gladney, 1991. Middle to late Cenozoic magmatism of the southeastern Colorado Plateau and central Rio Grande Rift (New Mexico and Arizona, U. S. A.); a model for continental rifting, Tectonophysics, 197,327-354.

Bass, J. D. and D. L. Anderson, 1984. Composition of the upper mantle: Geophysical tests of two petrological models, Geophys. Res. Leett., 11, 237-240.

Beghoul, N., M. Barazangi and B. L. Isacks, 1993. Lithospheric structure of Tibet and western North America: Mechanisms of uplift and a comparative study, J. Geophys. Res., 98, 1,997-2,016.

Bercovici, D. and S. Karato, 2003. Whole mantle convection and the transition zone water filter, Nature, 425, 39-44.

Bina, C. R. and B. J., Wood, 1984. The eclogite to garnetite transition: experimental and thermodynamic constraints, Geophys. Res. Lett., 11, 955-958.

Bina, C. R. and B. J., Wood, 1987. Olivine-spinel transitions: experimental and thermodynamic constraints for the nature of the 410 km seismic ddiscontinuity. J. Geophys. Res., 92, 4,853-4,866.

Bina, C. R. and G. Helffrich, 1994. Phase transition Claperon slopes and transition zone seismic discontinuity topography, J. Geophys. Res., 99 (B8), 15,853-15,860.

Bina, C. R., 1993. Mutually consistent estimates of upper mantle composition from seismic contrasts at 400 km depth, Pure Appl. Geophys., 141, 101-109.

Bird, P., 1984. Laramide crustal thickening event in the rocky mountain foreland and great plains, Tectonics, 3, 741-758.

Bird, P., 1988. Formation of the Rocky Mountains, western United States: A continuum computer model, Science, 239, 1,501-1,507.

Buck, W. R., 1986. Small-scale convection induced by passive rifting: the cause for uplift of rift shoulders, Earth and Planet. Sci. Lett., 77, 362-372.

Brudzinski, M. R., W.-P. Chen, R. L. Nowack, and B.-S. Huang, 1997. Variations of P wave speeds in the mantle transition zone beneath the northern Philippine Sea, J. Geophys. Res., 102, 11,815-11,827.

Brudzinski, M. R. and W.-P. Chen, 2003. A Petrologic Anomaly Accompanying Outboard Earthquakes Beneath Figi-Tonga: Corresponding Evidence from Broadband P and S Waveforms, Journal of Geophysical Research, 108, B6, 2299, doi:10.1029/2002JB002012.

Cammarano, F., S. Goes, P. Vacher, and D. Giardini, 2003. Inferring upper mantle temperatures from seismic velocities, Phys. Earth Planet. Int., 138, 197-222.

Cammarano, F., S. Goes, A. Deuss, and D. Giardini, 2005a. Is a pyrolite mantle compatible with seismic data? Earth Planet. Sci. Lett., 232, 227-243.

Cammarano, F., A. Deuss, S. Goes, and D. Giardini, 2005b. One-dimensional physical models for the upper mantle and transition zone: Combining seismic and mineral physicas constraints, J. Geophys. Res., 110, B01306, doi:10.1029/2004JB003272.

Cather, S. M., R. M. Chamberlin, C. E. Chapin, and W. C. McIntosh, 1994. Straigraphic consequences of episodic extension in the Lemitar Mountains, central Rio Grande rift, in Keller, G. R. and Cather, S. M. eds., Basins of the Rio Grande rift: structure, stratigraphy, and tectonics setting, Geol. Soc. Am. Special Paper, 291, 157-170.

Chapin, C. E. and S. M. Cather, 1994. Tectonic setting of the axial basins of the northern and central Rio Grande rift, in Keller, G. R. and S. M. Cather eds., Basins of the Rio Grande rift: Structure, straigraphy, and tectonic setting, Boulder, Colorado, Geol. Soc. Am. Special Paper, G-3, 5-25.

Chase, C. G., J. A. Libarkin, and A. J. Sussman, 2002. Colorado Plateau: Geoid and means of isostatic support, International Geology Review, 44, 757-588.

Christensen, N. I., 1996. Poisson's ratio and crustal seismology, J. Geophys. Res., 101, 3,139-3,156.

Christiansen, R. L., and R. L. Yeats, 1992. Post-Laramide geology of the U. S. Cordilleran region, in Burchfiel, B. C., et al., eds., The Cordilleran orogen: Conterminous U.S.: Boulder, Corolado, Geological Society of America, Geology of North America, v. G-3, p. 261-406.

Coney, P. J. and S. J. Reynolds, 1977. Cordilleran Benioff zones, Nature, 270, 403-406.

Davis, P. M., P. Slack, H. A. Dahlheim, W. V. Green, R. P. Meyer, U. Achauer, A. Glahn, and M. Granet, 1993. Teleseismic tomography of continental rift zones, in Seismic Tomography: Theory and Practice, edited by H. M. Iyer and K. Hirahara, 397-439, Blackwell, London.

Dickinson, W. R. and W. S. Snyder, 1978. Plate tectonics of the Laramide orogeny, Mem. Geol. Soc. Am., 151, 355-366.

Dueker, K., H. Yuan, and B. Zurek, 2001. Thick-Structured Proterozoic lithosphere of the Rocky Mountain region, GSA Today, 11(12), 4-9.

Duess, A. and J. Woodhouse, 2001. Seismic observations of splitting of the mid-transition zone discontinuity in the Earth's mantle, Science, 294, 354-357.

Dunn, R. A., D. R. Toomey, and S. C. Solomon, 2000. Three-dimensional seismic structure and physical properties of the crust and shallow mantle beneath the East Pacific Rise at 9 degrees 30'N, J. Geophys. Res., B, 105 (10), 23,537-23,555.

Dziewonski, A. and D. Anderson, 1981. Preliminary reference Earth model, Phys. Earth Planet. Int., 25, 297-356.

Eaton, G. P., 1987. Topography and origin of the southern Rocky Mountains and Alvarado Ridge, in Continental Extensional Tectonics, Geological Soc Special Pub, 28, 355-369.

Ericksen, M. C. and R. Slingerland, 1990. Numerical simulations of tidal and wind-driven circulation in the Crteaceous Interior Seaway of North America, Geol. Soc. Am. Bull., 102, 1,499-1,516.

Estabrook, C. H. and R. Kind, 1996. The nature of the 660-kilometer upper-mantle seismic discontinuity from precursors to the PP phase, Nature, 274, 1179-1182.

Evans, J. R. and U. Achauer, 1993. Teleseismic velocity tomography using the ACH method: theory and application to continental-scale studies, in Seismic Tomography, Theory and Practice, edited by H. M. Iyer and K. Hirahara, pp. 319-360, Chapman and Hall, New York.

Flanagan, M. P. and Shearer, P. M., 1998, Global mapping of topography on transition zone discontinuities by stacking SS precursors, J. Geophys. Res., 103 (B2): 2,673-2,692.

Forsyth, D. W., S. C. Webb, L. M. Dorman, and Y. Shen, 1998. Phase velocities of Rayleigh waves in the MELT Experiment on the East Pacific Rise, Science, 280, 1235-1238.

Fuchs, K. and G. Muller, 1971. Computation of synthetic seismograms with the reflectivity method and comparison with observations, Geophys. J. R. Astron. Soc., 23, 417-433.

Fukao, Y., M. Obayashi, H. Inoue, and M. Nenbai, 1992. Subducting slabs stagnant in the transition zone, J. Geophys. Res., 97, 4,809-4,822.

Gao, S. S., K. H. Liu, P. M. Davis, P. D. Slack, Y. A. Zorin, V. V. Mordvinova, and V. M. Kozhevnikov, 2003. Evidence for small-scale mantle convection in the upper mantle beneath the Baikal rift, J. Geophys. Res., 108, doi:10.1029/2002JB002039.

Gao, W., S. P. Grand, W. S. Baldridge, D. Wilson, M. west, J. F. Ni, and R. Aster, 2004. Upper mantle convection beneath the central Rio Grande rift imaged by P and S wave tomography, J. Geophys. Res., 109, B03305, doi:10. 1029/2003JB002743.

Gilbert, H. J., A. F., Sheehan, K. G., Dueker, and P. Molnar, 2003. Receiver functions in the western United States, with implications for upper mantle structure and dynamics. J. Geophys. Res., 109(B5), doi:10.1029/2001JB00 1194.

Gok, R., J. Ni, E. Snadvol, D. Wilson, W. S. Baldridge, R. Aster, M. West, S. Grand, W. Gao, F. Tilmann, and S. Semken, 2003. Shear wave splitting and mantle flow beneath the LA RISTRA array, Geophys. Res. Lett, 30(12), 1614, doi:10.1029/2002GL016616.

Grand, S. P. and D. Helmberger, 1984. Upper mantle shear structure of North America, Geophys. J. R. astr. Soc. 76, 399-438.

Grand, S. P., 1994. Mantle shear structure beneath the Americas and surrounding oceans, J. Geophys. Res., 99, 11,591-11,621.

Grand, S. P., R. D. van der Hilst, and S. Widiyantoro, 1997. Global seismic tomography: A snapshot of convection in the Earth, Geo. Soc. Am. Today, 7(4), 1-7.

Gregory, K. M. and C. G. Chase, 1992. Tectonic significance of paleobotanically estimated climate and altitude of the late Eocene erosion surface, Colorado, Geology, 20, 581-585.

Gu, Y., Dziwonski, A. M. & Ekstrom, G. 2003. Simultaneous inversion for mantle and topography of transition zone discontinuities. Geophys. J. Int., 154, 559-583.

Helffrich, G. R. and B. J., Wood, 1996. 410-km discontinuity sharpness and the form of the olivine α–β phase diagram: Resolution of apparent seismic contradictions, Geophys. J. Int., 126, F7-F12.

Helffrich, G. R., E. Asencio, J. Knapp and T. Owens, 2003. Transition zone structure in a tectonically inactive area: 410 and 660 km discontinuity properties under the northern North Sea, Geophys. J. Int., 155, 193-199.

Heller, P. L., K. Dueker, and M. McMillan, 2003. Post-Paleozoic alluvial gravel transport as evidence of continental tilting in the U. S. Cordilleran, Geol. Soc. Am. Bull., 115, 1,122-1,132.

Humphreys, E. D., 1995. Post-Laramide removal of the Farallon slab, western United States, Geology, 23, 987-990.

Humphreys, E. D. and K. G. Duecker, 1994. Physical state of the western U.S. upper mantle, J. Geophys. Res., 99, 9,635-9,650.

Humphreys, E. D., E. Hessler, K. Dueker, G. L. Farmer, E. Erslov, and T. Atwater, 2003. How Laramide-age hydration of North American lithosphere by the Farallon slab controlled subsequent activity in the western U. S., Int. Geol. Rev., 45, 575-595.

James, D. E., M. J. Fouch, J. C. VanDecar, and S. Van der Lee, 2001. Tectospheric structure beneath southern Africa, Geophys. Res. Lett., 28, 2485-2488.

Karato, S., 1993. Importance of anelasticity in the interpretation of seismic tomography, Geophys. Res. Lett., 20, 1,623-1,626.

Karlstrom, K. E. and S. A. Bowring, 1988. Early Proterozoic assembly of tectonostratigraphic terranes in southwestern North America, J. Geology, 96, 561-576.

Karlstrom, K. E. and E. D. Humphreys, 1998. Persistent influence of Proterozoic accretionary boundaries in the tectonic evolution of southwestern North America: Interaction of cratonic grain and mantle modification events, Rocky Mountain Geology, 33, 161-179.

Keller, G. R., P. Morgan, and W. R. Seager, 1990. Crustal structure, gravity anomalies and heat flow in the southern Rio Grande rift and their relationship to extensional tectonics, Tectonophysics, 174, 21-37.

Kennett, B. L. N. and E. R. Engdahl, 1991. Traveltimes for global earthquake location and phase identification, Geophys. J. Int., 105, 429-465.

Kennett, B. L. N., E. R. Engdahl, and R. Buland, 1995. Constraints on seismic velocities in the Earth from travel times, Geophys. J. Int., 122, 108-124.

Lachenbruch, A. H. and J. H. Sass, 1977. Heat flow in the United States and the thermal regime of the crust in The Earth's Crust, Geophys. Monogr. Ser., vol 20, edited by J. G. Heacock, 626-675, AGU, Washington DC.

Lastowka, L. A., A. F. Sheehan, and J. M. Schneider, 2001. Seismic evidence for partial lithospheric delamination model of Colorado plateau uplift, Geophys. Res. Lett., 28, 1,319-1,322.

Lawton, T. F. and N. J. McMillan, 1999. Arc abandonment as a cause for passive continental rifting; Comparison of the Jurassic Mexican Borderland rift and the Cenozoic Rio Grande rift, Geology, 27, 779-782.

LeFevre, L. V. and D. V., Helmberger, 1989. Upper mantle P structure of the Canadian shield, J. Geophys. Res., 94, 17,749-17,765.

Lévêque, J. -J., and F. Masson, 1999. From ACH tomographic models to absolute velocity models, Geophys. J. Int., 137, 621-630.

Li, B., 2003. Compressional and shear wave velocities of ringwoodite γ-Mg_2SiO_4 to 12 GP, American Mineralogist, 88, 1,312-1,317.

Li, B., Y. R. C. Liebermann, and D. J. Weidner, 1998. Elastic Moduli of Wadsleyite (β-Mg_2Sio_4) to 7 Gigapascals and 873 Kelvin, Science, 281, 675-677.

Livaccari, R. F. and F. V. Perry, 1993. Isotopic evidence for preservation of Cordilleran lithospheric mantle during the Sevier-Laramide orogeny, western United States, Geology, 21, 719-722.

Matzel, E., 2002. The anisotropic seismic structure of the Earth's mantle: Investigations using full waveform inversion, Dissertation, The University of Texas at Austin.

Matzel, E. and S. P. Grand, 2004. The anisotropic seismic structure of the East European platform, J. Geophys. Res.,109, B01302, doi:10.1029/2001JB0.

McMillan, N. J., A. P. Dickin, and D. Haag, 2000. Evolution of magma source regions in the Rio Grande rift, southern New Mexico, Geol. Soc. Am. Bull., 112, 1,582-1,593.

McQuarrie, N., and C. Chase, 2000. Raising the Colorado Plateau, Geology, 28, 91-94.

Melbourne, T. and D. V. Helmberger, 1998. Fine structure of the 410 km discontinuity, J. Geophys. Res., 103, 10,091-10,102.

Menk, W., 1989. Geophysical data analysis: discrete inverse theory, Academic Press, Inc..

Michael T. Heath, 1997. Scientific Computing: An introductory Survey, WCB /McGraw-Hill.

Mitrovica, J. X., C. Beaumont, and G. T. Jarvis, 1989. Tilting of continental interiors by the dynamical effects of subduction, Tectonics, 8, 1,079-1,094.

Mora, P., 1988. Elastic wave-field inversion of reflection and transmission data, Geophysics, 53, 6, 750-759.

Morgan, P., W. R. Seager and M. P. Golombek, 1986. Cenozoic thermal, mechanical and tectonic evolution of the Rio Grande rift, J. Geophys. Res., 91, 6,263-6,276.

Morgan, P. and C. A. Swanberg, 1985. On the Cenozoic uplift and tectonic stability of the Colorado Plateau, J. Geodyn., 3, 39-63.

Mosher, S., 1998. Tectonic evolution of the southern Laurentian Grenville orogenic belt, Geol. Soc. Am. Bull., 110, 1,357-1,375.

Nataf, H. C. and Y. Ricard, 1996. 3SMAC: An a priori tomographic model of the upper mantle based on geophysical modeling, Phys. Earth Planet. Inter., 95, 101-122.

Niu, F. and H. Kawakatsu, 1998. Determination of the absolute depths of the mantle transition zone discontinuities beneath China: Effect of stagnant slabs on transition zone discontinuities, Earth, Planets and Space, 50, 965-975.

Nolet, G., 1975. Higher Rayleigh modes in western Europe, Geophys. Res. Lett., 2 (2), 60-62.

Nolet, G., 1990. Partitioned waveform inversion and two-dimensional structure under the Network of Autonomously Recording Seismographs, Journal of Geophysical Research, B, Solid Earth and Planets, 95 (6), 8499-8512.

Nolet, G., 1985. Solving or resolving inadequate and noisy tomographic systems, J. of Comp. Physics, 61, 463-482.

Nolet, G., 1987. Seismic wave propagation and seismic tomography, in Mathematical Geophysics, edited by Vlaar, Nolet Wortel, and Cloetingh, pp.155-187, D. Reidel Publishing Company.

Nolet, G., 1993. Solving large linearized tomographic problems, in Seismic Tomography, Theory and Practice, edited by H. M. Iyer and K. Hirahara, pp. 227-247, Chapman and Hall, New York.

Nolet, G., S. P. Grand, and B. L. N., Kennett, 1994. Seismic heterogeneity in the upper mantle, J. Geophys. Res., 99, pp. 23,753-23,766.

Nolet, G. and A. Zielhuis, 1994. Low S velocities under the Tornquist-Teisseyre zone: Evidence for water injection into the transition zone by subduction, J. Geophys. Res., 99, 15,813-15,820.

Olsen, K. H., G. R. Keller, and J. N. Stewart, 1979. Crustal structure along the Rio Grande rift from seismic refraction profiles, in Rio Grande Rift: Tectonics and Magmatism, edited by R. E. Riecker, Am. Geophys. Union, Washington DC.

Paige, C. C., and M. A. Saunders, 1982. LSQR: An algorithm for sparse linear equations and sparse least squares, ACM Transactions on Mathematical Software, 8, 43-71.

Paige, C. C., 1974. Bidiagonallization of matrices and solution of linear equations, SIAM J. Numer. Anal. 11, 197-209

Parker, E. C., P. M. Davis, J. R. Evans, H. M. Iyer, and K. H. Olsen, 1984. Upwarp of anomalous asthenosphere beneath the Rio Grande rift, Nature, 312, 354-356.

Pederson, J. L., R. D. Mackley, and J. L. Eddleman, 2002. Colorado Plateau uplift and erosion evaluated using GIS, GSA Today, 12(8), 4-10.

Perry, F. V., W. S. Baldridge, and D. J. DePaolo, 1988. Chemical and isotopic evidence for lithospheric thinning beneath the Rio Grande Rift, Nature, 332, 432-434.

Press, W., 1992. Numerical recipes in C: the art of scientific computing, 994 pp., Cambridge University Press, Cambridge.

Revenaugh, J., and S. A. Sipkin, 1994. Seismic evidence for silicate melt atop the 410-km mantle discontinuity, Nature, 369, 474-476.

Revenaugh, J. and S. A. Sipkin, 1994. Mantle discontinuity structure beneath China, J. Geophys. Res., 99, 21,911-21,927.

Ringwood, A. E., 1975. Composition and petrology of the Earth's mantle, McGraw-Hill, New York.

Ringwood, A. E. and T. Irifune, 1988. Nature of the 650-km seismic discontinuity: implications for mantle dynamics and differentiation, Nuture, 331, 131-1136.

Romanowicz, B., 1991. Seismic tomography of the Earth's mantle, Annu. Rev. Earth Planet. Sci., 19, 77-99.

Riter, J. C. A. and D. Smith, 1996. Xenolith constraints on the thermal history of the mantle below the Colorado Plateau, Geology, 24, 267-270.

Ryberg, T., F. Wenzel, A. V. Egorkin, and L. Solodilov, 1997. Short-period observation of the 520 km discontinuity in the northern Eurasia, J. Geophys. Res., 102, 5,413-5,422.

Sahagian, D., A. Proussevitch, and W. Carlson, 2002. Timing of Colorado Plateau uplift: Initial constraints from vesicular basalt-derived paleoelevations, Geology, 30, 807-810.

Saltzer, R. L. and E. D. Humphreys, 1997. Upper mantle P wave structure of the eastern Snake River Plain and its relationship to geodynamic models of the region, J. Geophys. Res., 102, 11,829-11,842.

Selverstone, J., A. Pun, and K. C. Condie, 1999. Xenolithic evidence for Proterozoic crustal evolution beneath the Colorado Plateau, GSA Bulletin, 111, 590-606.

Shearer, P. M., 1993. Global mapping of upper mantle reflectors from long-period SS precursors, Geophys. J. Int., 115, 878-904.

Shearer, P. M., 1990. Seismic imaging of upper-mantle structure with new evidence for 520-km discontinuity, Nature, 344, 121-126.

Shearer, P. M. and M. P. Flanagan, 1999. Seismic velocity and density jumps across the 410- and 660-kilometer discontinuities, Science, 285, 1545-1548.

Simmons, N. A. and H. Gurrola, 2000. Multiple seismic discontinuities near the base of the transition zone of the Earth's mantle, Nature, 405, 559-562.

Sinno, Y. A. and G. R. Keller, 1986. A Rayleigh wave dispersion study between El Paso, Texas and Albuquerque, New Mexico, J. Geophys. Res., 91, 6,168-6,174.

Sinogeikin, S. V., T. Katsura, and J. D. Bass, 1998. Sound velocities and elastic velocities of Fe-bearing wadsleyite and ringwoodite, J. Geophys. Res., 103, pp. 20,819-20,825.

Sinogeikin, S. V., J. D. Bass, and T. Katsura, 2003. Single-crystal elasticacity of ringwoodite to high pressure and high temperatures: implications for 520 km seismic discontinuity, Phys. Earth. Planet. Inter., 136, 41-66.

Slack, P. D., P. M. Davis, W. S. Baldridge, K. H. Olsen, A. Glahn, U. Achauer, and W. Spence, 1996. The upper mantle structure of the central Rio Grande rift region from teleseismic P and S wave travel time delays and attenuation, J. Geophys. Res., 101, 16,003-16,024.

Smith, D., 2000. Insights into the evolution of the uppermost continental mantle from xenolith localities on and near the Colorado Plateau and regional comparisons, J. Geophys. Res., 105, 16,769-16,781.

Smith, D., D. Moser, J. Connelly, K. Manser, and D. Schulze, 2002. U-Pb zircon ages of eclogites, garnetites, and Cenozoic rock-water reactions in Proterozoic mantle below the Colorado Plateau, Geol. Soc. Am. Abstracts, v. 34, 253.

Song, T., D. Helmberger, and S. P. Grand, 2004. Low-velocity zone atop the 410-km seismic discontinuity in the northwestern United States, Nature, 427, 530-533.

Spakman, W., and G. Nolet, 1988. Imaging algorithms, accuracy and resolution in delay time tomography, in Mathematical Geophysics, edited by Vlaar, Nolet, Wortel, and Cloetingh, pp.155-187, D. Reidel Publishing Company.

Spence, W., and R. S. Gross, 1990. A tomographic glimpse of the upper mantle source of magmas of the Jemez lineament, New Mexico, J. Geophys. Res., 95, 10,829-10,849.

Spencer, J. E., 1996. Uplift of the Colorado Plateau due to lithosphere attenuation during Laramide low-angle subduction, J. Geophys. Res., 101, 13,595-13,609.

Spetzler, J., J. Trampert, and R. Snieder, 2002. The effect of scattering in surface wave tomography, Geophys. J. Int., 149, 755-765.

Tanimoto, T., 2003. Geometrical approach to surface wave finite frequency effects, Geophys. Res. Lett., 30(19), doi:10.1029/2003GL017475.

Tajima, F. and P. Grand, 1995. Evidence of high anomalies in the transition zone associated with southern Kurile subduction zone, Geophys. Res. Lett., 22, 3,139-3,142.

Tajima, F. and P. Grand, 1998. Variation of transition zone high-velocity anomalies and depression of 660 km discontinuity associated with subduction zones from the southern Kuriles to Izu-Bonin and Ryukyu, J. Geophys. Res., 103, 15,015-15,036.

The MELT Seismic Team, 1998. Imaging the deep seismic structure beneath a mid-ocean ridge: the MELT experiment, Science, 280, 1215-1218.

Thompson, G. A., and M. L. Zoback, 1979. Regional geophysics of the Colorado Plateau, Tectonophysics, 61, 149-181.

Thurber, C., S. R. K. Roecker, M. P. L. Gold, and K. Rittger, 2003. Earthquake locations and three-dimensional fault zone structure along the creeping section of the San Andreas Fault near Parkfield, CA; preparing for

SAFOD, Geophysical Res. Lett., 30, no. 3 (3), 1112, doi:10.1029/2002GL 016004.

Tyburczy, J. A., T. S. Duffy, T. J. Ahrens, and M. A. Lange, 1991. Shock wave equation of state of serpentine to 150 GPA: Implications for the occurrence of water in the Earth's lower mantle, J. Geophys. Res., 96, 18,011-18,028.

Van der Sluis, A., and H. A. van der Vorst, 1988. Numerical solution of large, sparse linear algebraic systems arising from tomographic problems, in Seismic Tomography, edited by G. Nolet, pp49-83, D. Reidel Publishing Company.

Van der Lee, S. and G. Nolet, 1997. Seismic image of the subducted trailing fragments of the Farallon plate, Nature, 386, 266-269.

Van der Lee, S. and G. Nolet, 1997. Upper mantle S velocity structure of North America, J. Geophys. Res., 102 (10), 22,815-22,838.

Van der Lee, S., J. VanDecar, M. Fouch, and D. James, 2003. Upper mantle structure beneath southern Africa from multidisciplinary constraints, Geophys. Res. Abstr., 5, Abstract 05918.

Vinnik, L., M. R. Kumar, R. Kind, and V. Farra, 2003. Super-deep low-velocity layer beneath the Arabian plate, Geophys. Res. Lett., 30(7), 1415, doi:10. 1029/2002GL016590.

Walck, M. C., 1984. The P-wave upper mantle structure beneath an active spreading center – the Gulf of California. Geophys. J. R. astr. Soc. 76, 697-723.

Weidner, D. J., 1985. Mineral physics test of a pyrolite mantle, Geophys. Res. Lett., 12, 417-420.

West, M., J. Ni, W. S. Baldridge, D. Wilson, R. Aster, W. Gao, and S. Grand, 2004. Crust and upper mantle shear wave structure of the southwest United States J. Geophys. Res., 109, B03310, doi:1029/2003JB002575.

Williams, Q. and E. J. Garnero, 1996. Seismic evidence for partial melt at the base of Earth's mantle, Science, 273, 1,528-1,530.

Wilson, D., Aster, R., and the RISTRA Team, 2003. Imaging Crust and Upper Mantle Seismic Structure in the Southwestern United States Using Teleseismic Receiver Functions, The Leading Edge, 22(3), 232-237.

Wilson, D., R. Aster, J. Ni, S. Grand, M. West, W. Gao, W. S. Baldridge, and S. Semken, 2005. Imaging the seismic structure of the crust and upper mantle beneath the Great Plains, Rio Grande Rift, and Colorado Plateau using receiver functions, J. Geophys.Res., 110, B05306, ido:10.1029/2004JB003492.

Wood, B., 1995. The effect of H_2O on the 410-kilometer seismic discontinuity, Science, 268, 74-76.

Van der Sluis, A., and H. A. van der Vorst, Numerical solution of large, sparse linear algebraic systems arising from tomographic problems, in Seismic Tomography, edited by G. Nolet, pp49-83, D. Reidel Publishing Company, 1988

Van der Lee, S. and G. Nolet, 1997. Seismic image of the subducted trailing fragments of the Farallon plate, Nature, 386, 266-289.

Zhao, D., A. Hasegawa, and S. Horiuchi, 1992. Tomographic imaging of P and S wave velocity structure beneath northeastern Japan, J. Geophys. Res., 97, 19,909-19,928.

Zhao, D., Y. Xu, D. A. Wiens, L. Dorman, J. Hildebrand, and S. Webb, 1997. Depth extent of the Lau back-arc spreading center and its relation to subduction processes, Science, 278, 254-257.

VITA

Wei Gao was born in Jinzhou, Liaoning Province, China on February 18, 1960, son of Shenghe Gao and Xiuying Jiang.

In March, 1978, he attended the University of Science and Technology of China, majoring geophysics. He graduated with a Bachelor's degree from the department of Earth and Space Sciences in 1982. Afterward, he attended the Institute of Geophysics, China Seismological Bureau and graduated with a Master's degree in 1985. After Graduation, he worked as a research associate in Center for Prediction and Analysis, China Seismological Bureau until 1994. He then worked as a research scientist in the Center for Prediction and Analysis and the Institute of Geophysics, China Seismological Bureau until 1999 when he entered The University of Texas at Austin as a doctoral student.

Permanent address: China Seismological Bureau Apartments Apt. 252,
Jinjiachun, Fengtai District, Beijing 100036, China

This dissertation was typed by the author.